
[All ETDs from UAB](#)

[UAB Theses & Dissertations](#)

1992

Combined Backscatter Moessbauer spectrometer/x-ray fluorescence analyzer (BaMS/XRF) for planetary surface materials.

Tad Douglas Shelfer
University of Alabama at Birmingham

Follow this and additional works at: <https://digitalcommons.library.uab.edu/etd-collection>

Recommended Citation

Shelfer, Tad Douglas, "Combined Backscatter Moessbauer spectrometer/x-ray fluorescence analyzer (BaMS/XRF) for planetary surface materials." (1992). *All ETDs from UAB*. 5822.
<https://digitalcommons.library.uab.edu/etd-collection/5822>

This content has been accepted for inclusion by an authorized administrator of the UAB Digital Commons, and is provided as a free open access item. All inquiries regarding this item or the UAB Digital Commons should be directed to the [UAB Libraries Office of Scholarly Communication](#).

INFORMATION TO USERS

This manuscript has been reproduced from the microfilm master. UMI films the text directly from the original or copy submitted. Thus, some thesis and dissertation copies are in typewriter face, while others may be from any type of computer printer.

The quality of this reproduction is dependent upon the quality of the copy submitted. Broken or indistinct print, colored or poor quality illustrations and photographs, print bleedthrough, substandard margins, and improper alignment can adversely affect reproduction.

In the unlikely event that the author did not send UMI a complete manuscript and there are missing pages, these will be noted. Also, if unauthorized copyright material had to be removed, a note will indicate the deletion.

Oversize materials (e.g., maps, drawings, charts) are reproduced by sectioning the original, beginning at the upper left-hand corner and continuing from left to right in equal sections with small overlaps. Each original is also photographed in one exposure and is included in reduced form at the back of the book.

Photographs included in the original manuscript have been reproduced xerographically in this copy. Higher quality 6" x 9" black and white photographic prints are available for any photographs or illustrations appearing in this copy for an additional charge. Contact UMI directly to order.



University Microfilms International
A Bell & Howell Information Company
300 North Zeeb Road, Ann Arbor, MI 48106-1346 USA
313/761-4700 800/521-0600

Order Number 9312974

**Combined Backscatter Mössbauer spectrometer/x-ray
fluorescence analyzer (BaMS/XRF) for planetary surface
materials**

Shelfer, Tad Douglas, Ph.D.

University of Alabama at Birmingham, 1992

U·M·I
300 N. Zeeb Rd.
Ann Arbor, MI 48106

COMBINED BACKSCATTER MÖSSBAUER SPECTROMETER/X-RAY
FLUORESCENCE ANALYZER (BaMS/XRF) FOR PLANETARY SURFACE
MATERIALS

by

TAD DOUGLAS SHELFER

A DISSERTATION

Submitted in partial fulfillment of the requirements for
the degree of Doctor of Philosophy in the Department of
Physics in the Graduate School,
The University of Alabama at Birmingham

BIRMINGHAM, ALABAMA

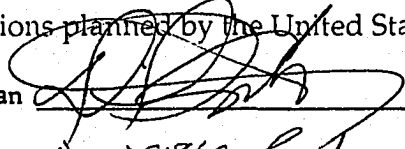
1992

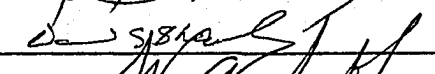
ABSTRACT OF DISSERTATION
GRADUATE SCHOOL, UNIVERSITY OF ALABAMA AT BIRMINGHAM

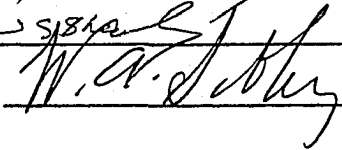
Degree Ph.D. Major Subject Physics
Name of Candidate Tad Douglas Shelfer
Title Combined Mossbauer Spectrometer/X-Ray Fluorescence Analyzer
(BaMS/XRF) For Planetary Surface Materials

The purpose of this work is to design, construct, and test a prototype (proof-of-concept) combination backscatter Mössbauer spectrometer and x-ray fluorescence analyzer (BaMS/XRF) instrument. Mössbauer spectroscopy is a sensitive technique for determining the oxidation state of iron in a sample, the mineralogy of each iron-bearing phase, and the relative distribution of iron among different phases. In addition to the mineralogical analysis provided by Mössbauer spectroscopy, elemental analysis can be performed concurrently using x-ray fluorescence. The BaMS geometry is optimized for XRF and no additional instrumentation is required to perform both experiments in this single instrument.

It is useful to divide the prototype instrument package into two components: 1) the probe head containing the Mössbauer drive with source and the detector system, and 2) the body unit comprised of the storage and control electronics and power supply. The completed BaMS/XRF probe unit is ~300 grams in mass, consumes less than 0.20 Watt of power, and is roughly the same size (volume) as a 12-ounce soft-drink can. A space-qualified version of the prototype instrument discussed in this work could play a pivotal role in the success of many upcoming exploration missions planned by the United States.

Abstract Approved by: Committee Chairman 

Program Director 

Date 1/6/93 Dean of Graduate School 

DEDICATION

I dedicate this work solely to the loving memory of a man who made it his life's work to insure that each member of his family had the maximum number of options from which to choose a life's work. I am grateful that I have been blessed with the opportunity to get a good education and pursue advanced degrees in what has always been my favorite hobby: physics. Thanks for everything Dad. I love you.

PS. I hope you have had time to scout heaven's lakes for us. Remember, you still owe me a fishing trip.

ACKNOWLEDGMENTS

I would like to gratefully acknowledge the time, assistance, and understanding given to me by Dr. David G. Agresti, my graduate advisor. Having a doctoral graduate student must be a lot like having a teenage child. A little knowledge made me believe I knew everything and I was always right. Thanks Dr. Agresti for the patience that only parents are supposed to understand. I would like to give special thanks to Dr. Edward L. Wills for access to his vast experience in experimental physics techniques (not to mention automotive repair). I must also thank Dr. Wills for the numerous fishing trips which helped keep me sane throughout this project. I am grateful to Dr. Richard V. Morris, my NASA technical advisor at NASA Johnson Space Center, for all the time and hard work he has put in to make this project a reality. I would like to thank the members of my graduate committee, Dr. Agresti, Dr. Wills, Dr. Thomas J. Wdowiak, Dr. William K. Nonidez (Chemistry Dept.), and Dr. Mark Drummond (Geology Dept.), for their assistance in polishing this scientific work.

I am grateful to all members of the UAB Physics Department's faculty and staff for their assistance in this project. I would like to give special thanks to Ming-Hung Shen (Electrical Engineer) and Jerry Sewell (Scientific Instrument Maker) for all they have done to make this project possible. I would also like to thank Donna Hamer and Donna Andrews for making science in the real world possible for the Physics Department.

I would like to thank and give all my love to my wife Leigh Ann and the rest of my family for all of the support and sacrifices they have made to allow me to pursue this advanced degree. To my loved ones I promise that any work

or discoveries I make in the future will not be used in any way to harm fellow human beings. Building weapon systems pays very well, but I know that my family and friends are my true wealth.

I am grateful to all of my fellow physics graduate students for their support, friendship, and interesting conversations. I am especially grateful for my friendships with Joseph Tombrello and Marsha Pimperl. I would like to remind all of my fellow graduate students to remember to network and stay in touch with each other.

Finally, I am very grateful for the financial support of this work by the NASA Graduate Researchers Program.

TABLE OF CONTENTS

	<u>Page</u>
ABSTRACT	ii
DEDICATION	iii
ACKNOWLEDGMENTS.....	iv
LIST OF TABLES.....	vii
LIST OF FIGURES.....	viii
 CHAPTER	
I INTRODUCTION	1
II BACKGROUND.....	8
A. Iron Mössbauer spectroscopy.....	8
B. X-ray fluorescence.....	22
III EXPERIMENTAL METHODS	
A. Mössbauer Spectroscopy	29
B. Historical development of the velocity transducer	32
C. Modern Mössbauer drive with control electronics	35
D. Radiation detector and signal conditioning circuitry	36
E. Multichannel analyzer (MCA)	37
F. Typical Mössbauer spectra	38
G. X-ray fluorescence (XRF)	40
IV RESULTS AND DISCUSSION	
A. Mössbauer drive system	41
B. Detector system	54
C. Complete BaMS/XRF system.....	61
V CONCLUSIONS.....	68
REFERENCES.....	70
 APPENDICES	
A MECHANICAL DRAWINGS.....	73
B ELECTRICAL SCHEMATICS.....	77
C COMPUTER PROGRAM.....	80
D EXPERIMENTAL DATA.....	91

LIST OF TABLES

<u>Table</u>	<u>Page</u>
I Percentage of Fe associated with each mineral for two lunar soils.....	5
II ^{57}Fe excited-state transition percentages and half-lives	10
III Isomer shift values for different ^{57}Fe source matrices.....	17
IV Transition intensities for various photon directions	22
V Maximum Compton energy shifts for some ^{57}Co emissions	29
VI Summary of microdrive characteristics for both spring designs	50

LIST OF FIGURES

<u>Figure</u>	<u>Page</u>
1 Transmission Mössbauer spectra of EETA79001 and H34	3
2 Transmission Mössbauer spectra of lunar soils 72131 and 73131	4
3 Transmission Mössbauer spectra of crushed lunar rock 70035	6
4 ^{57}Fe nuclear resonance effect	8
5 ^{57}Co nuclear decay diagram	9
6 Schematic illustration of the Mössbauer isomer shift interaction	16
7 Schematic illustration of the electric quadrupole interaction	20
8 Schematic illustration of the magnetic dipole interaction	21
9 Schematic diagram of the most common electronic transitions	24
10 Mass absorption coefficient of lead versus photon energy	26
11 K and L x-ray fluorescence yields as a function of atomic number	27
12 Schematic diagram of transmission Mössbauer spectrometer	29
13 Two types of geometries used in Mössbauer spectroscopy	31
14 Schematic diagram of two rotational Mössbauer drives	33
15 Schematic diagram of lead-screw Mössbauer drive	34
16 Kankleit Mössbauer drive construction	35
17 Schematic Mössbauer spectra of the isomer shift interaction	39
18 Schematic Mössbauer spectra of the electric quadrupole interaction	39
19 Schematic Mössbauer spectra of the magnetic dipole interaction	40
20 PZT transducer construction and connection to Mössbauer drive	42
21 Amplitude and phase response of standard laboratory drive	44
22 Miniature single-coil drive response	45
23 Microdrive amplitude and phase response	47

LIST OF FIGURES (Continued)

<u>Figure</u>	<u>Page</u>
24 Resonant frequency as a function of moving mass for the microdrive ..	48
25 Microdrive spring designs.....	49
26 Microdrive response using softer spring design	50
27 Resonant frequency as a function of moving mass using soft springs ...	51
28 Simplified schematic illustrating main functions of feedback circuit.....	52
29 Mössbauer spectrum obtained with feedback circuit and microdrive ...	55
30 Pulse height spectrum of ^{57}Co using HgI_2 detector	56
31 Backscatter Mössbauer spectrum using HgI_2 detector array	57
32 Schematic diagram of 2π backscatter proportional counter detector.....	58
33 Pulse height spectrum of ^{57}Co using 2π backscatter detector	58
34 PHA spectrum of ^{57}Co using PIN diode detector	59
35 Schematic diagram of component placement on aluminum chassis	62
36 Schematic diagram of a graded radiation shield.....	63
37 Overlay of individual difference K x-ray fluorescence spectra.....	64
38 Backscatter Mössbauer spectrum of enriched Fe foil	65
39 Backscatter Mössbauer spectrum of natural Fe foil.....	66
40 Backscatter Mössbauer spectrum of Hawaiian palagonite H34.....	67

CHAPTER I

INTRODUCTION

A priority for future spacecraft missions to the surfaces of the Moon, Mars, asteroids, and other solid solar system objects is instrumentation which can perform non-destructive *in-situ* mineralogical and elemental analyses. Such analyses would provide the fundamental data required to identify the surface materials present, and also provide clues to the formation and subsequent modification with time of the surface components. One element in particular, the element iron, stands out as an excellent probe of naturally occurring materials due to its high abundance and multivalent nature (primarily 0, +2, and +3 oxidation states). Information as to the oxidation state of iron and its distribution among iron bearing mineralogical phases greatly restricts the types of materials that may be present in a sample.

A combination backscatter Mössbauer spectrometer and x-ray fluorescence analyzer (BaMS/XRF) instrument is capable of measuring the distribution of iron among its oxidation states, the distribution of each oxidation state among different mineralogical phases, and the relative concentration of each element present in the sample. The BaMS/XRF instrument would be highly suitable for remote *in-situ* operation due to the overall simplicity of the instrument and the fact that no sample preparation would be required.

The utility of the diagnostic information iron Mössbauer spectroscopy (FeMS) can provide on the iron mineralogy of extraterrestrial surfaces has been demonstrated for both the planet Mars and the Moon.

Our knowledge of the Martian surface comes primarily from data returned by the two Viking landers and data collected from earth-based telescopic observations. Additionally, there is a group of meteorites known as SNCs which are believed to be material ejected from the surface of Mars through violent impact events [1]. EETA79001 is an example of a SNC meteorite which has not been strongly weathered as part of its brief stay in our terrestrial environment [1]. Therefore, it is believed that EETA79001 is generally representative of the unoxidized component of the Martian surface material.

In contrast to the fresh material formed by fundamental volcanic processes that EETA79001 represents, the fine sand and dust which coats a large portion of the Martian landscape and plays a major role in seasonal planet-wide dust storms represents the oxidized (weathered) Martian surface component. It is this fined-grained surface material which forms a majority of the bright regions of the Martian surface as seen from earth-based telescopes. Spectroscopic studies of these bright regions indicate the presence of crystalline iron oxide [2-4]. We have studied a number of laboratory Martian soil analogues and found that a good match to the observed reflectance spectra of Martian bright regions can be obtained through a mixture of bulk hematite ($\alpha\text{-Fe}_2\text{O}_3$) and very small particles of hematite including a superparamagnetic portion [5,6]. Superparamagnetic particles are crystalline particles with diameters generally below 10 nm [5]. Hawaiian palagonite H34 is a naturally occurring example of the mixture of bulk and fine iron oxide particles and has a reflectance spectrum similar to the Martian bright regions [2].

The Mössbauer spectra [7] of EETA79001 (unweathered Mars surface component) and H34 (weathered Mars surface component analogue) are shown in Fig. 1.

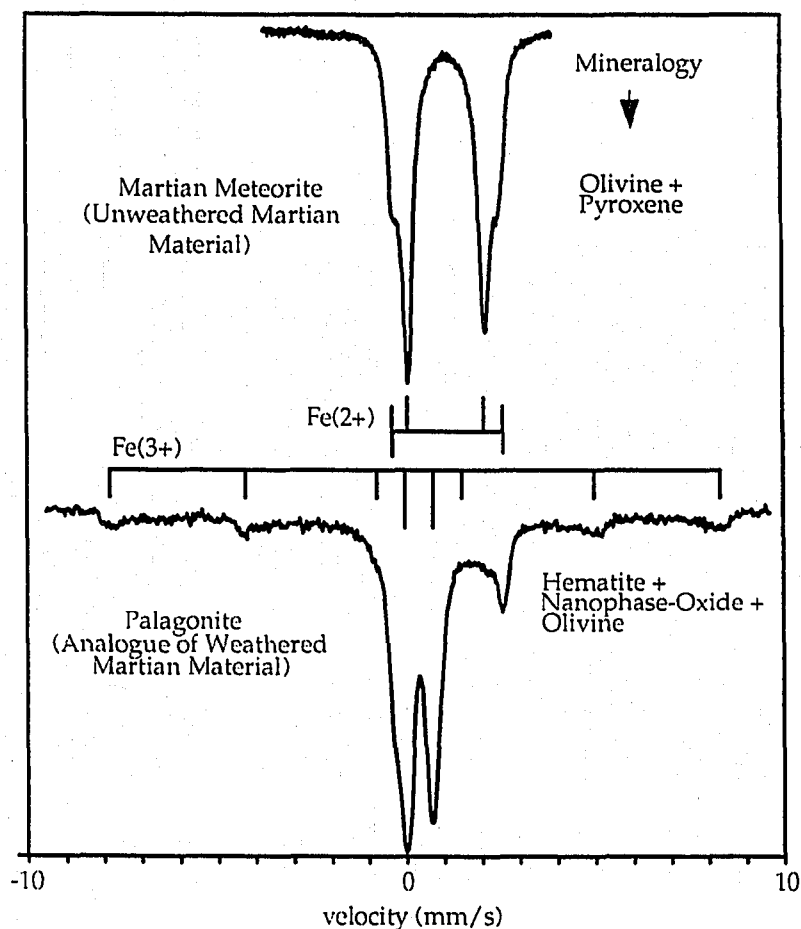


FIG. 1. Transmission Mössbauer spectra of EETA79001 and H34.

The Mössbauer spectrum of EETA79001 consists of two doublets characteristic of the presence of olivine $(\text{Mg,Fe})_2\text{SiO}_4$ and pyroxene $(\text{Mg,Fe,Ca})\text{SiO}_3$, both ferrous (+2) iron mineralogies. The relative area of each doublet is proportional to the amount of each phase present in the sample assuming their recoil-free fractions are nearly equal, as discussed later in the Mössbauer background tutorial given in Chapter II. Based on the relative areas in the spectrum, there is more pyroxene than olivine in EETA79001. In contrast, the Mössbauer spectrum of Hawaiian palagonite H34 is quite different and indicates the presence of ferric iron (+3) mineralogies in bulk hematite and superparamagnetic iron oxide, as well as olivine [7]. These spectra demonstrate the ability of Mössbauer spectroscopy to distinguish different iron mineralogies and determine the

relative amounts of each iron-bearing phase present. They show that FeMS carried out on the surface of Mars would be able to distinguish between weathered and unweathered surface materials. The technique is also capable of analyzing samples representing the wide range of mixtures between weathered and unweathered components expected on the surface.

FeMS has been applied extensively in analyzing the samples returned from the lunar surface during NASA's Apollo missions [8-10]. Figure 2 below shows the transmission Mössbauer spectra of two lunar soils 72131 and 73131 returned by Apollo 17 [11].

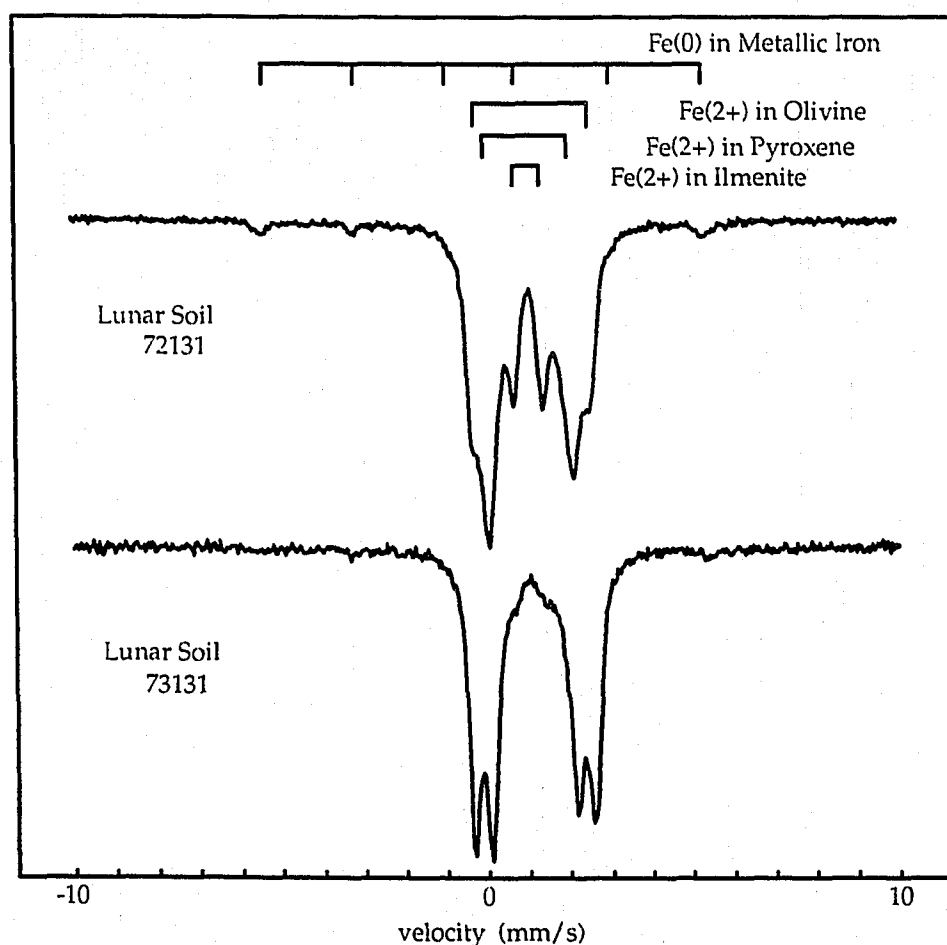


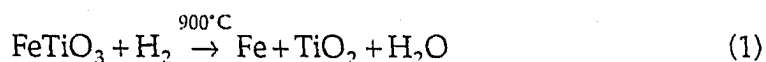
FIG. 2. Transmission Mössbauer spectra of lunar soils 72131 and 73131.

The spectrum of lunar soil 72131 is characteristic of three ferrous-bearing mineralogies including pyroxene, olivine, and ilmenite (FeTiO_3), in addition to a small amount of metallic iron. In contrast, the spectrum of lunar soil 73131 shows very different relative proportions of the three ferrous-bearing minerals. Based on the relative peak areas for pyroxene, olivine, and ilmenite, the total percentage of iron associated with each for both lunar samples is shown in Table I [11].

TABLE I. Percentage of Fe associated with each mineral for two lunar soils.

Lunar soil	% Pyroxene	% Olivine	% Ilmenite
72131	66	15	16
73131	57	39	4

The high sensitivity of FeMS in characterizing iron-bearing materials opens the possibility for using the Mössbauer technique for an important lunar resource application. A process by which water may be produced on the lunar surface through hydrogen reduction of the mineral ilmenite has been proposed [12]. This hydrogen reduction process is shown in the following chemical equation.



The water produced in this reduction process can be used for life support in a permanent lunar base or electrolyzed into oxygen and hydrogen gasses. The hydrogen gas could be recycled into the reduction system, while the oxygen could be used for life support and as fuel in various spacecraft.

A Mössbauer spectrometer could be used on the lunar surface as an instrument to prospect for ilmenite-rich mineral deposits. Additionally, it could be used by the hydrogen reduction reactor as a process control instrument in the evaluation of the efficiency of the reactor. Figure 3 shows the transmission

Mössbauer spectra of crushed lunar rock 70035 before and after the hydrogen reduction process [11]. The spectrum of 70035 before H_2 reduction is characteristic of pyroxene and ilmenite. After H_2 reduction, the spectrum shows that all of the iron in ilmenite has been converted into metallic iron, which signals the reduction process has been completed.

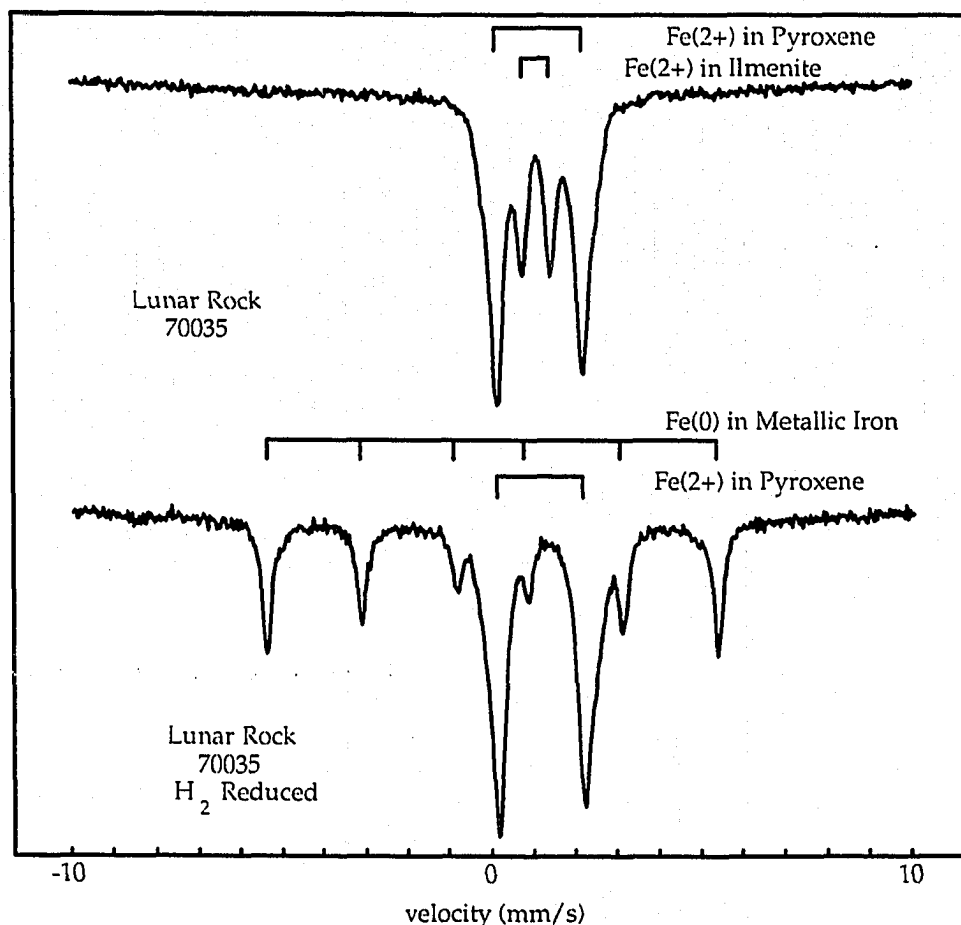


FIG. 3. Transmission Mössbauer spectra of crushed lunar rock 70035.

Mössbauer spectroscopy may also be used to determine the maturity of lunar soils [11,13,14]. This maturity factor would be important in identifying the relative amount of time that surface materials (~1mm deep) have been exposed to the solar wind. The maturity factor could therefore be useful in locating lunar materials rich in solar wind species such as N, H, ^3He for use as lunar resources.

Based on our studies of extraterrestrial surface materials using FeMS in the laboratory, we decided to initiate an instrument development program, as part of an ongoing collaborative effort between the U.A.B. Physics Department and NASA Johnson Space Center, to design and construct a working proof-of-concept iron Mössbauer spectrometer with suitable characteristics for use as a demonstration flight instrument. Thus, we proposed that a Mössbauer spectrometer be developed for "possible future NASA missions including lunar bases, the exploration of Mars and its moons, and the exploration of an asteroid" [15] at the November, 1988, Sample Acquisition, Analysis, and Preservation (SAAP) Instrument Technology Workshop, as part of the mineralogical working group. At the conclusion of this meeting, Mössbauer spectroscopy was rated as one of the enabling technologies for remote mineralogical analysis.

Based on private discussions with individuals involved in the development of missions to the Moon and Mars, we have established a set of characteristics that must be met or exceeded by a mineralogical instrument in order to be considered for inclusion on upcoming exploration missions. It is the design, construction, and testing of a prototype (proof-of-concept) instrument which meets the following characteristics that form the purpose and goal of this dissertation. The volume of the prototype instrument should be $<350 \text{ cm}^3$ (about the size of a soft-drink can), the instrument should be less than 500 g in mass, and it should consume no more than 2 W of electrical power.

CHAPTER II

BACKGROUND

The following theoretical material is intended to provide a brief tutorial background for the two experimental techniques included in the instrument described in this work. A more detailed description of the Mössbauer effect may be found in several texts on the subject [16,17]. Similarly, there are many fine texts available that provide a detailed description of the x-ray fluorescence spectroscopic technique [18,19].

A. Iron Mössbauer spectroscopy

Iron Mössbauer spectroscopy (FeMS) is a non-destructive nuclear spectroscopy technique which is concerned with the 14.4 keV transition between the ground state and the first excited state in the ^{57}Fe nucleus. The Mössbauer effect, also known as recoil-free nuclear resonance (RNR), is a resonance effect, which implies that radiation from a source is resonantly absorbed in a sample. This effect is shown schematically in Fig. 4, where an isolated ^{57}Fe nucleus in the first excited state decays to the ground state emitting a 14.4 keV γ -ray which is then resonantly absorbed by another isolated ^{57}Fe nucleus.

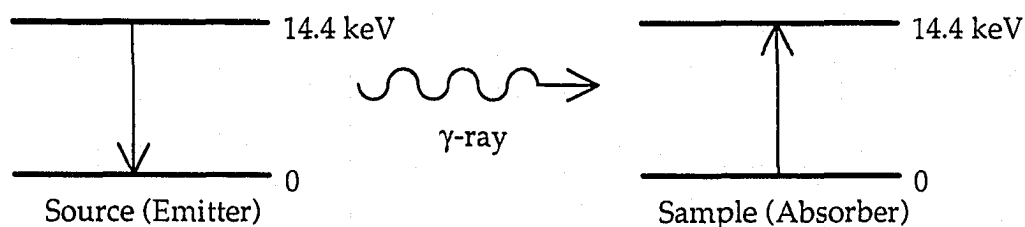


FIG. 4. ^{57}Fe nuclear resonance effect.

The problem with this simple schematic illustration is that the energy of the emitted γ -ray is reduced due to the recoil of the emitting nucleus. The recoil energy loss, E_R , can be calculated starting with the conservation of linear momentum shown below.

$$\vec{p}_{\text{nucleus}} = \vec{p}_{\gamma\text{-ray}} \quad (2)$$

The magnitude of the γ -ray momentum is given by:

$$p_{\gamma\text{-ray}} = E_{\gamma\text{-ray}} / c \quad (3)$$

where $E_{\gamma\text{-ray}}$ is the energy of the γ -ray photon and c is the speed of light. E_R can now be written using the non-relativistic approximation as follows:

$$E_R \approx p_{\text{nucleus}}^2 / 2M \Rightarrow E_R = E_{\gamma\text{-ray}}^2 / 2Mc^2 \quad (4)$$

where M is the nuclear mass. From this equation, E_R for the 14.4 keV photon emission of ^{57}Fe is approximately 1.96×10^{-3} eV.

The usual parent nucleus that provides ^{57}Fe nuclei in the first excited-state is ^{57}Co . The nuclear decay diagram for ^{57}Co is shown in Fig. 5 [20].

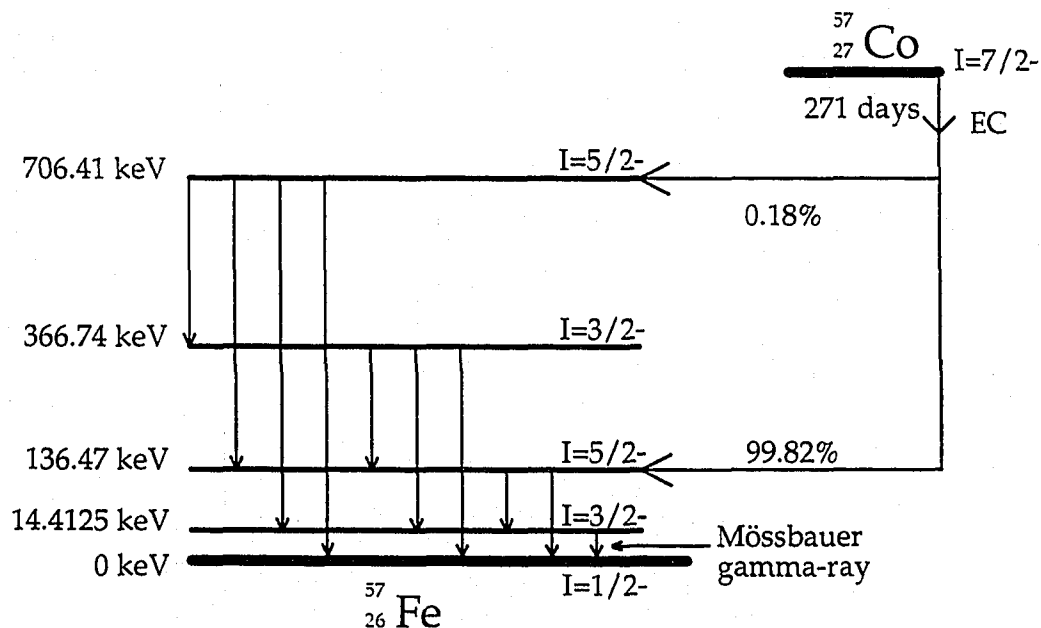


FIG. 5. ^{57}Co nuclear decay diagram.

The levels are shown in the figure with energies and spin-parity assignments. The relative transition probabilities and excited-state half-lives for the levels of Fig. 5 are listed in Table II [20].

TABLE II. ^{57}Fe excited-state transition percentages and half-lives.

Energy (keV)	14.4125	136.471	366.74	706.41
366.74	----	----	----	2.5
136.471	----	----	8	8
14.4125	----	89	77	86
0	100	11	15	3.5
Half-life (ns)	97.7	8.5	0.0069	0.003

The energies listed across the top of Table II represent the upper level of a transition, while the energy levels listed on the left side represent the lower level.

The natural line width of the 14.4 keV γ -ray, $\Gamma_{\gamma\text{-ray}}$, can be calculated from the half-life of the first excited level, 97.7 ns, using the Heisenberg uncertainty principle:

$$\Delta E \cdot \Delta t \geq \hbar / 2 \quad (5)$$

where ΔE represents the uncertainty in energy, Δt is the uncertainty in time, and \hbar is Planck's constant divided by 2π (6.5855×10^{-16} eV·s). Equation (5) can be rewritten in terms of the natural line width (full width at half maximum of a Lorentzian energy distribution [17]) and the mean lifetime, τ , of the excited state as:

$$\Gamma_{\gamma\text{-ray}} \cdot \tau = \hbar \quad (6)$$

where τ is the excited state half-life divided by $\ln 2$. From this calculation, the value of $\Gamma_{\gamma\text{-ray}}$ is 9.7×10^{-9} eV. With a recoil energy five orders of magnitude greater than the line width, it is clear that the resonance condition will not be satisfied. The problem is analogous to firing a cannon from a sled on a sheet of

ice. When fired, the cannon slides in the opposite direction to the projectile and reduces the projectile's energy. The solution is to somehow fix the cannon's position, such as bolting it to a giant concrete block frozen in the ice, assuring that essentially all of the energy is transferred to the projectile.

In 1961, Rudolph L. Mössbauer won the Nobel prize in physics for the discovery of recoil-free emission and absorption of gamma rays in nuclei. This was achieved much like the example of the cannon; however, rather than bolting the emitting nucleus to a giant concrete block, the nucleus is located in a crystalline lattice (or other solid host material). Quantum mechanics predicts that if the recoil energy is smaller than the mean energy required to excite vibrations (phonons) in the host lattice, then an appreciable fraction of γ -rays will be emitted without loss of energy to the host environment, i.e., recoil-free. High quality ^{57}Co Mössbauer sources typically have recoil-free fractions of around 95%.

The true power of Mössbauer spectroscopy is based on the fact that the energy levels of the nucleus are affected by the electronic and magnetic environments surrounding the nucleus. The simple nuclear level diagram shown in Fig. 4 is altered by two fundamental hyperfine interactions (interactions between the nucleus and the atomic electrons): 1) the nuclear quadrupole interaction, including the so-called "chemical isomer shift" (electronic) and 2) the nuclear Zeeman splitting (magnetic).

1. Nuclear quadrupole interaction

The nuclear quadrupole interaction is due to the Coulomb interaction between the nuclear charge distribution and the associated electron charge distribution, which is distorted due to other electrons and ions located in the nearby environment. The finite probability of finding electrons, in particular s-electrons, inside the nucleus implies that any distortions experienced by the

electrons will also be felt by the nucleus. If the nuclear charge density is represented by $\rho(\vec{r})$ and the electric potential due to the electrons and ions which surround the nucleus is represented by $\phi(\vec{r})$, then the total energy can be written as follows:

$$U = \int \rho(\vec{r})\phi(\vec{r})d\vec{v} \quad (7)$$

assuming the integral is extended over the nuclear volume. The fact that the nucleus is much smaller in size than the whole atom implies that the potential $\phi(\vec{r})$ changes very little over the dimensions of the nucleus and may be assumed to be nearly constant. With this assumption, the potential can be expanded using the multipole expansion:

$$\phi(\vec{r}) = \phi(0) + \sum_{i=1}^3 x_i \frac{\partial \phi}{\partial x_i} \Big|_0 + \frac{1}{2} \sum_{i,j} x_i x_j \frac{\partial^2 \phi}{\partial x_i \partial x_j} \Big|_0 + \dots \quad (8)$$

where the origin is located at the center of the nucleus and the derivatives are evaluated at the origin, and $\vec{r} = (x_1, x_2, x_3)$. The total energy can now be written as a series of terms as shown.

$$U = \sum_{n=0}^{\infty} U_n \quad (9)$$

The first term in this series U_0 represents the monopole term as follows:

$$U_0 = \int \rho(\vec{r})\phi(0)d\vec{v} = \left[\int \rho(\vec{r})d\vec{v} \right] \phi(0) = Ze\phi(0) \quad (10)$$

where Z is the nuclear charge and e is the magnitude of the electronic charge. U_0 is a constant term which is the same for all nuclear levels and therefore, when measuring energy differences (transitions) between two levels, the constant term cancels out. The monopole term may be disregarded.

The next term in the series is the dipole term U_1 .

$$U_1 = \sum_{i=1}^3 \left[\int x_i \rho(\vec{r})d\vec{v} \right] \frac{\partial \phi}{\partial x_i} \Big|_0 = 0 \quad (11)$$

This term is zero because the nuclear charge density is symmetric about the origin, that is $\rho(\vec{r}) = \rho(-\vec{r})$, which makes the product of $x_i \cdot \rho(\vec{r})$ an odd function of x_i . The integral of an odd function over the symmetric limits of the nuclear volume is zero.

The quadrupole term U_2 is shown below.

$$U_2 = \frac{1}{2} \sum_{i,j=1}^3 \left[\int x_i x_j \rho(\vec{r}) d\vec{v} \right] \frac{\partial^2 \phi}{\partial x_i \partial x_j} \Big|_0 \neq 0 \quad (12)$$

The quadrupole term does not equal zero and we shall return to U_2 shortly.

The octupole term U_3 is equal to zero for the same reasons as the dipole term. The hexadecapole term U_4 is not equal to zero but it involves a fourth-order derivative of a slowly varying function and can be ignored along with all higher terms in the multipole expansion.

The only term in the multipole expansion of importance here is the quadrupole term U_2 repeated below:

$$U_2 = \frac{1}{2} \sum_{i,j=1}^3 \left[\int x_i x_j \rho(\vec{r}) d\vec{v} \right] \phi_{ij} \quad (13)$$

where the tensor ϕ_{ij} has been introduced to simplify the notation.

$$[\phi_{ij}] = \left[\frac{\partial^2 \phi}{\partial x_i \partial x_j} \right]_0 = \begin{bmatrix} \frac{\partial^2 \phi}{\partial x_1^2} & \frac{\partial^2 \phi}{\partial x_1 \partial x_2} & \frac{\partial^2 \phi}{\partial x_1 \partial x_3} \\ \frac{\partial^2 \phi}{\partial x_2 \partial x_1} & \frac{\partial^2 \phi}{\partial x_2^2} & \frac{\partial^2 \phi}{\partial x_2 \partial x_3} \\ \frac{\partial^2 \phi}{\partial x_3 \partial x_1} & \frac{\partial^2 \phi}{\partial x_3 \partial x_2} & \frac{\partial^2 \phi}{\partial x_3^2} \end{bmatrix}_0 \quad (14)$$

The trace of the ϕ_{ij} tensor is shown below.

$$T = \frac{\partial^2 \phi}{\partial x_1^2} \Big|_0 + \frac{\partial^2 \phi}{\partial x_2^2} \Big|_0 + \frac{\partial^2 \phi}{\partial x_3^2} \Big|_0 = \nabla^2 \phi \Big|_0 \quad (15)$$

From Poisson's equation the value of the trace is known to be:

$$T = \nabla^2 \phi|_0 = -4\pi\rho_{\text{elec}}(0) = 4\pi e|\psi_{\text{elec}}(0)|^2 \quad (16)$$

where $\rho_{\text{elec}}(0)$ is the electron charge density within the nuclear volume, $|\psi_{\text{elec}}(0)|^2$ is the total electronic probability density at the nucleus, and $-e$ is the charge of an electron.

It is now useful to define a new tensor V_{ij} which has a trace of zero as shown:

$$V_{ij} = \phi_{ij} - \frac{1}{3}T\delta_{ij} \quad (17)$$

where $\delta_{ij} = 0$ if $i \neq j$, and $\delta_{ij} = 1$ if $i = j$. The quadrupole term of the total energy can now be broken into two pieces.

$$U_2 = \frac{1}{2} \sum_{i,j=1}^3 \left[\int x_i x_j \rho(\vec{r}) d\vec{v} \right] V_{ij} + \frac{1}{2} \sum_{i,j=1}^3 \left[\int x_i x_j \rho(\vec{r}) d\vec{v} \right] \left(\frac{1}{3}T \right) \delta_{ij} \quad (18)$$

The first term in this sum is labeled U_Q and is typically referred to as the electric quadrupole interaction. U_Q is directional in nature and leads to the splitting of nuclear levels with spins $I \geq 1$. U_Q will be discussed shortly.

The second term in the sum, which will be labeled U_δ , is the isomer shift interaction. Using the properties of δ_{ij} , the summation in U_δ may be written as shown:

$$\sum_{i=1}^3 \int x_i^2 \rho(\vec{r}) d\vec{v} = \int r^2 \rho(\vec{r}) d\vec{v} = Ze \langle r^2 \rangle_{\text{nucleus}} \quad (19)$$

where $\langle r^2 \rangle_{\text{nucleus}}$ is the average value of the square of the nuclear radius. The isomer shift interaction U_δ can now be written using Eq. (16) as:

$$U_\delta = \frac{2}{3} \pi Z e^2 \langle r^2 \rangle_{\text{nucleus}} |\psi_{\text{elec}}(0)|^2. \quad (20)$$

For simplicity, the nuclear charge density may be assumed to be distributed uniformly within a sphere of radius R , and U_δ can be simplified by the following relationship:

$$\langle r^2 \rangle_{\text{nucleus}} = \frac{1}{Ze} \int r^2 \rho(\vec{r}) d\mathbf{v} = \frac{1}{V} \int_0^R r^2 \cdot 4\pi r^2 dr = \frac{3}{5} R^2 \quad (21)$$

where $V = 4\pi R^3/3$ is the nuclear volume. Finally, the isomer shift interaction U_δ can be rewritten:

$$U_\delta = \frac{2}{5} \pi Z e^2 R^2 |\psi_{\text{elec}}(0)|^2. \quad (22)$$

It should be pointed out that some authors incorrectly associate the isomer shift interaction with the monopole expansion term rather than as a part of the quadrupole term (see for example Ref. 21).

The isomer shift interaction results in a simple shift of the nuclear energy levels. In general, the shift is different for the ground and excited states due to the fact that the radius of the nucleus is different for the various energy levels. The shift is also typically different for the source and sample due to differing chemical environments. The isomer shift interaction is shown schematically in Fig. 6. In the figure, the Mössbauer γ -ray is emitted from the source with energy E_s related to the isomer shift interaction for each level as follows:

$$E_s = E_0 + (U_{\delta_{\text{source}}}^* - U_{\delta_{\text{source}}}) \quad (23)$$

where E_0 is the γ -ray energy of the bare nucleus, $U_{\delta_{\text{source}}}^*$ is the isomer shift of the excited level, and $U_{\delta_{\text{source}}}$ is the isomer shift of the ground state. The resonant energy of the sample can be written as shown.

$$E_a = E_0 + (U_{\delta_{\text{sample}}}^* - U_{\delta_{\text{sample}}}) \quad (24)$$

The resonant energy difference between the source and absorber is now shown:

$$\delta = E_a - E_s. \quad (25)$$

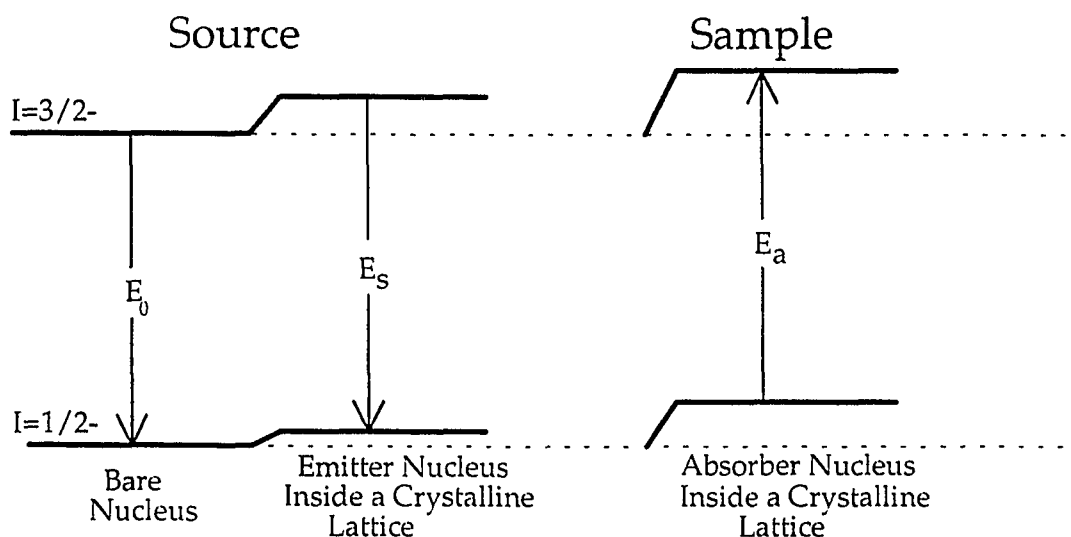


FIG. 6. Schematic illustration of the Mössbauer isomer shift interaction.

This energy difference, δ , known as the isomer shift or the chemical shift, is the value typically reported in the literature. Note that δ is measured with respect to the isomeric interactions in the source. This implies that different values for the isomer shift will be measured for the same sample if a different source matrix is used. By convention, isomer shift data are published with respect to metallic α -iron using published tables of isomer shift data for different source matrix materials and making the appropriate correction. Table III lists some common isomer shift values for different sources matrices and an α -Fe absorber [22]; in the table, K+ represents $K_4Fe(CN)_6 \cdot 3H_2O$ (potassium hexacyanoferrate), SS represents stainless steel (300 series), and Na+ represents $Na_2[Fe(CN)_5NO] \cdot 2H_2O$ (sodium nitroprusside).

We now return to the electric quadrupole interaction term, U_Q , from Eq. (18):

$$U_Q = \frac{1}{6} \sum_{i,j=1}^3 \left[\int (3x_i x_j - r^2 \delta_{ij}) \rho(\vec{r}) d\vec{r} \right] V_{ij} \quad (26)$$

TABLE III. Isomer shift values for different ^{57}Fe source matrices.

Source	IS (mm/s)	Source	IS (mm/s)	Source	IS (mm/s)	Source	IS (mm/s)
Au	-0.632	Cu	-0.226	Mo	-0.060	SS	0.090
In	-0.530	Ir	-0.225	Ta	-0.033	Ti	0.108
Zn	-0.527	Pd	-0.185	Fe	0	Cr	0.152
Ag	-0.525	Be	-0.120	Nb	0.015	V	0.198
Pt	-0.347	Rh	-0.114	K+	0.045	Na+	0.257

where U_Q has been written in conventional notation, using the fact that $\sum V_{ii} = 0$. In order to simplify the mathematics without danger of affecting any physical results, a new set of axes is chosen, the principle axis system, which we will use from this point on, in which V_{ij} is diagonal as shown. (For convenience, we continue to use the notation V_{ij} , now equal to V_{ij} referred to principle axes.)

$$[V_{ij}] = \begin{bmatrix} V_{xx} & 0 & 0 \\ 0 & V_{yy} & 0 \\ 0 & 0 & V_{zz} \end{bmatrix} \quad (27)$$

By convention, the axes are chosen such that $|V_{zz}| \geq |V_{yy}| \geq |V_{xx}|$. The trace is invariant under rotation and we still have $V_{xx} + V_{yy} + V_{zz} = 0$, which implies the tensor is determined by just two independent parameters. These are defined by:

$$eq = V_{zz} \text{ and } \eta = \frac{V_{xx} - V_{yy}}{V_{zz}} \quad (28)$$

where eq is the negative axial component of the electric field gradient and η is the asymmetry parameter. The electric quadrupole interaction (26) can now be written:

$$U_Q = \frac{1}{6} \sum_{i=1}^3 \left[\int (3x_i^2 - r^2) \rho(\vec{r}) d\vec{v} \right] V_{ii} \quad (29)$$

which can be rewritten in terms of the two independent variables eq and η .

$$U_Q = \frac{eq}{4} \left[\int (3z^2 - r^2) \rho(\bar{r}) d\mathbf{v} + \eta \int (x^2 - y^2) \rho(\bar{r}) d\mathbf{v} \right] \quad (30)$$

The Wigner-Eckart theorem can now be used to simplify U_Q and make further computations much clearer. This theorem states that since \bar{r} transforms like the angular momentum vector \bar{I} under certain rotations, the matrix elements of U_Q formed between two states are proportional to matrix elements formed by replacing the coordinates x , y , and z with the angular momentum operators \hat{I}_x , \hat{I}_y , and \hat{I}_z , respectively. The theorem is illustrated below:

$$\int f(x, y, z) \rho(\bar{r}) d\mathbf{v} = \text{const} \cdot \langle f(\hat{I}_x, \hat{I}_y, \hat{I}_z) \rangle \quad (31)$$

where $\rho(\bar{r})$ is evaluated in the particular quantum mechanical state, $|R(r)\rangle |I, m_I\rangle$, and the proportionality constant is independent of m_I .

To find the constant, we begin by defining the nuclear electric quadrupole moment Q [23]:

$$eQ = \int (3z^2 - r^2) \rho(\bar{r}) d\mathbf{v} \quad (32)$$

where $\rho(\bar{r})$ is evaluated in the state with $m_I = I$. Thus,

$$eQ = C \langle I, I | 3\hat{I}_z^2 - \bar{I}^2 | I, I \rangle = C [3I^2 - I(I+1)] = C(2I^2 - I) \quad (33)$$

where C is a proportionality constant which may be written as follows.

$$C = \frac{eQ}{[I(2I-1)]}. \quad (34)$$

Then, we note that the second term in U_Q , Eq. (30), leads to zero:

$$\int (x^2 - y^2) \rho d\mathbf{v} \propto \langle \hat{I}_x^2 - \hat{I}_y^2 \rangle = 0 \quad (35)$$

since the state $|I, I\rangle$ is rotationally symmetric. The full Hamiltonian operator for the electric quadrupole interaction can now be written.

$$\hat{H}_Q = \frac{eq}{4} \cdot \frac{eQ}{I(2I-1)} [3\hat{I}_z^2 - I(I+1) + \eta(\hat{I}_x^2 - \hat{I}_y^2)] \quad (36)$$

\hat{H}_Q is much easier to evaluate when the raising and lowering operators are used instead of \hat{I}_x and \hat{I}_y . The relationship between these operators is shown below [24].

$$\hat{I}_x^2 - \hat{I}_y^2 = \frac{1}{2}(\hat{I}_+^2 + \hat{I}_-^2) \quad (37)$$

Finally, \hat{H}_Q can now be written in the following form.

$$\hat{H}_Q = \frac{e^2 q Q}{4I(2I-1)} \left[3\hat{I}_z^2 - I(I+1) + \eta(\hat{I}_+^2 + \hat{I}_-^2) \right] \quad (38)$$

As stated earlier, the electric quadrupole interaction removes some of the degeneracy of nuclear levels with $I \geq 1$. In the case of ^{57}Fe , the presence of an electric field gradient at the nucleus results in the splitting of the excited state $I=3/2$ into two levels and leaves the ground state unchanged since $I=1/2$. The energy difference between split levels is now given by the solution of Schrödinger's equation with the electric quadrupole interaction Hamiltonian \hat{H}_Q shown in Eq. (38):

$$E_Q = \langle \hat{H}_Q \rangle = \pm \frac{e^2 q Q}{4} \sqrt{1 + \frac{\eta^2}{3}} \quad (39)$$

where $e^2 q Q$ is defined as the electric quadrupole coupling constant, and $e^2 q Q/2$ is the "quadrupole splitting" term used in the literature. The quadrupole splitting is the separation between the two $I=3/2$ sublevels in Fig. 7 (shown for $\eta=0$). Note that with quadrupole splitting there are now two possible transitions between the ground state and first excited state. This implies that there are now two energies E_1 and E_2 at which resonant absorption can occur.

2. Nuclear Zeeman splitting

Any nucleus with a magnetic moment $\vec{\mu}$ in the presence of a magnetic field \vec{B} will experience shifts in nuclear energy levels as expressed by the following Hamiltonian operator:

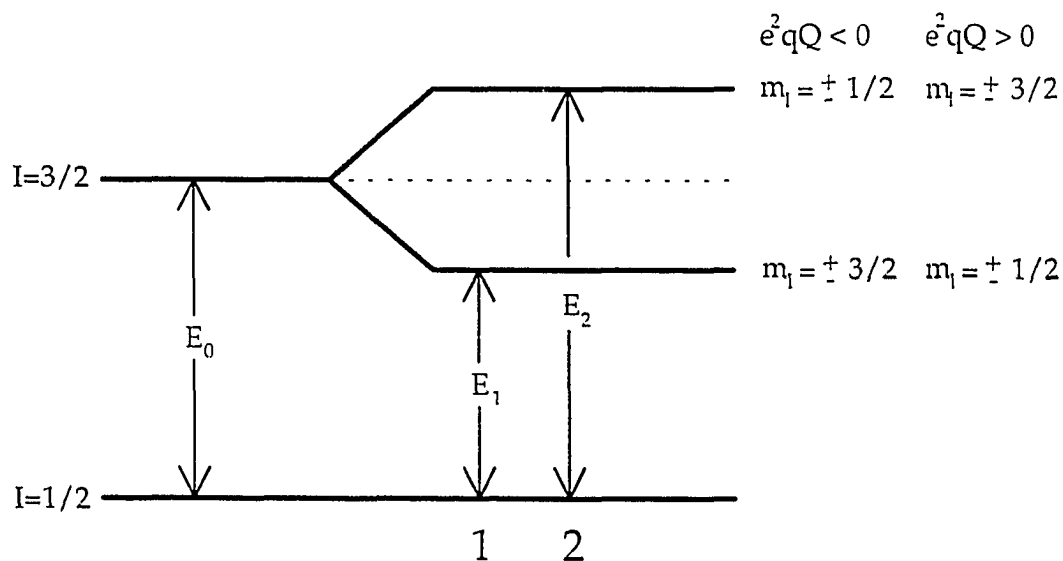


FIG. 7. Schematic illustration of the electric quadrupole interaction.

$$\hat{H}_M = -\vec{\mu} \cdot \vec{B} = -g\mu_N B \hat{I}_z \quad (40)$$

where g is nuclear g -factor or gyromagnetic ratio, and μ_N is the nuclear magneton (3.1525×10^{-12} eV/gauss). The magnetic field at the nucleus may be due to the magnetization of the material in which the nucleus resides or due to a magnetic field produced externally in the lab, or a combination of the two. The effect of this magnetic dipole interaction is to totally remove the degeneracy of all nuclear levels with $I > 0$. The energy splittings of the levels can be found by solving Schrödinger's equation using the magnetic dipole interaction Hamiltonian in Eq. (40) as follows:

$$E_M = \langle I, m_I | \hat{H}_M | I, m_I \rangle = -g\mu_N B m_I \quad (41)$$

where m_I is the magnetic quantum number.

The splitting of the nuclear levels of ^{57}Fe due to the magnetic dipole interaction is shown in Fig. 8. Zeeman splitting has removed the degeneracy for both nuclear energy levels.

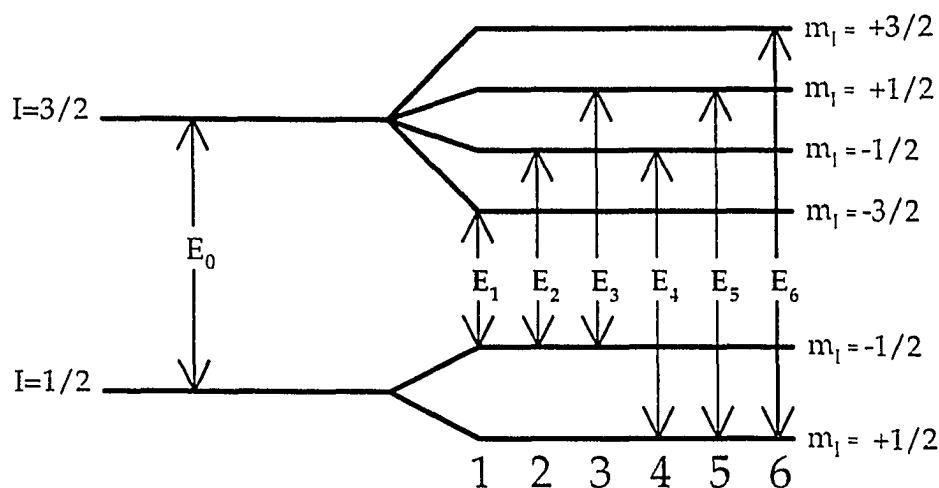


FIG. 8. Schematic illustration of the magnetic dipole interaction.

Since the 14.4 keV transition results from the magnetic dipole interaction (M1 transition), m_l may change only by 0 or ± 1 . This fact accounts for the lack of transitions drawn between the ground $m_l = +1/2$ to the excited $m_l = -3/2$ states and the ground $m_l = -1/2$ to the excited $m_l = +3/2$ states. There are now six possible transitions, which implies six different possible resonant absorption energies. The inversion of levels seen in the excited state is due to the negative g -factor of the excited state ($g_{\text{ground}} = 0.0907$, $g_{\text{excited}} = -0.0518$) [22]. From an analysis of an observed sextet, the effective magnetic field experienced by the nucleus may be measured.

The transition probabilities or intensities for each of the six possible resonance energies are proportional to the squares of the Clebsch-Gordan coefficients that couple any two quantum states, and also depend on the angle Θ between the γ -ray direction and the direction of \vec{B} . Table IV lists the relative intensities of the six transitions for three useful cases: randomly oriented powder, $\Theta=0$ degrees, and $\Theta=90^\circ$.

In general, a ^{57}Fe nucleus will be affected by one or more of the interactions discussed: the isomer shift, electric quadrupole splitting, and Zeeman splitting. These interactions lead to shifts in the resonance energy

TABLE IV. Transition intensities for various photon directions.

Transition	m_i ground	m_i excited	Θ random	$\Theta=0$	$\Theta=90^\circ$
1	-1/2	-3/2	3	3	3
2	-1/2	-1/2	2	0	4
3	-1/2	+1/2	1	1	1
4	+1/2	-1/2	1	1	1
5	+1/2	+1/2	2	0	4
6	+1/2	+3/2	3	3	3

condition and remove degeneracies, allowing multiple resonant absorptions. The number and positions of resonant energy levels can be quite complex for minerals which contain iron in many different crystallographic environments where the total number and position of resonant absorptions is the superposition of all the individual components. It is the detail of information Mössbauer spectroscopy provides on the electronic and magnetic environment of individual Fe nuclei which makes this technique so powerful for iron containing materials. Different solid environments lead to unique peak positions in the Mössbauer spectrum based on the three interactions, and these peak positions form characteristic spectral "fingerprints" for different mineralogical environments. If several different environments exist in a sample, then the relative area associated with each spectral fingerprint is proportional to the amount of iron located in each environment in the sample (assuming equal recoil-free fractions for each site).

B. X-ray fluorescence

Energy dispersive x-ray fluorescence spectroscopy is a powerful non-destructive technique which uses the characteristic x-rays of individual atoms to accurately determine the elemental composition of a sample. These

characteristic x-rays can be described using the Bohr model of the atom, in which there is a central positively charged nucleus surrounded by a series of negatively charged spherical shells of electrons. Based on the principle quantum number n , the electron shells are conventionally labeled K ($n=1$), L ($n=2$), M ($n=3$), N ($n=4$), and each shell can hold a maximum of $2n^2$ electrons. Based on the idea of spin-orbit coupling, it is known that the shells with $n > 1$ are actually comprised of several different sub-levels. These sub-levels are labeled L_I , L_{II} , and so on for the $n=2$ level, with a similar labeling scheme for higher levels.

With the shell labeling scheme in mind, we can now describe the fundamental process by which characteristic x-rays are formed. This process is begun by introducing a photon or charged particle into the atom with enough energy to knock an electron out of one of the inner shells. This requires that the incident photon or charged particle has enough energy to overcome the binding energy of the electron in the atom. The atom, missing an electron from an inner shell, is in an excited state and will quickly return to the ground state, during which an electron from a higher shell must drop to fill the vacancy (hole), releasing a well defined quantum of energy equal to the energy difference of the two levels involved. This quantum of energy is released in the form of the characteristic x-ray photon or may be given to a higher shell electron, which then leaves the atom (Auger effect). Note, for a single electron originally removed from the atom, that many characteristic x-rays may be released as an electron moves to fill a hole in a lower level, leaving behind another hole which must be filled. This filling process continues until the outer shells are reached, and a characteristic x-ray is emitted for each transition made. Figure 9 is a schematic diagram showing some of the possible electron transitions inside the atom along with the conventional notation for the most common characteristic emission lines (adapted from [18,19]).

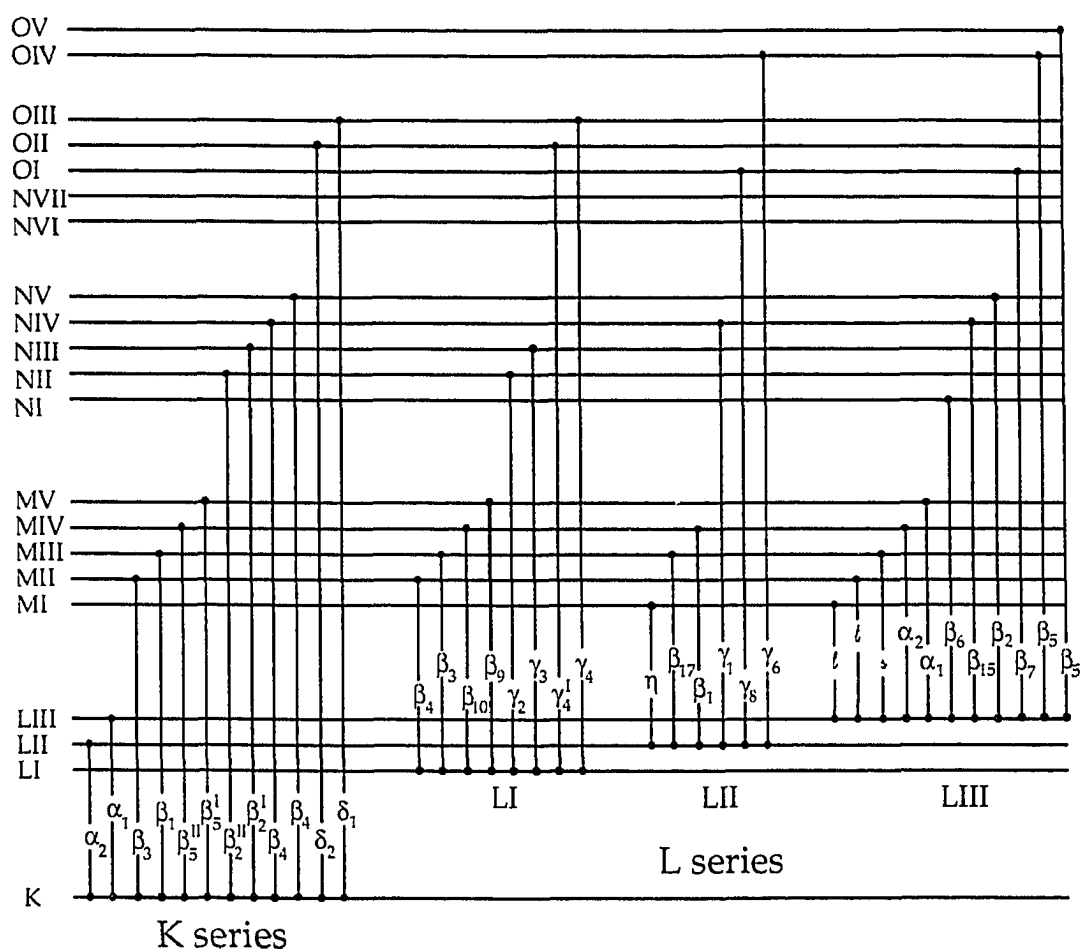


FIG. 9. Schematic diagram of the most common electronic transitions.

The actual energy level values, and hence their spacing, is unique for each atom and depends on the number of protons in the nucleus. When an electron from an upper shell falls to fill a vacancy in a lower shell, an x-ray photon is emitted with energy:

$$E_{\text{x-ray}} = h\nu = E_i - E_f \quad (42)$$

where h is Planck's constant, ν is the frequency of the photon, E_i is the electron's initial energy, and E_f is the final energy of the electron.

For the ^{57}Co source used in the Mössbauer experiment, the primary excitation is electromagnetic. There are three fundamental types of interactions

possible between an incident photon and an atom: the photoelectric effect, inelastic scattering (Compton scattering), and elastic scattering (Rayleigh scattering). Only the photoelectric effect creates electron holes which lead to characteristic x-rays. Photoelectric absorption occurs when the energy of an incident photon, E_γ , is completely absorbed by the atom and the resulting photoelectron is ejected from the atom. The energy of the emitted photoelectron is:

$$E_{e^-} = E_\gamma - E_B \quad (43)$$

where E_{e^-} is the kinetic energy of the photoelectron and E_B is the binding energy (critical energy) in the atom. For a photoelectron to be released, the incoming photon must be of greater energy than the binding energy of the electron in question. Figure 10 shows that the maximum probability for the creation of a photoelectron occurs just above the critical energy (or just below the critical wavelength, where photon energy is related to wavelength by $E(\text{keV}) \cdot \lambda(\text{\AA}) = 12.4(\text{keV} \cdot \text{\AA})$).

The probability that an incident photon will be absorbed by a material is proportional to the linear absorption coefficient, μ , which is defined by:

$$N_f = N_i e^{-\mu x} \quad (44)$$

where N_i is the number of incident photons and N_f is the number of photons which pass through a sample of thickness x . The linear absorption coefficient μ is equal to the mass absorption coefficient μ_m multiplied by the density of the sample, ρ . The mass absorption coefficient is independent of the physical form (gas, liquid, or solid) of the material under investigation; however, it is dependent on the energy of the incoming photon. Figure 10 shows the relationship of the mass absorption coefficient of lead to the photon energy (data from [25]).

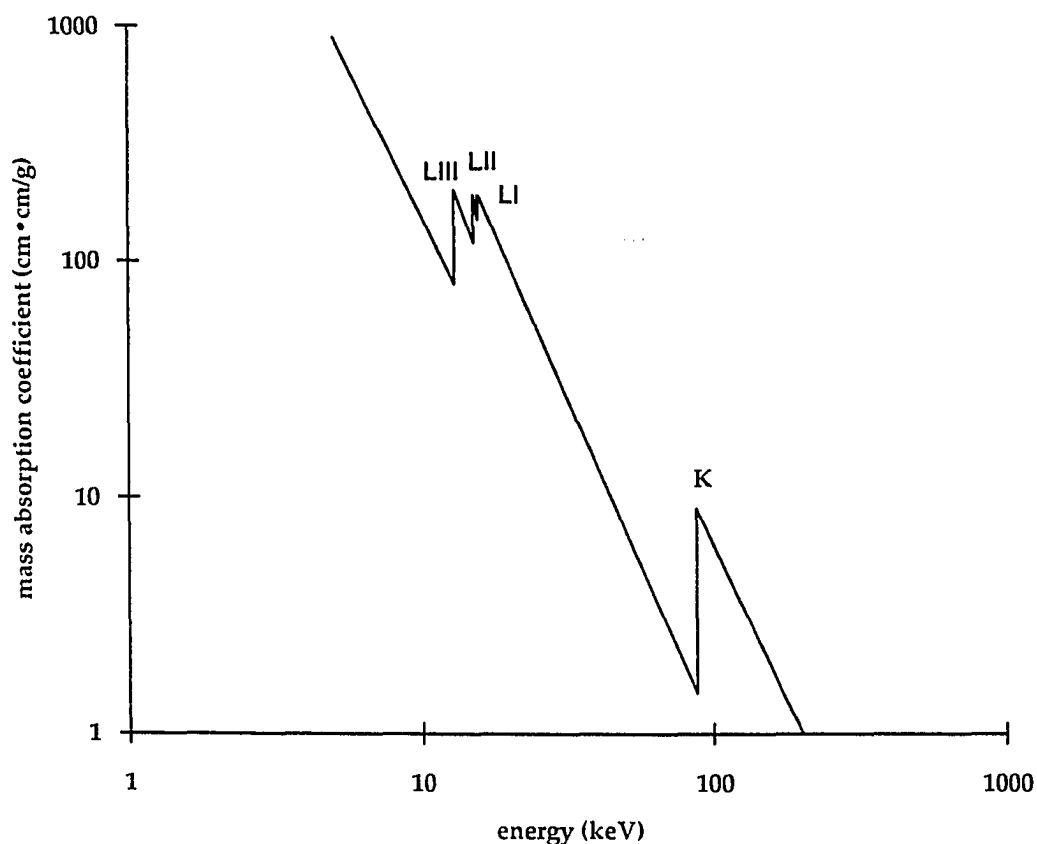


FIG. 10. Mass absorption coefficient of lead versus photon energy.

The mass absorption coefficient increases with decreasing energy. There are several discontinuities located at the critical energies for the Pb K electrons and the Pb LI, LII, LIII electrons (closely grouped). These discontinuities are known as absorption edges and, like the atomic energy level diagram, are unique for each element.

The number of fluorescence (characteristic) x-rays produced following the photoelectric effect may be reduced by the Auger effect. When an electron falls to fill a hole, there is a certain probability that, rather than creating a photon, the transition energy may be given to an outer shell electron, thus producing an Auger electron which leaves the atom with a specific kinetic energy. The hole

from the Auger electron is filled from a higher level producing a low-energy x-ray or another Auger electron.

The fluorescence yield is defined as the number of electron transitions which results in emission of a particular type of x-ray divided by the total number of such electron transitions. The fluorescence yield for K and L x-rays as a function of atomic number is shown in Fig. 11 (data from [18]). Figure 11 also shows that the probability of inducing fluorescent x-rays for elements with low atomic numbers is greatly reduced by the Auger effect.

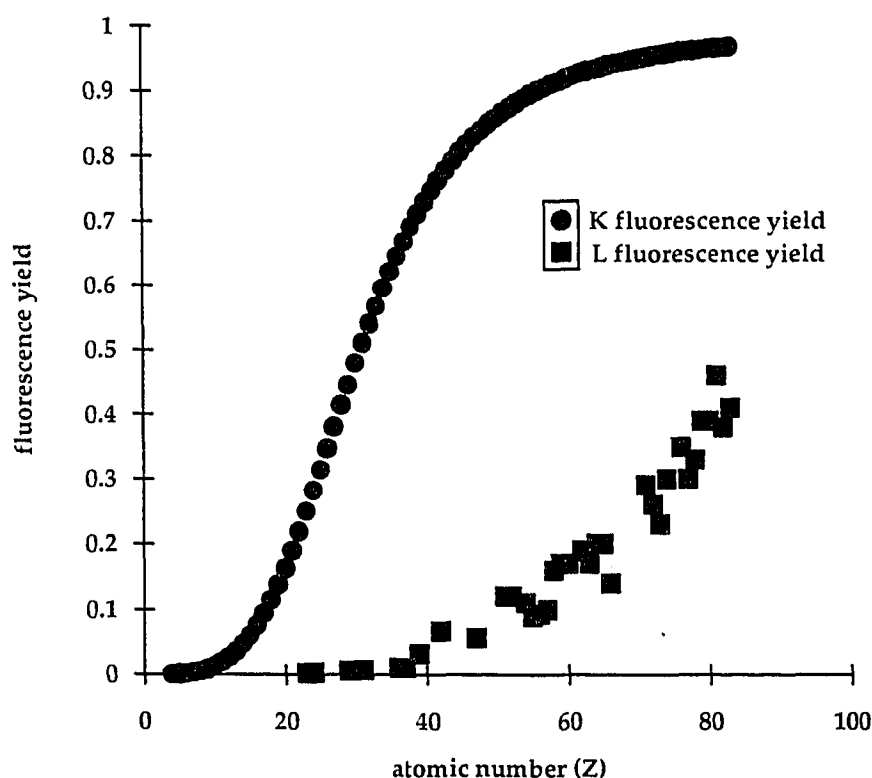


FIG. 11. K and L x-ray fluorescence yields as a function of atomic number.

The scattering of photons by atomic electrons also tends to reduce the number of interactions which leads to characteristic x-ray emission. The Compton effect occurs when the incident photon is scattered by an electron in one of the weakly bound outer shells of the atom. The photon interacts with the

electron as if it were a free electron, and the scattered photon leaves the interaction reduced in energy. The shift in energy of the photon is a function of the scattering angle, Θ , as shown in the following equation:

$$E' = E_0 \frac{1}{1 + \frac{E_0}{mc^2}(1 - \cos \Theta)} \quad (45)$$

where E' is the final photon energy, E_0 is the initial photon energy, m is the mass of the electron, and c is the speed of light. The maximum energy shift occurs at $\Theta = 180^\circ$. Table V lists the Compton-shifted energies for several of the photons emitted from a ^{57}Co nucleus at $\Theta = 180^\circ$. The difference between the initial and final energies of the photon is the kinetic energy given to the scattered atomic electron (Compton electron).

TABLE V. Maximum Compton energy shifts for some ^{57}Co emissions.

Initial energy (keV)	Final energy (keV)	$E_0 - E'$ (keV)
136.47	88.99	47.48
122.06	82.63	39.43
14.4125	13.64	0.77

Another form of photon scattering by an atomic electron is elastic or Rayleigh scattering. In this case the incident photons are scattered by tightly bound electrons without any loss in photon energy. The result of this type of scattering is therefore a simple change in photon direction.

For single-element sample material in a monochromatic photon beam, the mass absorption coefficient, fluorescence yield, and scattering probabilities may be used to calculate the intensity of characteristic x-rays given off by the sample. Conversely, the characteristic x-ray pattern emitted by a sample containing many different elements may be used to infer the elemental composition of the sample.

CHAPTER III.

EXPERIMENTAL METHODS

A. Mössbauer spectroscopy

The Mössbauer spectrometer can be effectively broken down into three main functional units: the Mössbauer velocity transducer (drive) with control system, the radiation detector with signal conditioning circuitry, and the storage and synchronization electronics. These three units are shown schematically in Fig. 12.

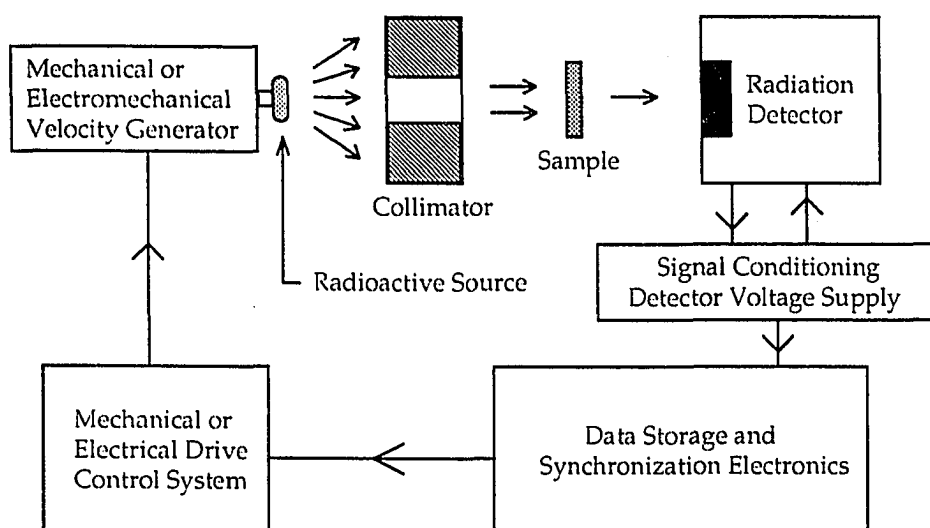


FIG. 12. Schematic diagram of transmission Mössbauer spectrometer.

From the theoretical discussion of the Mössbauer effect in Chapter II, it is apparent that unless the energy of the Mössbauer γ -ray from the radioactive source can somehow be adjusted, resonant absorption in a sample will be a rare event. For most spectroscopic techniques (Mössbauer included), one of the most important experimental components is the device used to vary the

energy of the probing radiation. For example, in the case of infrared spectroscopy, the energy dispersion device might be a high quality prism or a grating monochromator. For the Mössbauer spectrometer the corresponding instrumental component is the velocity transducer or Mössbauer drive.

The velocity transducer is a mechanical or electromechanical device which uses the Doppler effect to change the energy (frequency) of the 14.4 keV radiation emitted from the ^{57}Co source through the following relationship:

$$\Delta E = \frac{v}{c} E_{\gamma} \quad (46)$$

where v is the speed of the source (assumed to be moving parallel ($v > 0$) or antiparallel ($v < 0$) to the γ -ray direction), c is the speed of light, ΔE is the energy shift, and E_{γ} is the unshifted ($v = 0$) photon energy. For FeMS and the three interactions covered in Chapter II, velocities up to 10 mm/s ($|\Delta E| < 4.8 \times 10^{-7}$ eV) are generally required to sweep the γ -ray energy through the various resonant energies possible in a typical sample.

After the Doppler-shifted 14.4 keV Mössbauer γ -rays are emitted from the source along with the other photons shown on the decay diagram (Fig. 5), they generally pass through a collimator to form a well defined photon beam which interacts with a sample. Two main geometries may be employed in the experimental setup of a Mössbauer spectrometer, as shown in Fig. 13.

In transmission geometry, when an energy-shifted γ -ray has the precise energy needed to fulfill the resonance condition of an ^{57}Fe nucleus in the sample, the γ -ray may be resonantly absorbed. The detector, placed on the opposite side of the sample from the Mössbauer drive and source, will then see a reduction in the total number of 14.4 keV photons. The reason for the reduction is that after the resonant absorption, the following de-excitation results in another 14.4 keV γ -ray or a conversion electron and conversion x-rays, all emitted in a totally

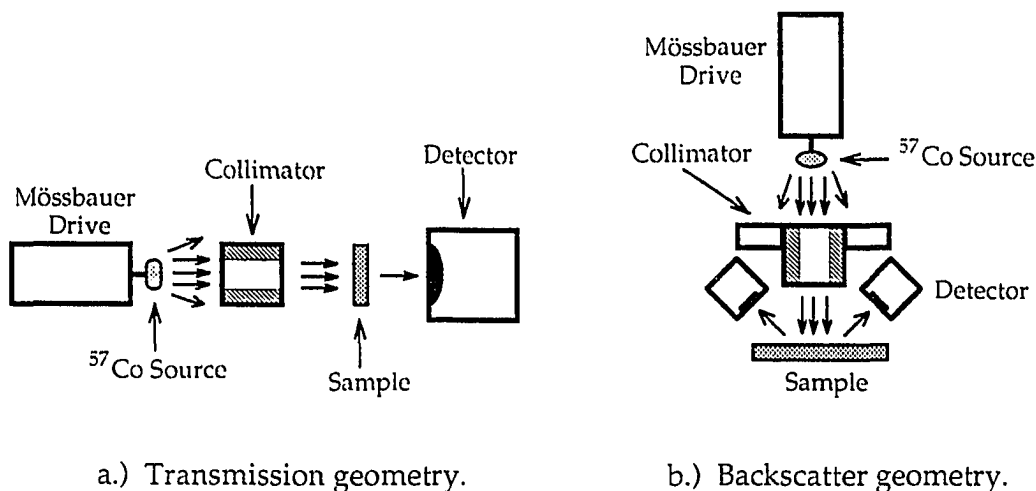


FIG. 13. Two types of geometries used in Mössbauer spectroscopy.

random direction. The conversion electron is an inner shell (usually K-shell) electron which absorbs the 14.4 keV of energy and then leaves the atom with 7.3 keV of kinetic energy ($14.4 \text{ keV} - 7.1 \text{ keV}$ of K-shell binding energy) [16]. The hole left by the conversion electron is then filled from a higher (usually L) shell resulting in a characteristic 6.4 keV (K_{α}) conversion x-ray. L and M shell electrons also have small probabilities of participating in the conversion electron interaction. The ratio of total conversion electron emission to 14.4 keV γ -ray emission is 8.25 (conversion coefficient), while the relative probability among K, L, and M conversion electrons is 81:9:1, respectively [20].

In transmission geometry, the resulting Mössbauer spectrum, which is a graph of radiation intensity as a function of Doppler velocity (shifted γ -ray energy), will show a dip in the background at the energy of resonance transitions of the sample. Transmission geometry generally requires some preparation to place the sample between the source and detector. The requirement for sample preparation is particularly cumbersome in extraterrestrial applications, and may be eliminated with a backscatter

Mössbauer spectrometer (BaMS) by allowing the instrument simply to be placed near the sample.

The experimental arrangement used in backscatter geometry is identical to the transmission case up to the formation of a beam of Doppler-shifted photons through the collimator interacting with a sample. However, after a resonance absorption event, the re-emitted radiation is collected by detectors on the same side of the sample as the incident beam (Figure 13b). Since the emission of radiation from individual nuclei (γ -rays) or atoms (conversion electrons and x-rays) is completely random in direction, the maximum radiation that can be gathered is the half directed back towards the instrument. It is then necessary to use an array of detectors or one large detector capable of gathering nearly all of the radiation coming off the sample in the backscatter direction. The resulting Mössbauer spectrum from a BaMS instrument shows peaks in the radiation intensity at the location of any resonant transition of the sample. The BaMS geometry is also optimized for x-ray fluorescence spectroscopy, which may be performed concurrently with Mössbauer spectroscopy.

B. Historical development of the velocity transducer

Nearly all of the early Mössbauer drives shared one characteristic: they were operated at constant velocity. The result of this characteristic was that in order to study a range of Doppler velocities, several experiments would have to be performed, each at a different velocity. A major drawback of this type of system is the inconvenience of resetting the instrument for each velocity (perhaps a hundred or more values) which would make single sample spectrum automation very difficult. Additionally, the lack of reproducibility of single velocities due to long-term drift would tend to compromise the experiments. The early drives could generally be classified in terms of the motions they produced as rotational or translational devices.

Two types of rotational Mössbauer drive systems are shown schematically in Fig. 14 (adapted from [26]).

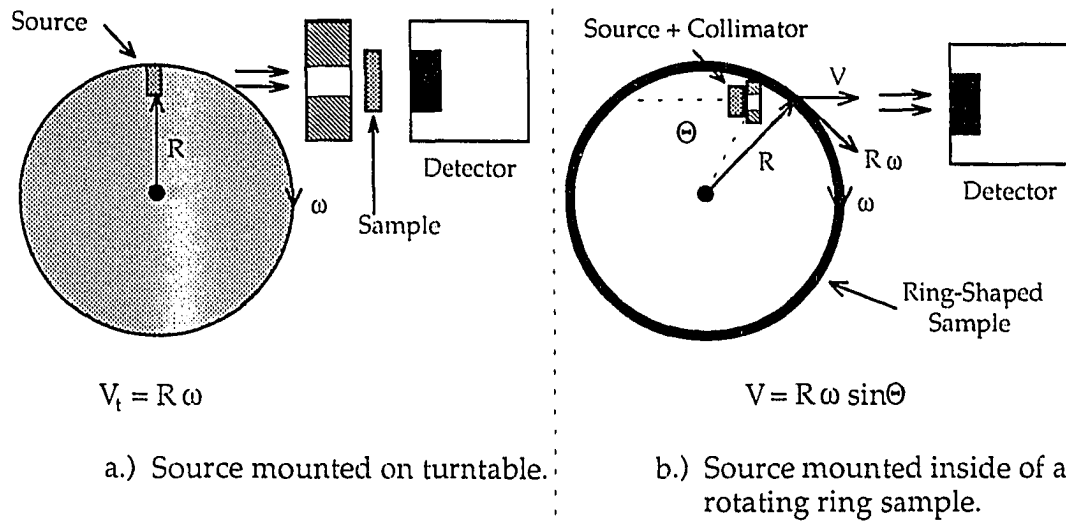


FIG. 14. Schematic diagram of two rotational Mössbauer drives.

The Mössbauer drive of Fig. 14(a) consists of a turntable on which the radioactive source is mounted. It is the type used by Mössbauer in his original work [27]. With the use of a collimator as shown, the Doppler velocity is equal to the tangential component of the turntable's uniform circular motion. The drive shown in Fig. 14(b) was used to rotate a ring shaped sample around the source and collimator, located off the central axis of the ring. The Doppler velocity of this system is equal to the component of the tangential velocity parallel to the line between the source and detector. This arrangement represents an improvement in the original system used by Mössbauer in that data could be collected continuously, rather than only when the source is aligned with the collimator.

The most successful early drive of translational design was based on the mechanical lead-screw system employed in most lathes. A schematic diagram of a transmission Mössbauer spectrometer using the lead-screw arrangement is

shown in Fig. 15 [26]. The lead-screw drive could be configured with a moving source and stationary sample as shown, or with a moving sample and stationary source.

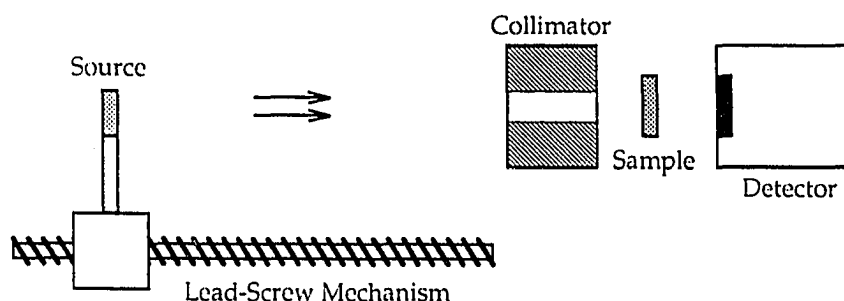


FIG. 15. Schematic diagram of lead-screw Mössbauer drive.

Due to the need to automate and improve the stability of Doppler velocities for a single Mössbauer spectrum, experimenters were quick to design systems which could periodically sweep through a range of velocities. Early mechanical designs of this fashion were based on slider-crank or cam-follower mechanisms. The difficulty with these mechanical systems is that they generally produced distorted sinusoidal velocity waveforms due to sticking and slipping of the system. It is desirable to sample each Doppler-shifted energy with equal weight, which requires the use of a triangular velocity waveform, for which the velocity varies linearly with time each half cycle. The need for a transducer which could generate triangular velocity waveforms led to the use of electromagnetic feedback systems as velocity drives.

The first electromagnetic transducer used was nothing more than a high quality audio loudspeaker [26], thus "loudspeaker-type" is a term given today to the electromechanical drive. Improving on the design of quality loudspeakers, E. Kankeleit designed a two-coil electromechanical device with feedback specifically for use as a Mössbauer drive [28,29]. The basic design of the Kankeleit Mössbauer drive is shown in Fig. 16 [29].

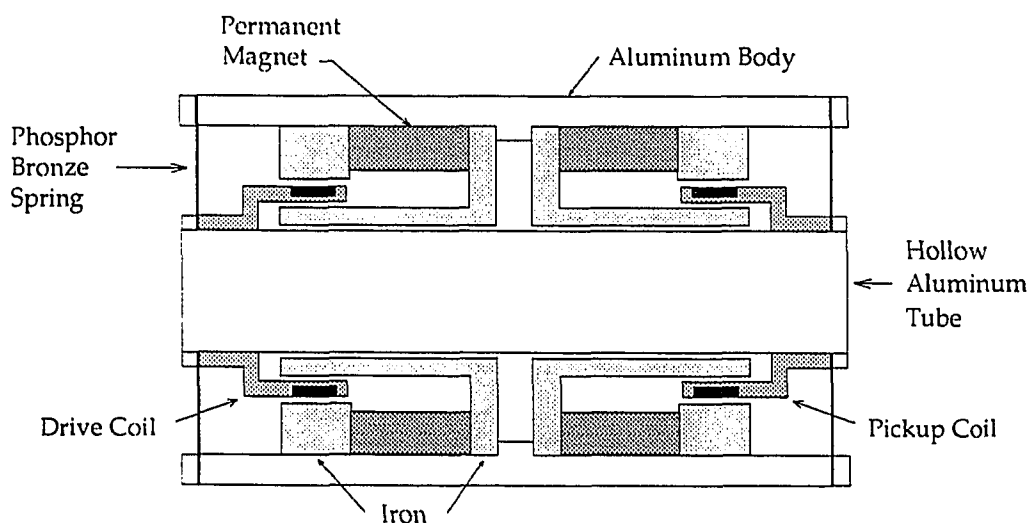


FIG. 16. Kankeleit Mössbauer drive construction.

The Kankeleit drive operates when a voltage corresponding to the desired velocity waveform is applied to the drive coil. A current is established in the drive coil which is perpendicular to a radial magnetic field, creating a force which moves the central portion of the drive (both coils, central aluminum tube, and springs) in a given direction. A restoring force is applied by the springs mounted on both ends. In order to maintain the desired motion, a pickup coil is used as part of a negative feedback system [29].

C. Modern Mössbauer drive with control electronics

The standard laboratory Mössbauer drive is a two-coil loudspeaker-type transducer similar to the original design by Kankeleit. A typical laboratory drive (Ranger Scientific VT-700) has a volume of nearly 1000 cm^3 , a mass greater than 2 kg, a resonant frequency of less than 10 Hz, and consumes around 15 W of peak power.

The Mössbauer experiment begins when a continuous periodic square-wave signal (synchronized with the data storage device) is received by the drive control electronics. This square-wave signal is then fed into an integrating

circuit using a long time constant to produce a triangular velocity reference signal. This reference signal then passes to the drive coil of the velocity transducer, starting it in motion. A separate pickup coil in the drive then sends a signal representing the actual velocity waveform of the drive's motion to a difference circuit which subtracts this pickup signal from the reference signal (negative feedback), producing an error signal. This error signal is then amplified and sent back to the drive coil. It is necessary to use a negative feedback circuit to force the drive to operate in a mode other than the natural sinusoidal motion of any harmonic oscillator system. The feedback circuit also corrects for any long-term drift in the electronics or mechanical operation of the drive. The result of the feedback circuitry working with the drive is that the Mössbauer γ -rays are periodically Doppler-shifted in energy in a pattern that follows a triangular waveform.

D. Radiation detector and signal conditioning circuitry

Another important device used in spectroscopic techniques is the radiation detector for the appropriate energy range. The standard radiation detectors employed in the laboratory Mössbauer spectrometer are single-wire gas-filled (for example, Xe 95%, CO₂ 5%) proportional counter tubes. These detectors are typically two inches in diameter by six inches long and require about 1600 V for operation. An energetic photon from the sample under investigation enters the proportional counter detector and creates an electron via the photoelectric effect with a gas molecule. The resulting photoelectron then creates a small cloud of electrons through further collisions. The large positive bias (voltage) applied to the small diameter central wire in the detector creates a Coulomb force which then pulls the electrons towards the wire. Near the wire, the electric field is high enough to cause the electrons to move with sufficient kinetic energy to ionize additional gas molecules, which is the heart of the gas

multiplication effect. When the cascade of electrons reach the positively charged wire they create a pulse of charge (very small current) on the high voltage wire supplied to the detector. The detector high voltage is connected to a preamplifier which serves to convert the charge collected in the detector into a small voltage which is then amplified to produce pulses of sufficient voltage for later analysis.

E. Multichannel analyzer (MCA)

The data storage function of the Mössbauer spectrometer is typically accomplished by a multichannel analyzer (MCA). The front end of most MCA systems contain single channel analyzers (SCA) which act essentially as a gate allowing only those voltage pulses that are in a specified range to pass through (double comparator circuit). Generally the SCA is set such that only those voltage pulses which correspond to 14.4 keV γ -rays are allowed to pass through. This process is referred to as setting the window. In order to set the window, the MCA is operated in the pulse height analysis (PHA) mode which presents the user with a graph of radiation intensity versus energy. The upper and lower level discriminators (the two sides of the window) are adjusted by comparison with the pulse height spectrum.

After the window has been properly set, the MCA is then operated in the second of its two modes, the multichannel scaling (MCS) mode. The MCS is a time-oriented mode of operation that opens a counter for a set period of time, counts the number of pulses which come through the SCA during this time, and then stores the total number counted in a memory channel. When one time period (dwell time) is completed, the MCS steps to the next memory channel and repeats the counting process, storing the result in this new channel. MCS's are generally configured with 128 through several thousand memory channels, with

dwell times from 10 μ s through several seconds. This step and count process is cycled through the entire memory group, until interrupted by the operator.

During this process, the high-order address bit is monitored. As an example, in a 128 channel MCS, the address bit which represents 64 will be zero volts (low) until the MCS reaches channel 64, at such time the 64 bit will be five volts (high) and remain high through the second half of the memory. The repeated scanning of the memory channels by the MCS has the effect of creating a square-wave voltage that changes value at the beginning and at the midpoint of each MCS sweep. It is this square-wave (midpass-out signal), automatically synchronized with the MCS, that is integrated in the Mössbauer drive circuitry to form the triangular velocity reference signal.

The result of this rather complex chain of events is that a graph (Mössbauer spectrum) is built up over time which represents the number of photons counted in a unit of time (radiation intensity) as a function of the velocity of the drive (Doppler-shifted γ -ray energy) as discussed below.

F. Typical Mössbauer spectra

It is now of interest to investigate the three interactions discussed in Chapter II and illustrate the appearance of the Mössbauer spectrum for each. The first interaction discussed was the isomer shift. This interaction shifts the resonance energy by a unique amount, from the reference value of the bare nucleus, to a new value depending on the chemical environment of the nucleus in the sample. For positive isomer shift, the resulting single-line Mössbauer spectra for the two experimental geometries are shown schematically in Fig. 17.

The next interaction discussed was the electric quadrupole interaction. This interaction removes some of the degeneracy of nuclear levels allowing, in the simplest case, two resonant absorptions to occur. Figure 18 is a schematic diagram of the Mössbauer spectrum resulting from quadrupole splitting.

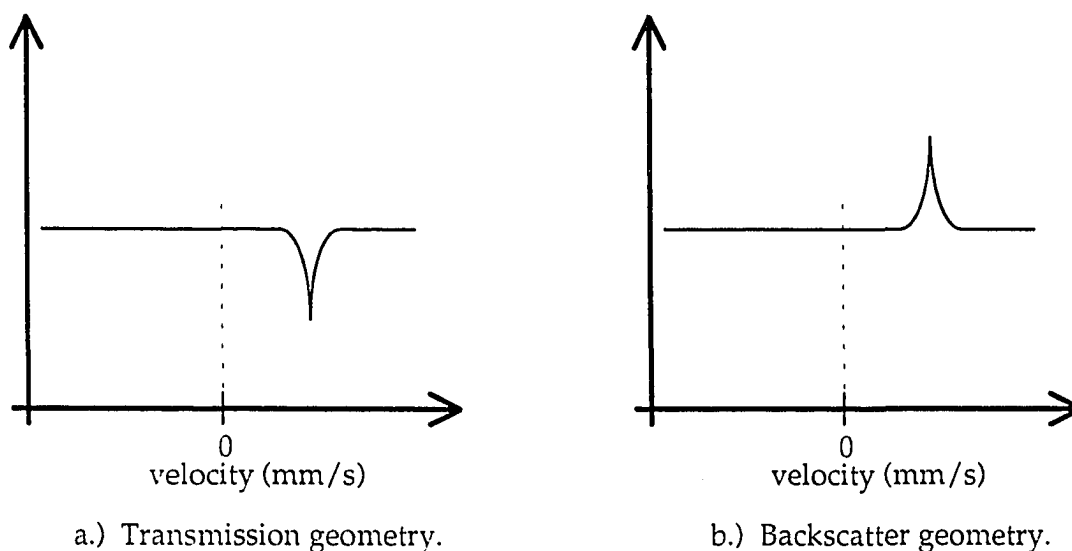


FIG. 17. Schematic Mössbauer spectra of the isomer shift interaction.

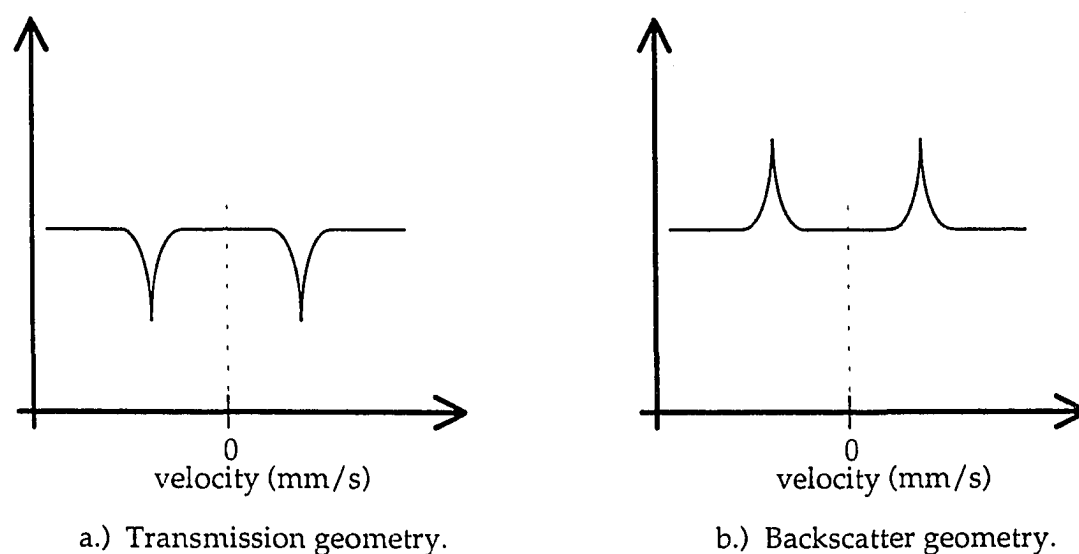


Figure 18. Schematic Mössbauer spectra of the electric quadrupole interaction.

The third and final interaction discussed, the magnetic dipole interaction or Zeeman effect, removes all degeneracy from the $I = 1/2$ and $3/2$ nuclear levels and results in six different resonant energy transitions. The Mössbauer spectrum for this interaction is shown schematically in Fig. 19.

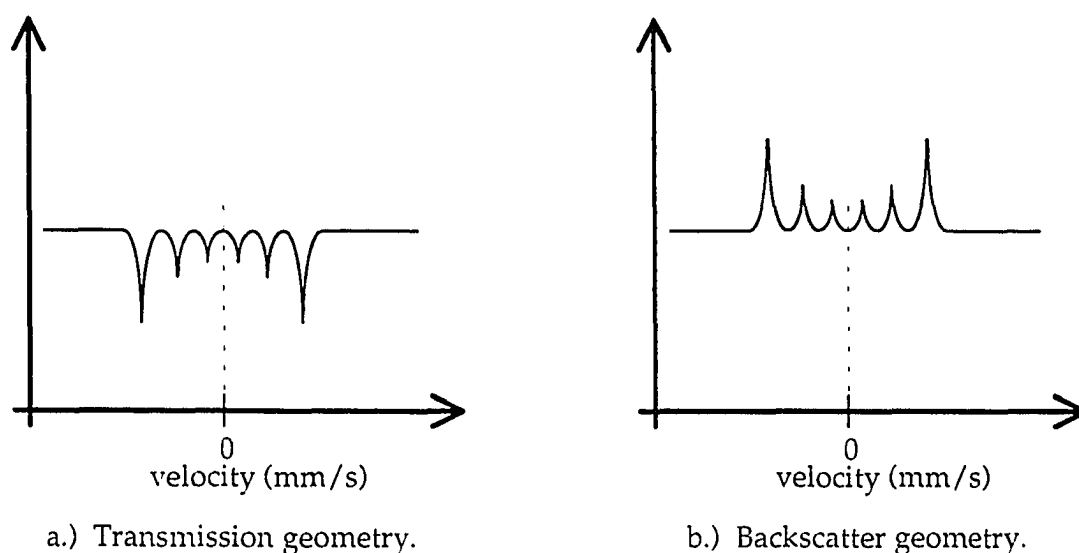


FIG. 19. Schematic Mössbauer spectra of the magnetic dipole interaction.

G. X-ray fluorescence (XRF)

The experimental setup of the BaMS instrument is the same as the setup required by x-ray fluorescence. The ^{57}Co Mössbauer source is also an excitation source used in XRF. The major fluorescing photons of this source are the 14.4 keV, 122.06 keV, and 136.47 keV γ -rays (indicated in Fig. 5), as well as the 6.4 keV Fe K_{α} (^{57}Fe from ^{57}Co) and 20.21 keV Rh K_{α} (Rh matrix) characteristic x-rays. The diversity of the emitted radiation from the ^{57}Co source makes it a good choice for elemental analysis over a wide range of atomic numbers. A thin aluminum filter is generally used to filter out any 6.4 keV Fe x-rays from the source so that the sample may be analyzed for iron content.

The characteristic x-ray peaks of elements in a sample are recorded in the same PHA spectrum used in the Mössbauer spectrometer to set the window with the SCA. Therefore, all that is necessary to make a combined BaMS/XRF instrument is that a copy of the PHA spectrum, with the SCA window fully open allowing all detectable photon energies to pass, be sent to a separate memory group.

CHAPTER IV

RESULTS AND DISCUSSION

A. Mössbauer drive system

At the beginning of this project we began testing solid-state positioning devices as possible candidates for use as compact rugged velocity transducers. The invention of the scanning tunneling, atomic force, lateral force, and magnetic force microscopes have created a large expanding market for small, very precise, and repeatable positioning units for the microscope stages. These small translators are currently based on two similar solid-state effects, the piezoelectric effect and the electrostrictive effect. In the piezoelectric effect, an electric field applied over the crystal will cause an elastic strain in the crystal resulting in a change in one of the crystalline dimensions. Interestingly, the reverse effect is also possible in that if the crystal is strained, it will produce a voltage. The amount of change in the crystal's size is proportional to the applied electric field and the crystal expands or contracts along the direction of the field. In the electrostrictive effect the amount of displacement is proportional to the square of the electric field and the crystal only expands. The amount of change in the crystal's size is usually quite small so, to achieve displacements on the order of micrometers, many layers of the material are stacked together with alternating electrodes such that the individual displacements add together. We have tested both a piezoelectric and an electrostrictive transducer for use as a Mössbauer drive.

The piezoelectric transducer tested was a multi-element lead-zirconate-titanate (PZT) translator [Micro Kinetics CT-6156-25] with a maximum excursion of $26.5\text{ }\mu\text{m}$ at 1250 V. Since a triangular velocity waveform may be considered to be the Fourier sum of sinusoidal components, the PZT's response to a single sinusoidal signal (simplest case) was analyzed. The PZT was attached to a standard two-coil Mössbauer drive and the pickup coil of this drive was used to measure the response of the PZT to the input sine wave. The construction of the multi-element PZT transducer and the manner in which it was attached to the two-coil drive are shown schematically in Fig. 20 below.

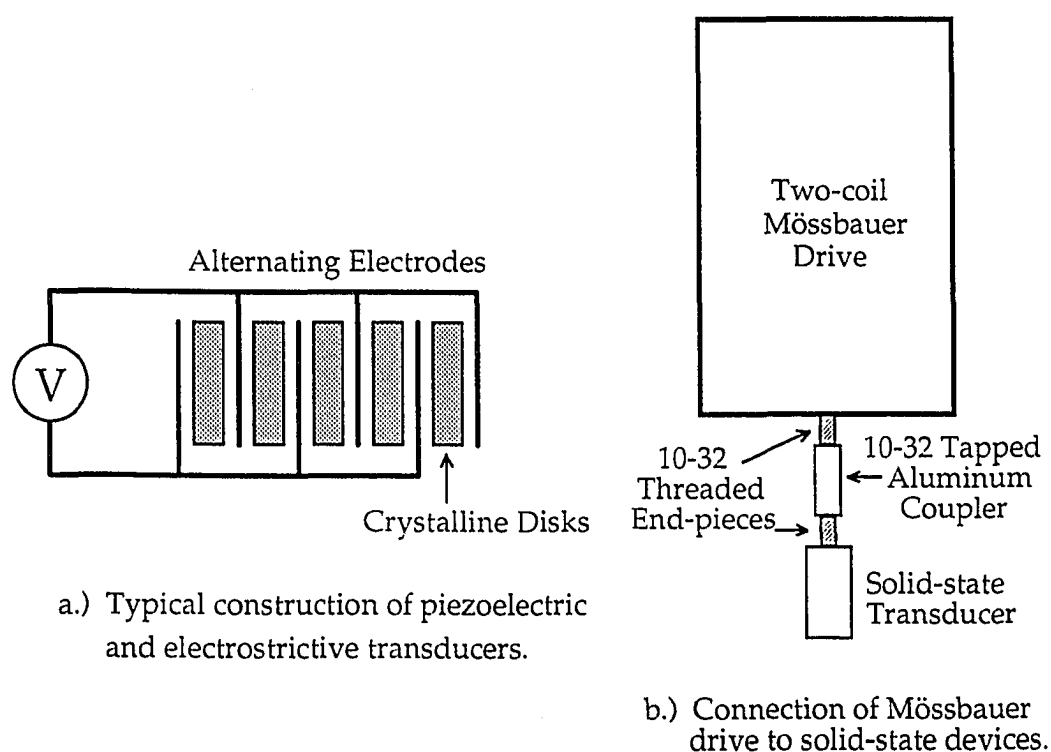


FIG. 20. PZT transducer construction and connection to Mössbauer drive.

The PZT was tested over a wide range of frequencies and amplitudes of the sinusoidal input signal. The response measured using the pickup coil of the standard drive was not linear. Rather than well behaved sinusoidal motion, a multifrequency motion that was dependent on both the frequency and

amplitude of the input signal was observed [30]. This poor response was unexplainable by the manufacturer, and we decided to abandon the PZT.

Next, we tested an electrostrictive transducer [Queensgate MT45] made of lead-manganese-niobate (PMN) capable of 45 μm excursions at 175 V. This device was constructed in the same fashion as its PZT counterpart, and was characterized using the same measurement scheme. Although not as pronounced, a similar non-linear response as the PZT was measured for the PMN. The PMN manufacturer felt that the poor response was due to the PMN power-amplifier's inability to maintain the motion at large excursions at the tested frequencies.

With the two solid-state transducers tested, it became obvious that without some kind of active feedback it would be nearly impossible to force the devices to move sinusoidally, much less make them move in a parabolic fashion (parabolic position versus time implies a triangular velocity waveform). Another reason for active feedback is that the response of both types of translators are documented in the manufacturer's literature to change as a function of temperature. Queensgate has recently started offering PZT and PMN systems with capacitive feedback correction; however, the power requirements of solid-state systems are on the order of 1.5 to 2 W, nearly the total available to a complete BaMS/XRF planetary instrument. Based on this information and the fact that others have reported similar problems, another approach was tried.

Having measured the phase and frequency response of the standard two-coil loudspeaker-type Mössbauer drive in preparation for the solid-state transducer study, it was felt a miniature version of this drive could be built that would meet the requirements of the BaMS instrument. This approach was begun by designing, machining, and testing a miniature single-coil Mössbauer drive. The details of the miniature drive's construction are shown on plate 1 in

Appendix A. The miniature drive represents a 90% reduction in both volume and mass compared to the typical laboratory drive.

All of the loudspeaker-type drives tested in this work were characterized using a small sinusoidal input signal (~ 200 mV peak-to-peak) on the drive coil, and analyzing the signal from the pickup coil using a lock-in amplifier [SR530, Stanford Research Systems, Inc.]. The raw data from each measurement is listed in Appendix D. For reference purposes, the measured response of a standard laboratory Mössbauer drive (constructed at Cal. Tech., 1970) is shown in Fig. 21.

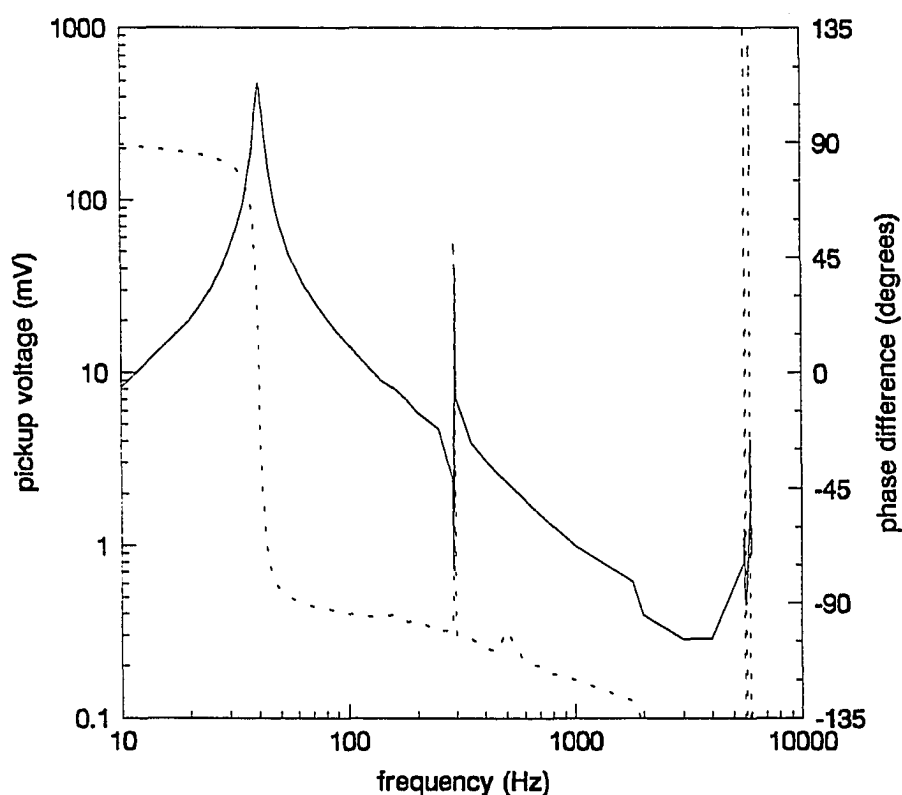


FIG. 21. Amplitude and phase response of a standard laboratory drive.

The response of a loudspeaker-type drive is that of a harmonic oscillator, as expected, and the standard drive tested had a resonant frequency of 40.3 Hz as shown by the solid line (pickup voltage) in the figure. The phase shift of the standard drive is $\pi/2$ below the resonant frequency, f_R , zero at f_R , and $-\pi/2$ above

f_R as shown by the dotted line (phase shift). The response of this drive agrees with the theoretical response of the forced harmonic oscillator system [31]. Of interest in Fig. 21 are the additional resonances shown near 300 Hz and 5.8 kHz, which are due to undesirable mechanical resonances as a result of the drive's construction.

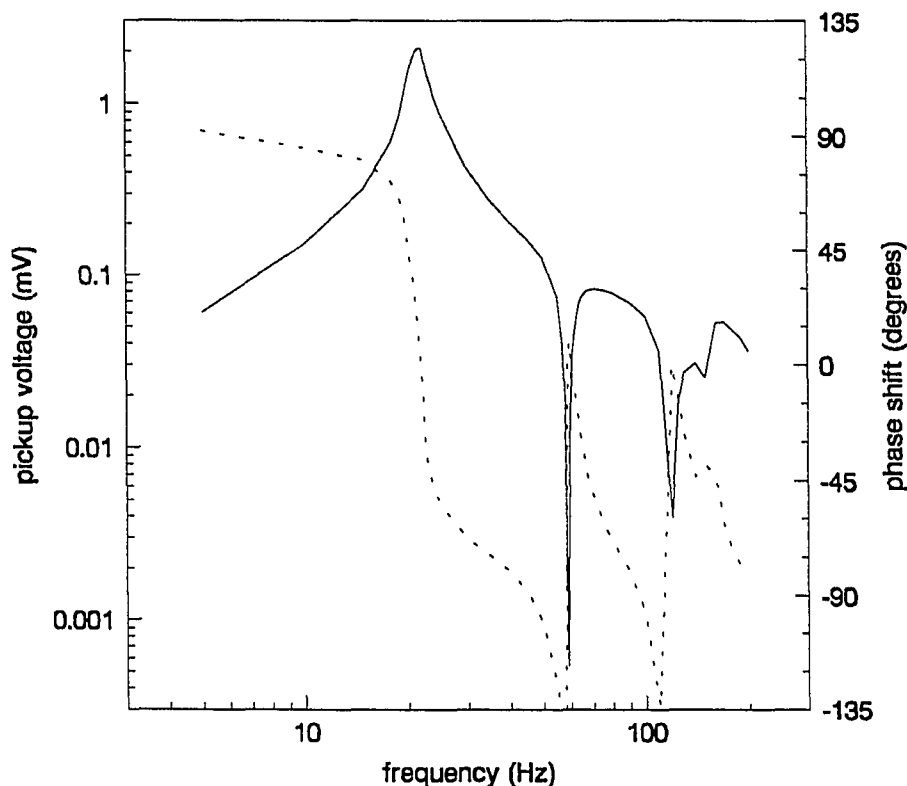


FIG. 22. Miniature single-coil drive response.

Figure 22 above shows the response for the miniature drive. Since the miniature drive was a single-coil device (Appendix A, plate 1), a magnet was attached to the moving shaft of the drive and a dual 3600 turn coil was placed perpendicular to the magnet's motion as a pickup coil for measurements. This technique proved to be quite noisy. The two dips in the pickup amplitude at 60 Hz and 120 Hz were due to the band-reject filters employed in the lock-in amplifier to pull the signal out of the background. Nevertheless, the

measurement shows the miniature drive has a resonant frequency of 22 Hz and generally comparable overall response to the laboratory drive. This small success gave confidence that with the expertise of the physics department's scientific instrument maker, Jerry Sewell, another stage of miniaturization could be achieved.

A "microdrive" was then designed and constructed, resulting in another 90% reduction in volume and mass. The design is shown on plate 2 in Appendix A. The microdrive represents about 1% of the original laboratory drive's volume and mass. It was designed with two coils like its larger cousin due to the difficulties experienced in trying to measure the response of the miniature drive and the need to ultimately provide precise velocity control. Two components of the microdrive, the magnets and the coils, deserve special mention here. The small magnets used were custom machined samarium/cobalt rare earth ring magnets (0.250" O.D., 0.10" I.D., 0.1" thick) created by the Dexter Magnetic Materials Division of Permag Corporation in Norcross, Georgia. These are very powerful magnets (as I quickly learned when two of them found each other from a considerable distance and shattered) with excellent stability over a wide temperature range (below liquid nitrogen). The drive coil was 64 turns of 40 gauge epoxy coated magnet wire, and the pickup coil was 642 turns of 51 gauge epoxy coated magnet wire. The 51 gauge wire is very difficult to see, much less handle and solder.

A special jig was created to help wrap both types of coils. A Gerald K. Heller GT21 laboratory mixer motor with reducing gearhead was used. The motor was controllable between 0 and 277 RPM, and to it was attached a 1/8" diameter, 4" long steel shaft using an aluminum connector with set screws. To this was attached a 6" diameter aluminum disk with two slots cut out on opposite sides (1/2" wide by 2" long). The end of the steel shaft was drilled and

tapped for a piece of 0-80 threaded rod on which the coils were placed. To count the number of turns of wire placed on the coil an infrared photogate (Pasco ME-9204A) connected to a counter/timer unit (Pasco model 8025) was employed. The slots in the rotating aluminum disk would pass through the photogate and register two counts for one complete turn of the coil. It was important to maintain a certain amount of friction on the wire as it was placed on the coil form. To supply this friction the wire was sent through a small plastic funnel with tissue stuffed around the wire.

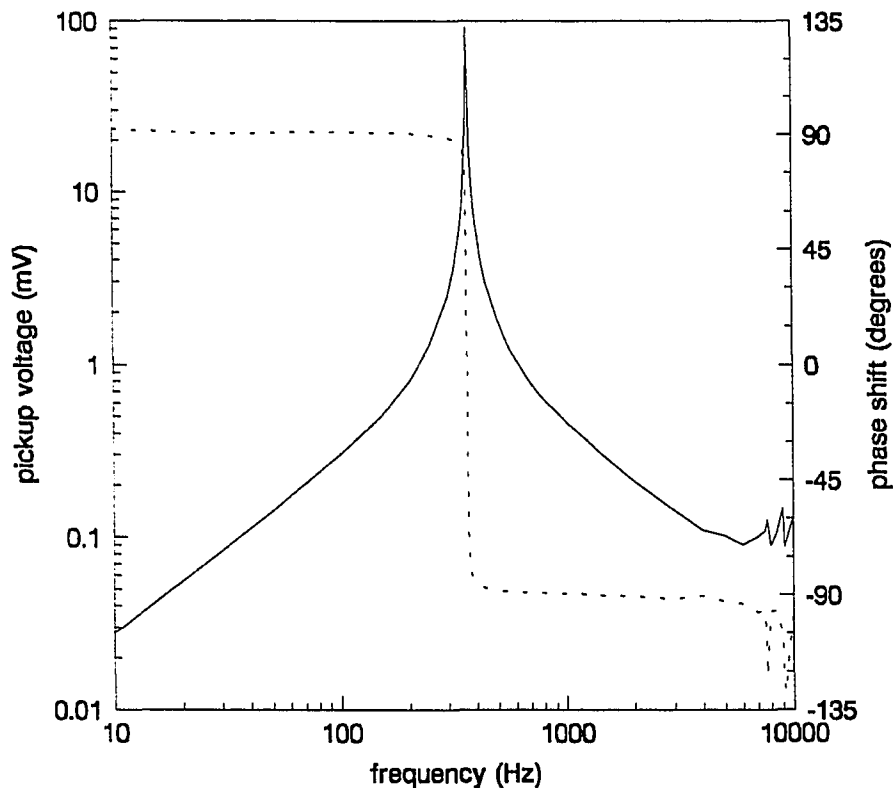


FIG. 23. Microdrive amplitude and phase response.

The measured response of the microdrive shown in Fig. 23 is superior to that of the miniature drive and the commercially available laboratory drive. The microdrive exhibits a crisp resonance at 366 Hz and shows no other resonant behavior until well past 7.5 kHz. To further investigate the motion of this drive

several objects of varying masses were attached to the central portion of the microdrive. The response of the microdrive was characterized for each mass just as in Fig. 23 and a set of data was taken regarding resonant frequency f_R as a function of moving mass, as plotted in the following graph.

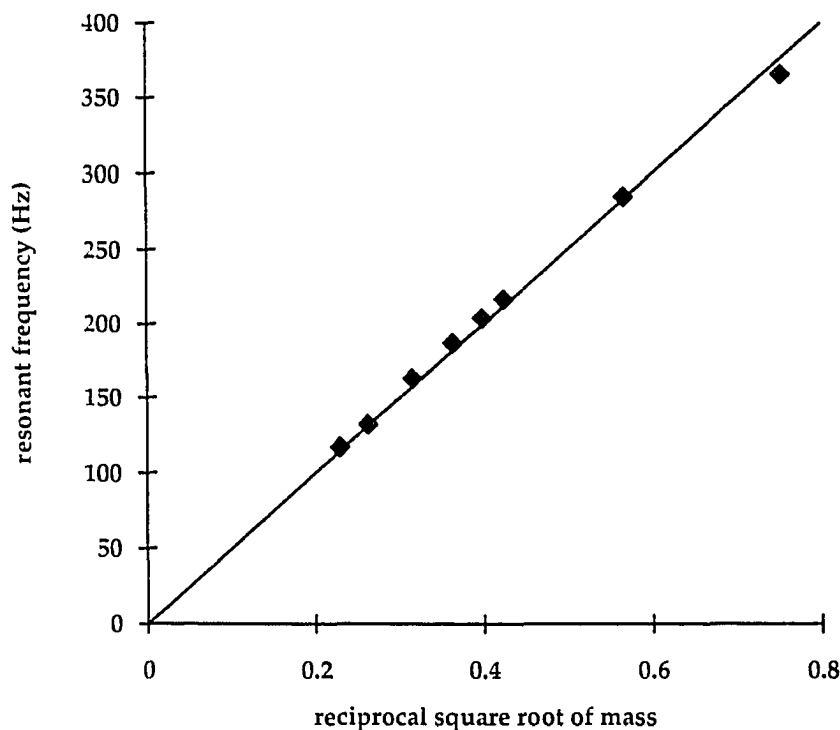


FIG. 24. Resonant frequency as a function of moving mass for the microdrive.

Since the frequency of a harmonic oscillator can be written as follows:

$$f = \frac{1}{2\pi} \sqrt{\frac{k}{m}} \quad (47)$$

where k is the spring constant and m is the moving mass, f_R is plotted as a function of the reciprocal square root of the mass. The straight line drawn in Fig. 24 represents the theoretically predicted values for the simple harmonic oscillator. This study shows that the microdrive has a spring constant $k = 9,318$

N/m, and the quality factor (or sharpness factor, equal to the resonant frequency divided by the full-width at half-max) of $Q = 657$.

In order to reduce the amount of current needed to run the microdrive at the speeds necessary for Mössbauer spectroscopy, the spring constant should be reduced. To achieve this reduction the cut of the springs was redesigned. The original (stiff) springs and the redesigned (softer) spring patterns are shown in Fig. 25, and in detail on plate 3 in Appendix A.

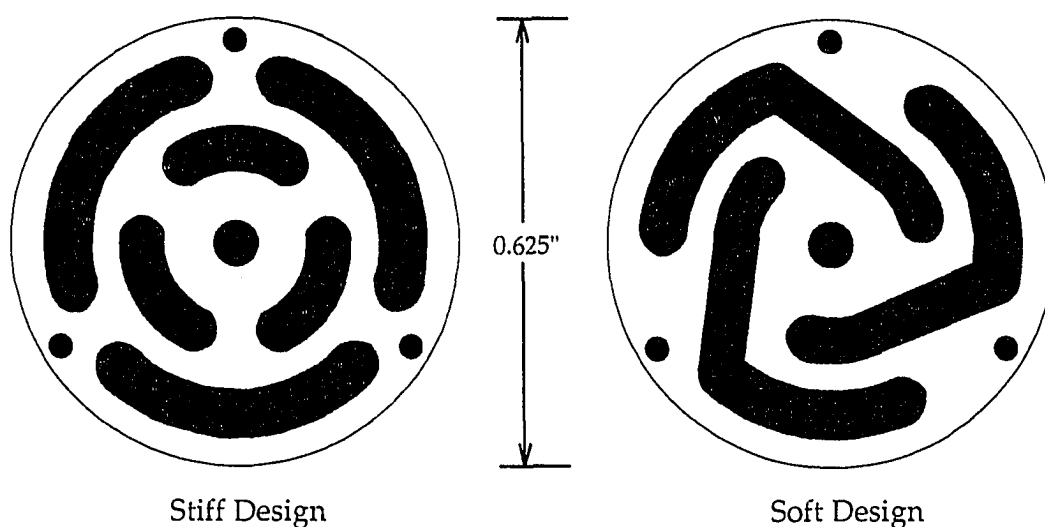


FIG. 25. Microdrive spring designs.

The response of the microdrive with new (soft) springs is shown in Fig. 26. Figure 26 shows that the microdrive using the softer spring design exhibits good frequency response, with a lack of additional mechanical resonances out to 10 kHz. The resonant frequency of the microdrive with soft springs is 168.9 Hz. The microdrive's resonant frequency was then tested as a function of moving mass with the results shown in Fig. 27. This study shows that the spring constant for the improved spring design is 2,080 N/m with a sharpness factor for the microdrive $Q = 366$. The softer springs will allow the microdrive to generate larger velocities with less total power than the original stiff spring design.

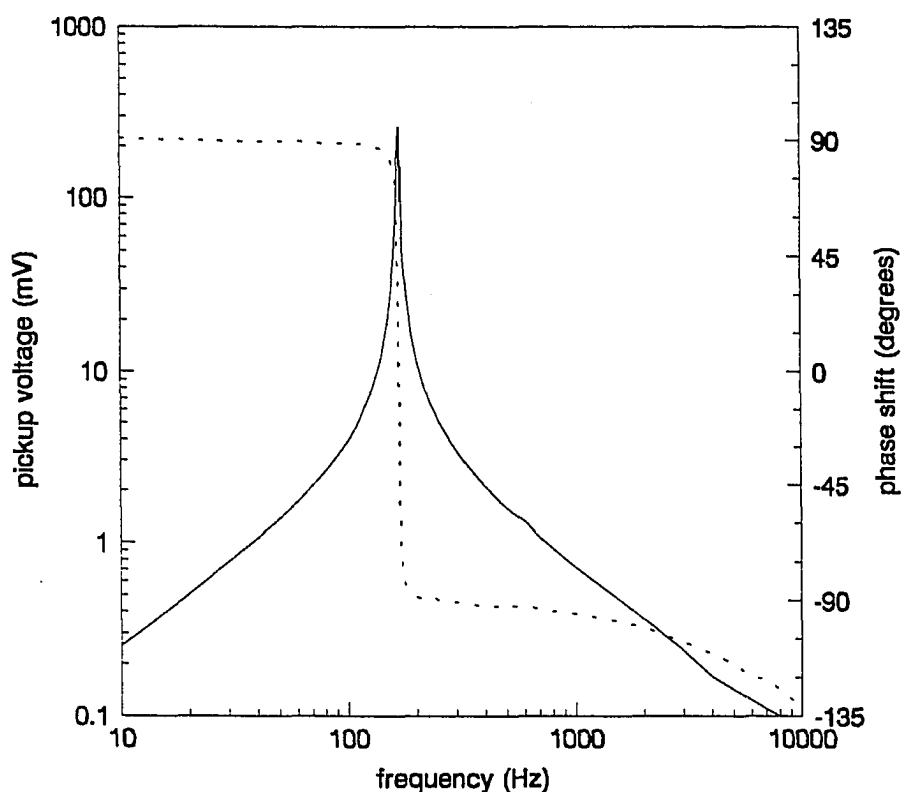


FIG. 26. Microdrive response using softer spring design.

The main operating characteristics of the microdrive with both spring designs are summarized in Table VI.

TABLE VI. Summary of microdrive characteristics for both spring designs.

Spring Design	Resonant frequency (Hz)	Spring Constant (N/m)	Sharpness Factor (Q)
Stiff	366	9,318	657
Soft	169	2,080	366

Based on the frequency response of the microdrive with soft (spiral cut) springs, we concluded that it was ready to be incorporated into the BaMS prototype instrument.

We now discuss the negative-feedback control circuitry used to maintain the triangular velocity waveform required to operate the drive in constant

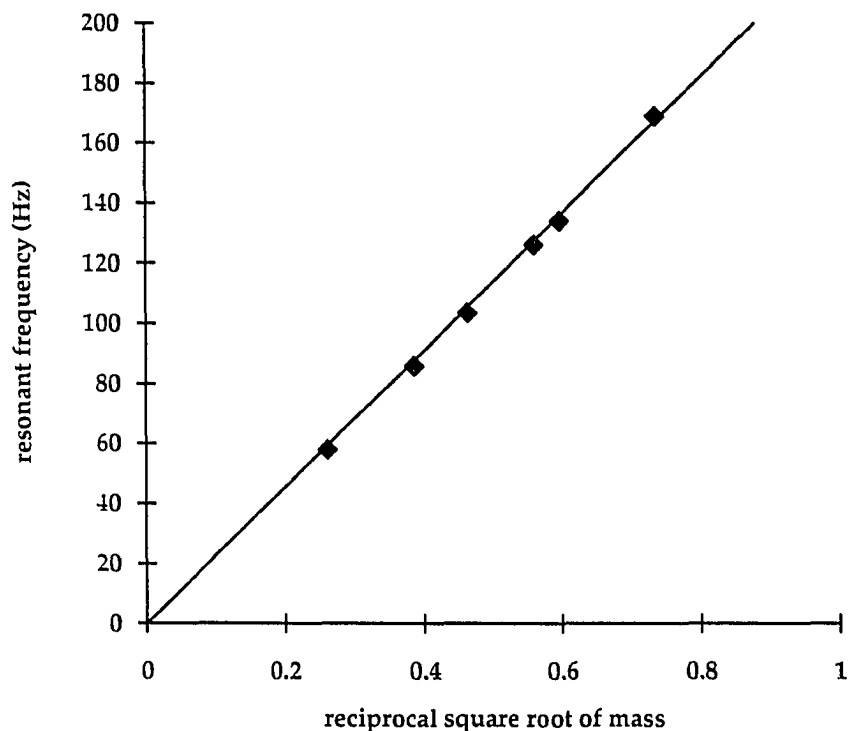


FIG. 27. Resonant frequency as a function of moving mass using soft springs. acceleration (linear velocity) mode. The drive control circuitry can be broken down into three main functional stages: the input stage, the filter stage, and the output stage, as shown in Fig. 28.

The input stage, as shown in detail on plate 1 in Appendix B, performs four main tasks. The first function of this circuit stage is to buffer the mid-pass out square wave reference (timing) signal output from the MCA. This is accomplished simply by using an operational amplifier (op-amp) in the unity-gain (buffer) mode. The purpose of this buffering stage is to protect the MCA from damage due to excessive current flow or a fault in the external circuit. The second task of the input stage is to integrate the mid-pass out square wave signal to produce a triangular signal. This triangular waveform is then used as the

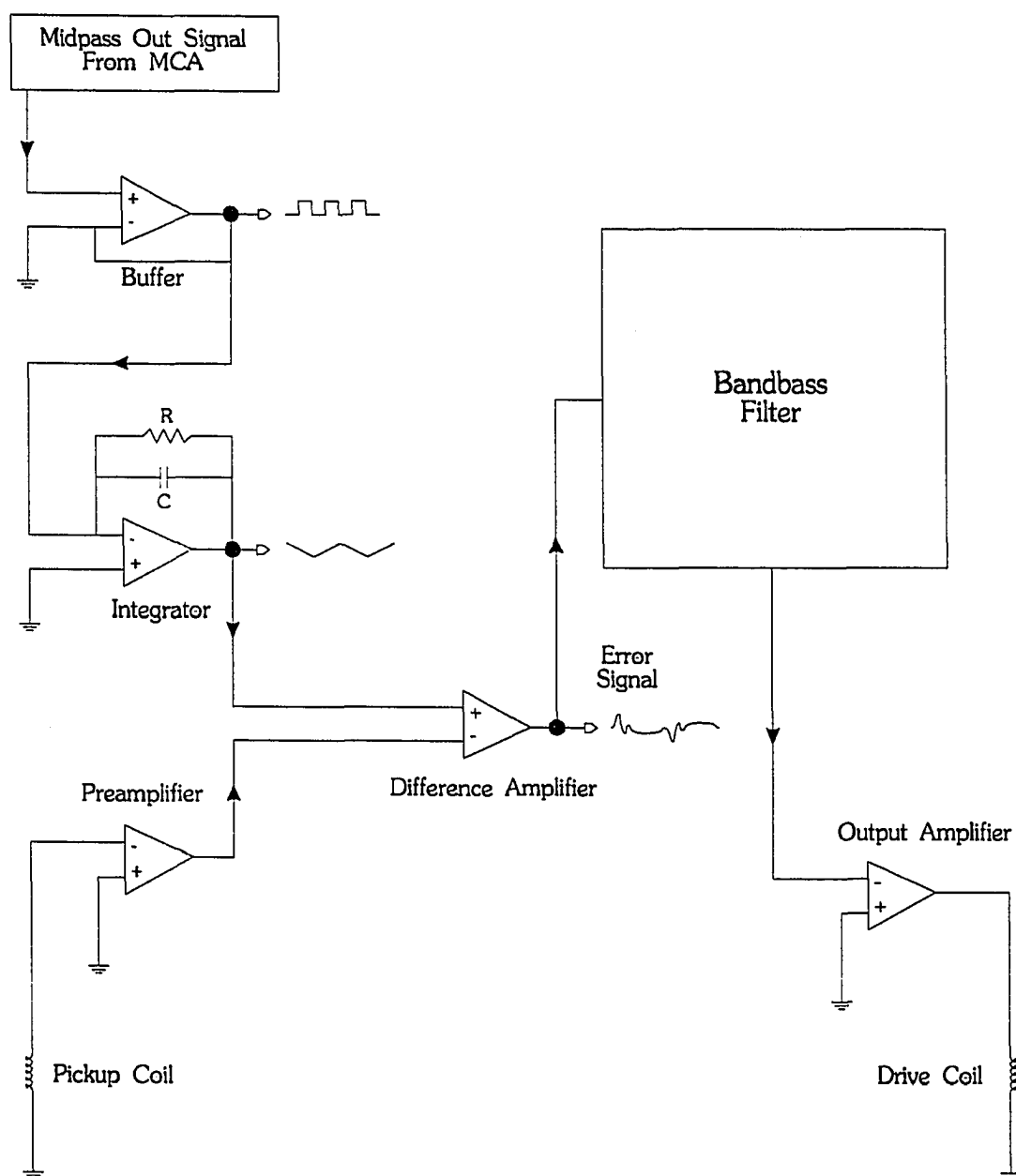


FIG. 28. Simplified schematic illustrating main functions of feedback circuit.

velocity reference signal. The third function of the input stage is a preamplifier for the drive's pickup signal. The gain of the pickup signal preamplifier is adjusted such that the peak-to-peak voltage of the pickup signal is comparable to that of the reference signal from the integrator. The fourth and final function of

the input stage is a difference amplifier which subtracts the amplified pickup signal from the reference signal, producing an error signal. The error signal is then sent to the second stage of the drive control circuit, the filter stage.

The second stage of the drive control circuit is a bandpass filter as shown on plate 2 in Appendix B. This filter performs two functions. The high-pass section, with a cutoff frequency set near 1 Hz, serves to eliminate any dc level of the error signal due to the op-amps used in the first stage. The dc level tends to drift with time and temperature, and must be filtered out before going to the third stage which is a high gain amplifier. If these dc signals were amplified and sent to the drive coil, the drive coil would receive more current than the 40-gauge wire can carry (rated at 0.185 Amps). The second function of the filter stage is the low pass part of the bandpass filter. The low pass filter's cutoff frequency is set based on the resonant frequency of the drive and the fourier synthesis program (TRIANGLE.BAS) listed in Appendix C. This program allows the user to determine how many terms in the fourier series expansion for the triangular waveform,

$$f(t) \propto \sum_{i=1}^{\infty} \frac{\cos[(2i-1)2\pi ft]}{(2i-1)^2}, \quad (48)$$

are required to produce a waveform which is linear to better than a user defined percentage over a user defined span of the waveform. Using this program, the number of terms required to fit a triangular waveform with less than 0.1% error over the central 90% of the linear portion of the waveform is 13 terms. This implies that 25 (2i-1) times the resonant frequency (168.9 Hz) or 4,222.5 Hz in frequency range is needed. The low-pass filter cutoff frequency was then chosen to be above this frequency at 5 kHz. The low-pass filter eliminates any noise present in the system above 5 kHz and prevents ringing in the output stage amplifier. Ringing may occur when the phase shift (measured by the pickup

coil) of the drive is much greater than 90° or much less than -90° , because the feedback in this region becomes positive rather than negative. Frequency components of the error signal between 1 Hz and 5 kHz are now passed to the final output amplifier stage of the drive control circuit.

The output stage is responsible for amplifying the filtered error signal and generating enough current to drive the pickup coil. The resistance of the drive coil is approximately $8\ \Omega$ and a special op-amp is required which can output more than 50 mA of current. An op-amp made by Analog Devices is suitable for this purpose. The AD842 is capable of generating currents up to 100 mA. The amplification of the output stage is adjusted to be as high as possible before the onset of ringing.

To test the completed drive control circuitry and the microdrive, a transmission Mössbauer experiment using this drive system and a $6\ \mu\text{m}$ thick natural iron foil sample was set up. The transmission Mössbauer spectrum obtained is shown in Fig. 29. Using a digital storage oscilloscope, the error signal produced in the drive control circuitry was continuously measured during the two-hour period of this experiment. The measured error signal was less than 1% of the total peak-to-peak voltage of the velocity reference signal.

B. Detector system

The first energy dispersive radiation detector examined for use as a backscatter detector in the BaMS/XRF instrument was a HgI_2 solid state detector manufactured by Xsirius Inc. of Marina del Rey, California. We studied, during a full week of experiments in California, the suitability of mercuric iodide detectors for use in the BaMS/XRF 2π backscatter detector array [32]. The HgI_2 detectors exhibit excellent resolution and are essentially 100% efficient for the photon energies of interest in this work. Figure 30 shows a pulse height

spectrum of ^{57}Co taken with a mercuric iodide detector, exhibiting the outstanding energy resolution offered by such detectors.

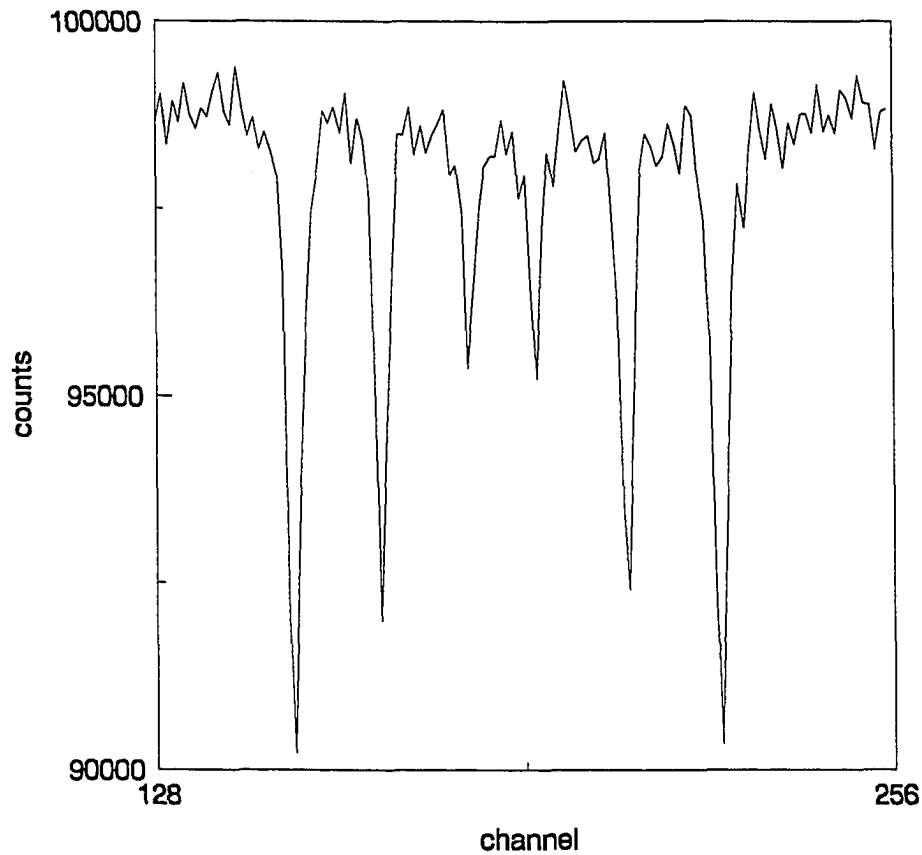


FIG. 29. Mössbauer spectrum obtained with feedback circuit and microdrive.

The resolution of the 14.4 keV γ -ray is near 4% (580 eV FWHM). The detector used in this study had a useful active area of 0.8 mm² (a very small detector) and was 480 μm thick. Experiments were also performed using three elements of a five element 780 μm thick array, giving an active area of 32 mm² (for three elements). A full series of PHA and Mössbauer spectra were taken over the course of a week, including the first transmission and backscatter Mössbauer spectra ever taken using HgI_2 . Figure 31 shows a backscatter Mössbauer spectrum taken of an enriched ^{57}Fe foil using the 3-element array.

This spectrum has been smoothed using a 3-point smoothing function to emphasize the peaks.

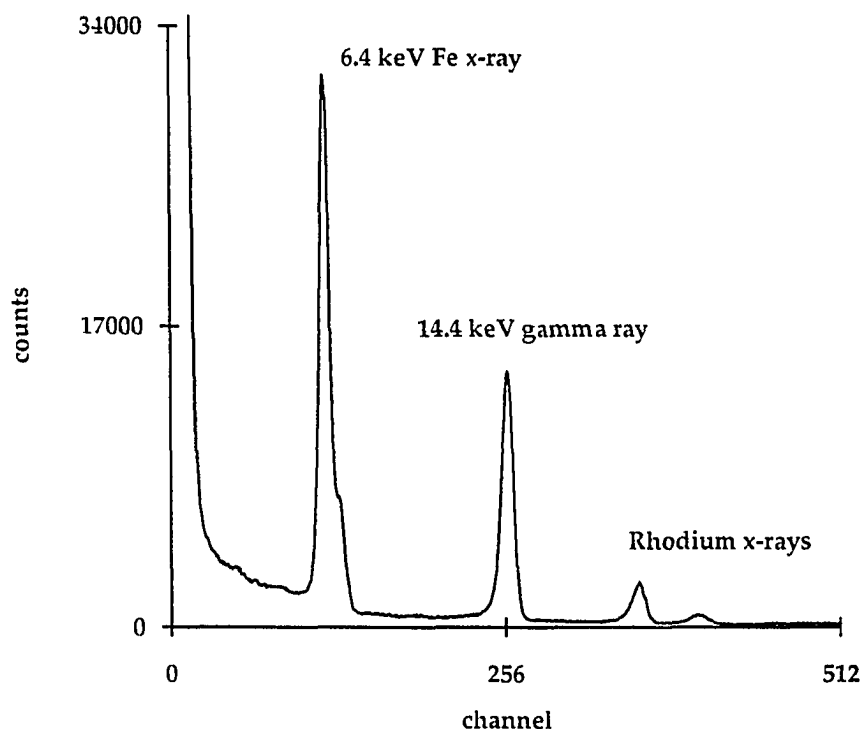


FIG. 30. Pulse height spectrum of ^{57}Co using HgI_2 detector.

The quality of the spectrum in Fig. 31 is poor due to the lack of time available for the experiment and the extremely small backscatter solid angle ($\sim 0.02\pi$ steradians) used. If a 2π backscatter surface could be tiled with HgI_2 detectors, then high quality spectra could potentially be taken quickly [32]. The high cost of HgI_2 detectors ($\sim \$10,000$ per detector) means that a tiled surface of such detectors is out of the question for this study.

A more economical approach would be to build a set of small proportional counter tubes, and distribute them in such a way as to gather as much of the 2π backscattered radiation as possible. Similarly, a single larger proportional counter could be used in which the incident radiation enters a small hole on the back side of the detector. The incident beam of photons travels

through the detector and out a large front window, where it interacts with the sample.

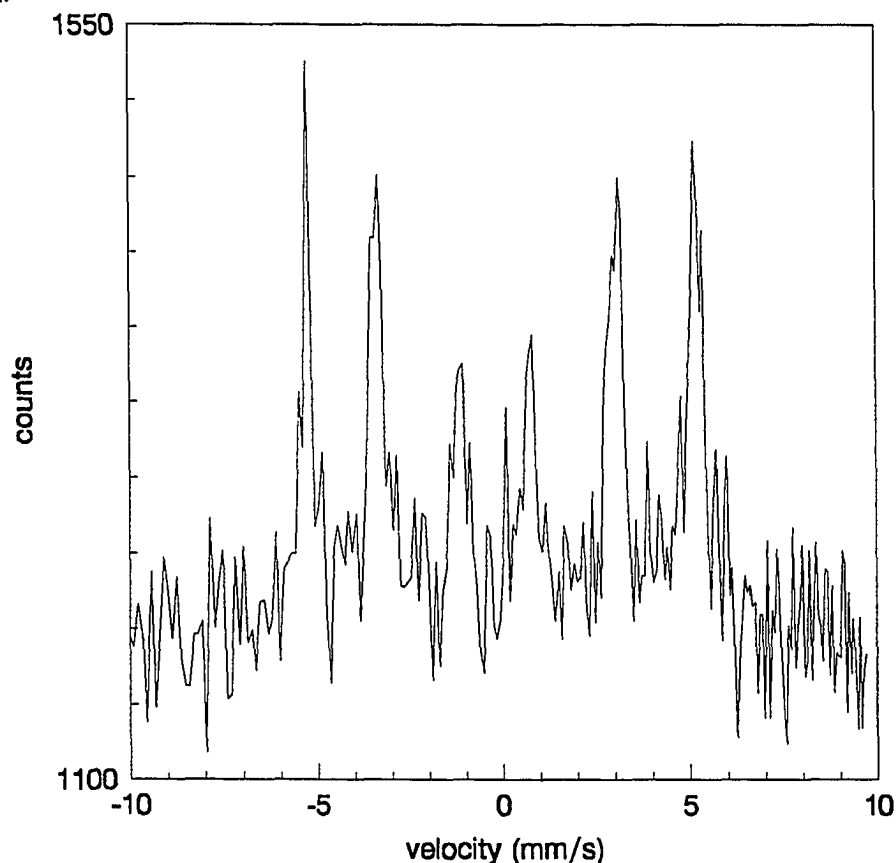


FIG. 31. Backscatter Mössbauer spectrum using HgI_2 detector array.

The backscattered radiation is then collected. We have designed and built such a system [33,34], and a schematic representation of its construction is shown in Fig. 32.

The high voltage anode used in this detector was 25 μm diameter gold-coated tungsten. The detector was filled with 1.19 atm of $\text{Ar}/5\% \text{CH}_4$, and the dimensions were chosen to optimize the collection of 6.4 keV Fe x-rays (4.3 cm thick X 4.7 cm square). A pulse height spectrum of ^{57}Co using this backscatter detector is shown in Fig. 33.

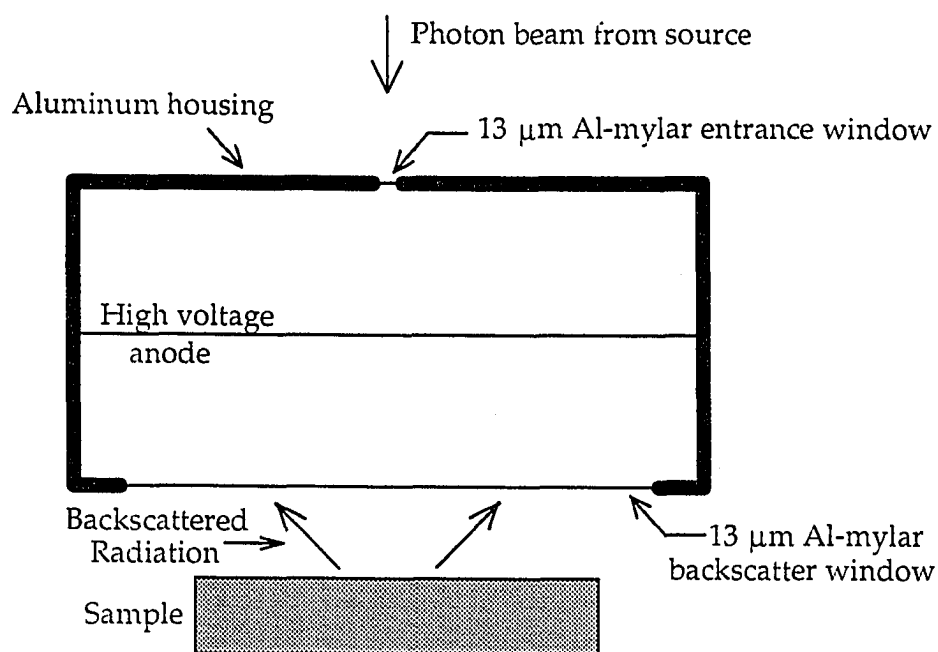


FIG. 32. Schematic diagram of 2π backscatter proportional counter detector.

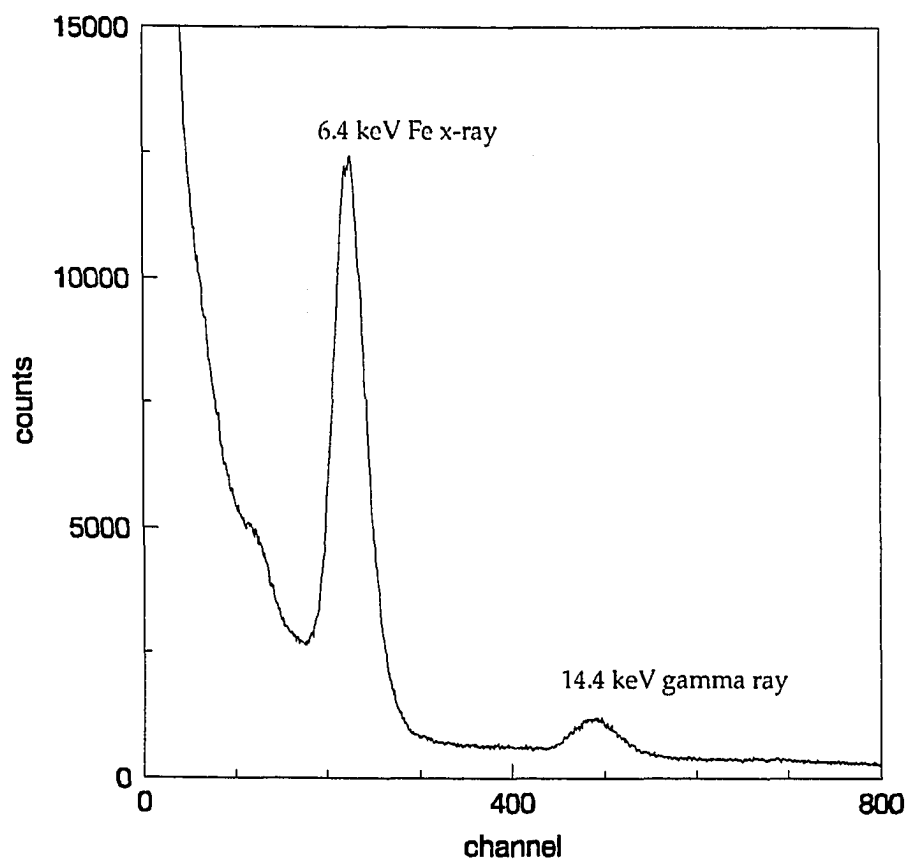


FIG 33. Pulse height spectrum of ^{57}Co using 2π backscatter detector.

The PHA spectrum shown in Fig. 33 was obtained at 1325 V and the resolution of the 6.4 keV Fe x-ray peak is 16.5%. Several backscatter Mössbauer spectra have been obtained using this detector [33,34].

The third and final type of detector system investigated in this work is the PIN silicon diode detector. This type of detector was first used in a BaMS context by a European group preparing for an upcoming Russian mission to the planet Mars [35]. These detectors are very affordable at ~\$200 for an active area of 1 cm²; therefore, an array of PIN diodes is not out of the question financially. A PHA spectrum of ⁵⁷Co using a 500 μm thick, 1 cm² PIN diode at 12°C and 160 V is shown in Fig. 34 below.

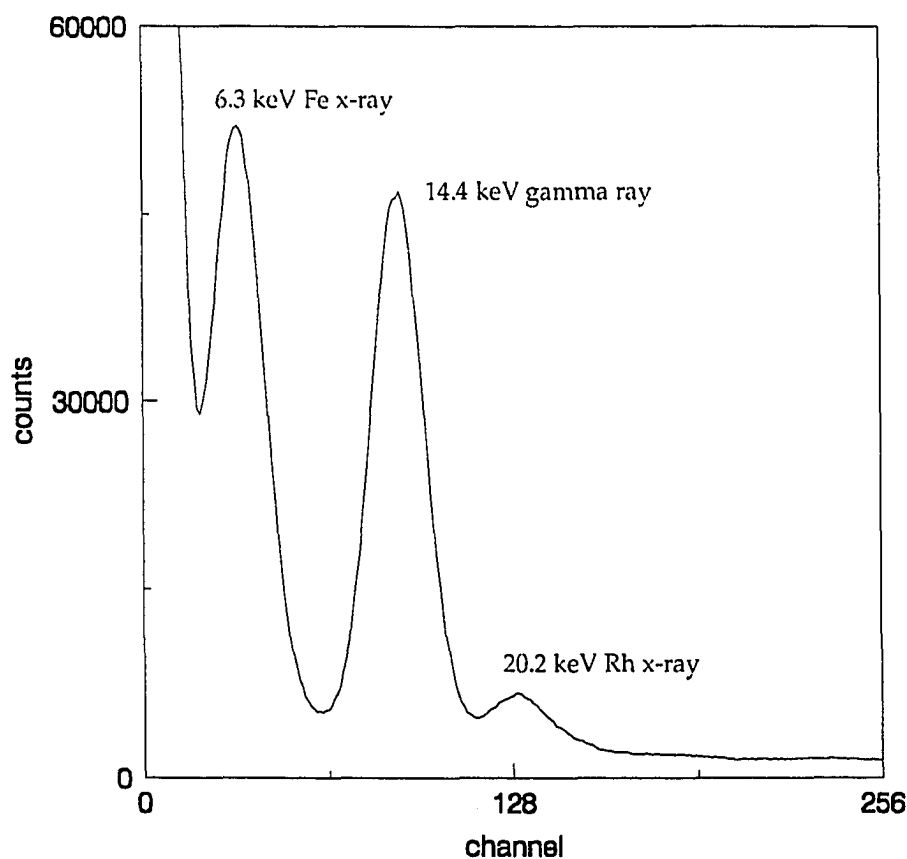


FIG. 34. PHA spectrum of ⁵⁷Co using PIN diode detector.

The resolution of the 14.4 keV γ -ray peak shown in Fig. 34 is approximately 30%. This resolution is sufficient for BaMS, but only allows for low resolution XRF. However, since the purpose of this work is to build and test a prototype "brassboard" BaMS/XRF, the instrument need not at this point be optimized for the highest resolution desirable in a flight-ready instrument. It was decided to use the PIN diode in the BaMS/XRF prototype instrument due to the diode's small size, large active area, and relatively low cost.

It is now appropriate to discuss the signal conditioning circuitry (preamplifier and amplifier) used for all the pulse height and Mössbauer spectra shown in this work to this point. The preamplifier used with the mercuric iodide detector is custom made by Xsirius and is mounted directly to the back side of the detector. This mounting arrangement has several advantages over the common practice of running a cable from the preamplifier to the detector. The main advantage of the single package detector/preamp is that the connection length from the detector to the preamp is minimized. The shorter connection helps to reduce stray noise pickup. It is critical to reduce noise on the detector end of the preamp stage, because any small noise signals will be greatly amplified in later stages and lead to a degradation of the detector's resolution. Another advantage of the single package concept is that both the detector and preamp may be easily cooled. The main source of intrinsic noise in the detector and the preamp is due to leakage current which is reduced with temperature. The signal amplifier used with the HgI_2 detector was a high quality, commercially available, Tennelec TC244 spectroscopy amplifier.

The spectra obtained with the backscatter proportional counter tube and the PIN diode were taken using commercially available components. The preamplifier used with the proportional counter detector was a Tennelec TC175, and a Canberra 2001 preamp was used with the PIN detector. The preamp

signals for both cases were then amplified using a Tennelec TC205 spectroscopy amplifier. In all cases the time constant (peaking time) of the amplifier, the amplifier's pole zero adjustment, and the detector high voltage supply (detector bias) were optimized to give the best measured resolution.

C. Complete BaMS/XRF system

Although little in the way of details is now available on the physical requirements for instruments to be included on either the Artemis lander to the Moon or the MESUR mission to Mars, one possibility is that only components of the BaMS/XRF instrument which have to do with the drive and detector systems will be mounted on an external robotic arm. The MCA and bias supply would then be mounted in the chassis of the lander. With this in mind, it is useful to divide the prototype BaMS/XRF into two physically separate units. We will call the external unit the probe, and the internal unit the body.

The probe unit contains the micro Mössbauer drive with the spiral cut springs, a PIN detector, and the detector preamp/amp (to keep the detector and preamp as close as possible). A small preamplifier/amplifier circuit has been designed and constructed by Dr. Tu Nguyen at NASA/JSC. The preamp is based on an AMPTEK A250 low noise charge-coupled preamplifier integrated circuit. Three op-amp stages follow the A250 to supply the gain and pulse shaping normally done by a separate commercial amplifier.

The drive, detector, and preamp/amp have been mounted onto a cylindrical aluminum chassis which is slightly smaller than a 12-ounce soft-drink can as shown schematically in Fig. 35. The details of the aluminum chassis construction are shown on plate 4 in Appendix A. After the PIN detector and preamp/amp are attached to the outer surface of the chassis, a 4 mil sheet of aluminum is wrapped around the chassis forming a noise-proof Faraday cage.

The microdrive with ^{57}Co source attached is simply lowered into the central shaft of the aluminum chassis and locked into place with two set screws.

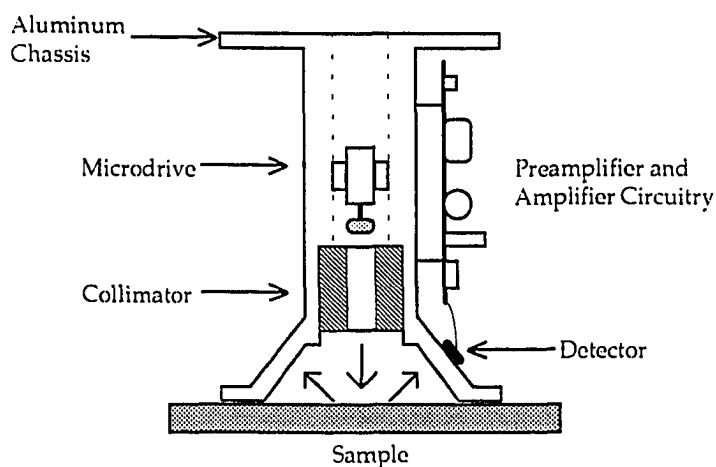


FIG. 35. Schematic diagram of component placement on aluminum chassis.

To block the radiation from going directly from the source into the PIN detector a graded shield or collimator (multilayered radiation shield) is installed in the cylindrical opening in front of the source. Based on the respective absorption x-ray edges and mass absorption coefficients (Chapter 2-B), the material and thickness used in each layer is selected to absorb nearly 100% of the x-rays produced by the preceding layer, as shown in Fig. 36. The result of the graded shield shown in Fig. 36 is that instead of 136 and 122 keV γ -rays hitting the PIN diode directly, the photons are converted (photoelectric effect) into 1.6 keV Al k_{α} x-rays, which are too low in energy for the detector to count (in the noise).

The signals from the probe unit (detector bias, microdrive signals, and amplifier output) are passed through a DB9 connector mounted on the back of the aluminum chassis, and travel through a set of small coaxial cables to the body unit. The body unit consists of the MCA, drive control circuit, and bias supply. To make the prototype BaMS/XRF as transportable as possible, all of

Element	↓ ↓	136 and 122 keV photons	Absorption edge	Thickness
Pb	↓ ↓	74.9 keV Pb x-rays	88.0 keV	67 mil
W	↓ ↓	59.3 keV W x-rays	69.5 keV	6 mil
Cd	↓ ↓	23.2 keV Cd x-rays	26.7 keV	25 mil
Cu	↓ ↓	8.05 keV Cu x-rays	8.98 keV	32 mil
Al	↓ ↓	1.49 keV Al x-rays	1.56 keV	>30 mil

FIG. 36. Schematic diagram of a graded radiation shield.

the body unit components are mounted in a portable 80386/33 MHz computer equipped with two full 16 bit and one 3/4 length 16 bit open slots. A Tennelec PCAII MCA card with 4 kbytes of memory was installed in the top full slot. The PCAII card is a double wide card, which leaves only the 3/4 length slot available, which is used to power and mount the drive control circuit and bias supply. This completes all the components necessary for a working prototype BaMS/XRF instrument. With an optional battery pack for the portable computer, the instrument is capable of making terrestrial field measurements.

The completed BaMS/XRF prototype instrument was tested on a number of Mössbauer standard samples and pure XRF targets at NASA Johnson Space Center in Houston, Texas.

To perform XRF test measurements the BaMS/XRF probe was simply placed on a number of different pure metal foils. A backscatter pulse height spectrum was then taken in this configuration. Next, the target material was removed and a reference PHA spectrum (with an aluminum target) obtained for the same amount of time as the PHA spectrum previously recorded. The

difference spectrum is the XRF spectrum of the target material with the detector noise subtracted out. The pure materials tested ranged in atomic number from copper ($Z=29$, $K_{\alpha 1} = 8.046$) to lead ($Z=82$, $K_{\alpha 1} = 74.956$). Figure 37 shows a K x-ray overlay spectrum of a series of difference spectra taken of pure materials excited by the ^{57}Co source with the BaMS/XRF instrument. ^{109}Cd (87.7 keV and 22.1 keV) and ^{55}Fe (5.9 keV) are commonly used excitation sources to study the lower Z elements ($Z=13$ to 44) [18]. In an eventual planetary instrument it would be possible to shutter either of these sources in or out to optimize the XRF data obtained.

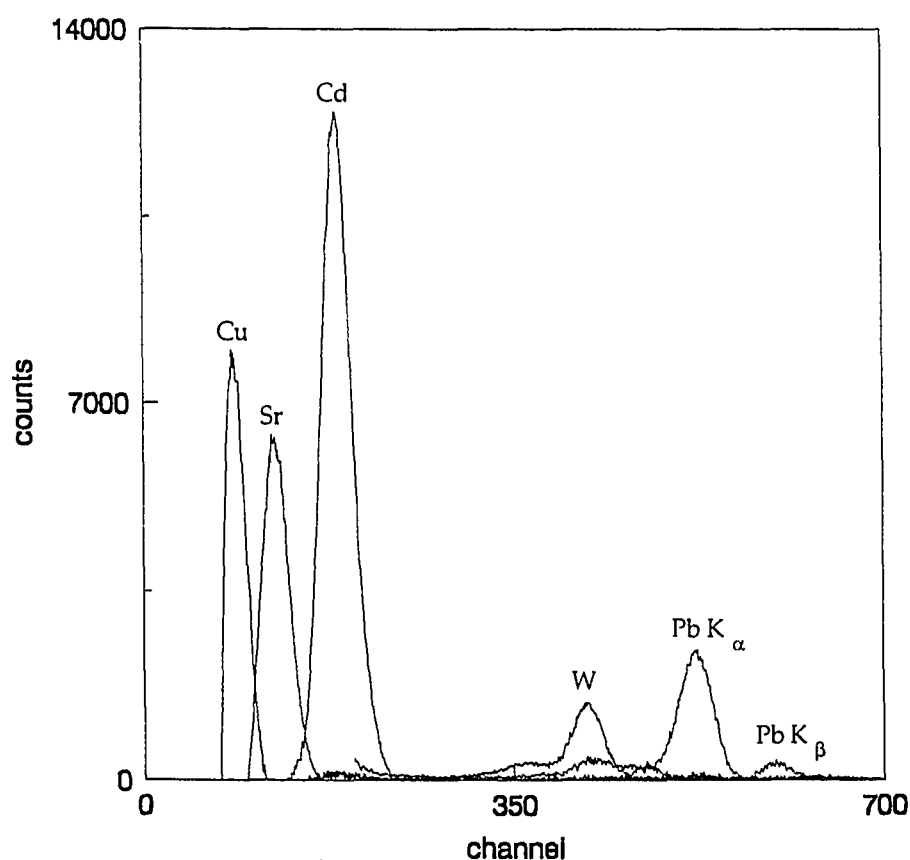


FIG. 37. Overlay of individual difference K x-ray fluorescence spectra.

To analyze a sample using backscatter Mössbauer spectroscopy, the BaMS/XRF probe is placed on or near the sample, with the sample in line with

the probing radiation. Figure 38 below is a 46-hour backscatter Mössbauer spectrum of an enriched iron foil (95% enriched in ^{57}Fe) taken with the assembled prototype BaMS/XRF instrument.

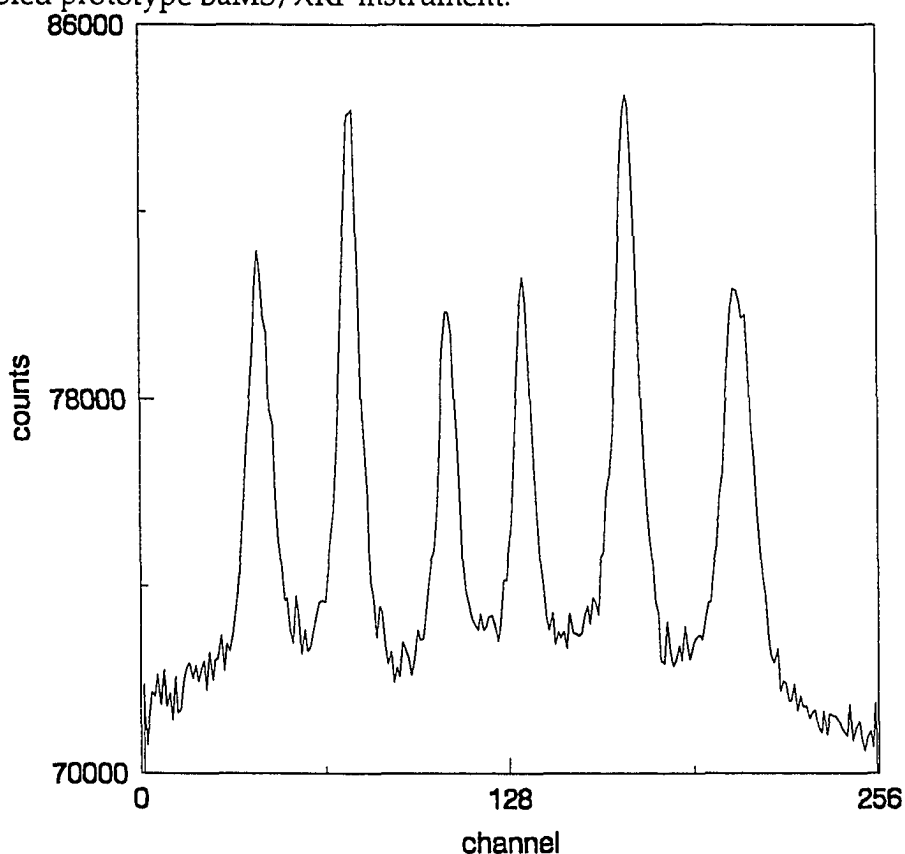


Figure 38. Backscatter Mössbauer spectrum of enriched Fe foil.

The relative intensities of the six peaks in the high-quality Mössbauer spectrum show the presence of preferential alignment of the magnetization in the foil. This agrees with the standard transmission spectrum of this sample, and is consistent with the manner in which the foil was made. The enriched Fe foil has been cold rolled as part of the foil's finishing process, which leads to preferential orientation in the plane of the foil (90° with respect to γ -ray path). The resonance linewidths are wide as compared to an Fe foil of natural abundance, due to the high number of resonant nuclei present per unit area. Since it is doubtful that an unusually high abundance of ^{57}Fe is present on the

Moon or Mars, a similar BaMS experiment was performed on a natural iron foil (^{57}Fe 2.2% natural abundance). A 51-hour backscatter spectrum of natural iron foil using the BaMS/XRF prototype instrument is shown in Fig. 39 below.

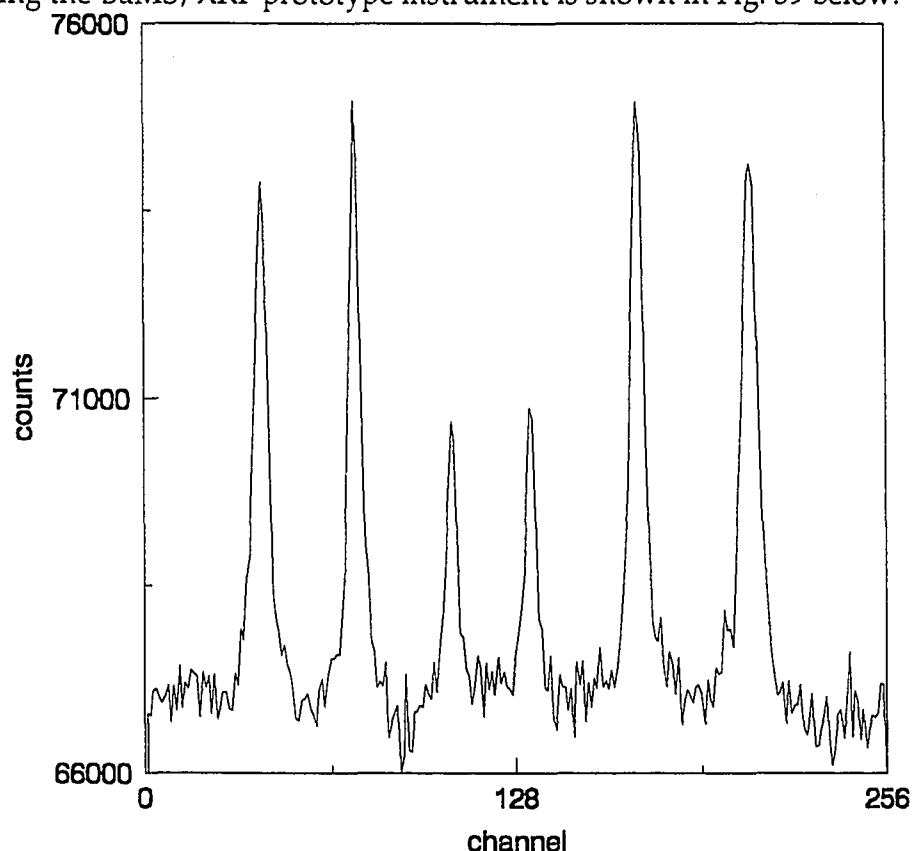


FIG. 39. Backscatter Mössbauer spectrum of natural Fe foil.

The natural iron foil has also been cold rolled as the resonance intensity pattern indicates. The number of resonant nuclei per unit area has been greatly reduced, and accordingly the widths of the peaks are much narrower than for the enriched foil.

As a final test of the BaMS/XRF instrument's Mössbauer capability, the Hawaiian palagonite sample H34 has been reexamined. Figure 40 below is a 100-hour backscatter Mössbauer spectrum of H34 taken with the BaMS/XRF prototype instrument.

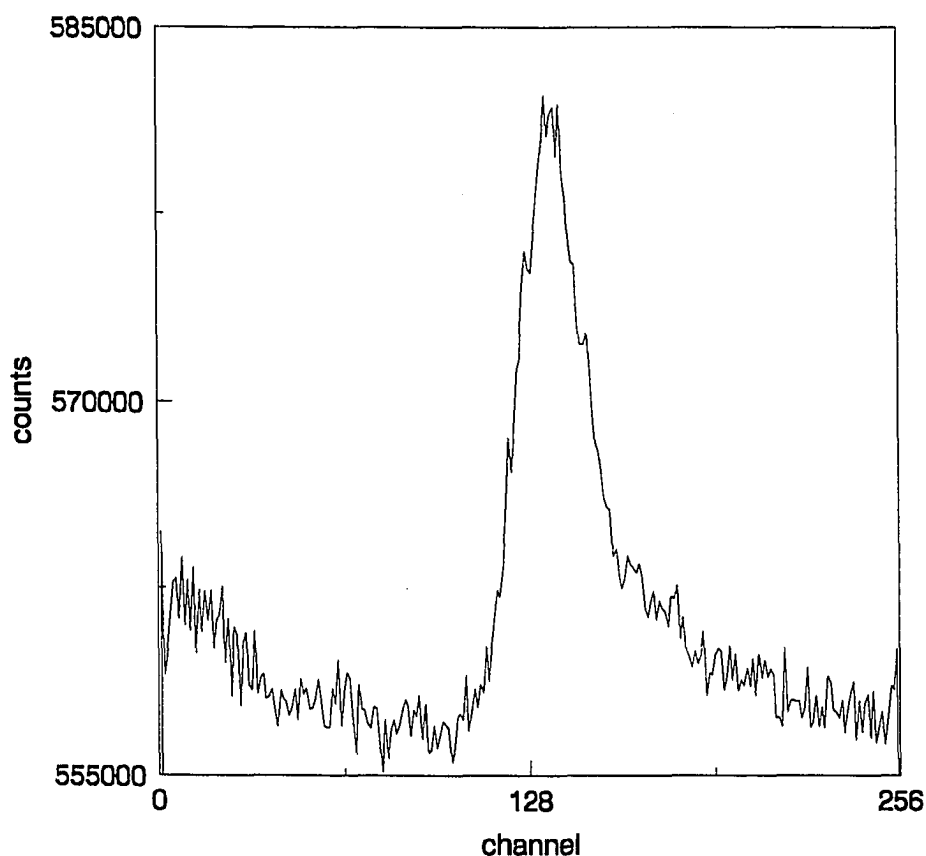


FIG. 40. Backscatter Mössbauer spectrum of Hawaiian palagonite H34.

This backscatter Mössbauer spectrum shows two broadened central doublets comparable with the transmission spectrum of this sample shown in Fig. 1. The signal-to-noise ratio of this spectrum is relatively poor in comparison with Fig. 39 due to the fact that H34 contains ~9% Fe (Viking ~13% [36]) while a Fe metal foil contains ~100% Fe. The radioactive source strength used in the BaMS/XRF prototype for these measurements was ~15mCi, while the anticipated source strength for a planetary mission would be roughly 100mCi. Furthermore, it is relatively straightforward to increase the detector solid angle in the instrument by using multiple PIN diodes. The increase in source strength and solid angle using six PIN diodes (for example) implies that a spectrum of equal quality to Fig. 40 would require ~2.5 h.

CHAPTER V

CONCLUSIONS

It has been the primary purpose of this work to produce a miniature BaMS/XRF prototype instrument to provide a foundation for the development of a flight-ready instrument to be used on an upcoming NASA exploration mission to a planetary surface. In this work we have shown that it is possible to miniaturize both the laboratory backscatter Mössbauer spectrometer and the x-ray fluorescence analyzer into a working package about the size of a 12-ounce soft-drink can. The BaMS/XRF probe has a mass of ~300 g, and consumes no more than 0.2 W of electrical power. We have surpassed the goals set at the beginning of this project. The BaMS/XRF project is now ready to proceed to the design and development of a flight-ready instrumentation package.

For a flight-ready BaMS/XRF system, there are several recommendations which can be made based on the experience with this project. One is that the detector array be constructed by tiling the backscatter surface with different types of detectors. An array of mostly PIN diodes with several mercuric iodide detectors would provide an instrument with excellent counting rates for BaMS and high resolution for XRF.

The electronics for the drive circuitry are based on components that are rated to military specifications. This means that the circuitry is radiation hardened and can be built to survive a wide range of temperatures. The flight-ready electronics will be required to meet these specifications. More importantly, the entire drive circuitry should be hybridized into a single integrated component. Similar hybridization should also be applied to the

The flight-ready electronics will be required to meet these specifications. More importantly, the entire drive circuitry should be hybridized into a single integrated component. Similar hybridization should also be applied to the detector's preamplifier and amplifier circuitry, and this package should have the detector mounted directly on it. The MCA should function like a computer with the PHA and MCS modes handled by software routines. These routines can be stored in electrically erasable programmable read only memory chips (EEPROM's) which could be remotely reprogrammed to handle any unforeseen problems that may arise. Enough memory should be included with the system to store many Mössbauer and XRF spectra so that, for example, the BaMS/XRF instrument would not have to wait for uplink time to Earth to dump data before more data could be collected. Laboratory MCA systems generally have ~8 kbytes of memory, while 16 megabytes of memory can currently be purchased on a single inline memory module (SIMM).

The materials in the construction of the prototype BaMS/XRF instrument were chosen based on availability and ease of use and machining. The flight-ready instrument will need materials which can withstand the rigors of a space flight including large temperature variations, exposure to vacuum and possible planetary atmospheres, and the stress and vibrations associated with the flight itself. It may be necessary to use a mechanical device to fix the moving portion of the microdrive to avoid damaging it on impact. The flight-ready package will be required to pass the so called "shake-and-bake" series of mechanical and temperature tests like any other package sent into space.

REFERENCES

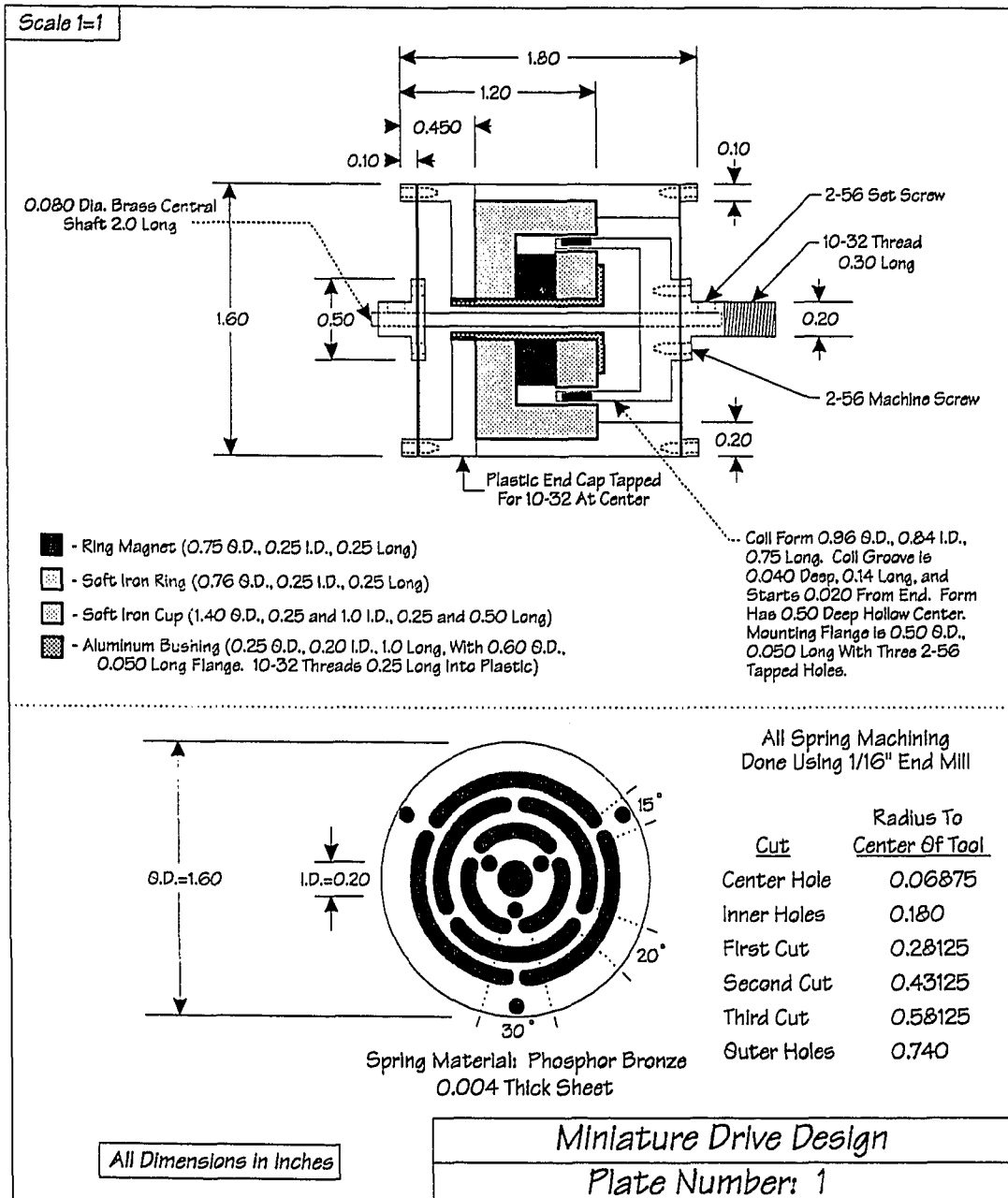
- [1] McSween, H.Y., Jr., *Rev. Geophys.*, 23 (1985), p. 391.
- [2] Singer, R.B., T.B. McCord, R.N. Clark, J.B. Adams, and R.L. Huguenin, *J. Geophys. Res.*, 84 (1979), p. 8415.
- [3] Singer, R.B., *Adv. Space Res.*, 5 (1985), p. 59.
- [4] Bell, J.F., III, T.B. McCord, and P.D. Owensby, *J. Geophys. Res.*, 95 (1990), p. 14,447.
- [5] Morris, R.V., D.G. Agresti, H.V. Lauer, Jr., J.A. Newcomb, T.D. Shelfer, and A.V. Murali, *J. Geophys. Res.*, 94 (1989), p. 2760.
- [6] Morris, R.V., D.G. Schulze, H.V. Lauer, D.G. Agresti, and T.D. Shelfer, *J. Geophys. Res.*, 97 (1992), p. 10,257.
- [7] Morris, R.V., D.G. Agresti, T.D. Shelfer, and T.J. Wdowiak, *Lunar Planet. Sci. Conf. XX*, (1989), p. 721.
- [8] Herzenberg, C.L., R.B. Moler, and D.L. Riley, *Proc. Lunar Sci. Conf. III*, (1971) p. 2103.
- [9] Housley, R.M., M. Blander, M. Abdel-Gawad, R.W. Grant, and A.H. Muir, Jr., *Proc. Apollo 11 Lunar Sci. Conf., Geochim. Cosmochim. Acta Suppl. 1*, 1 (1970), p. 2251.
- [10] Housley, R.M., R.W. Grant, A.H. Muir, Jr., M. Blander, and M. Abdel-Gawad, *Proc. Lunar Sci. Conf. II*, (M.I.T. Press, 1971), p. 2125.
- [11] Morris, R.V., D.G. Agresti, E.L. Wills, T.D. Shelfer, M.M. Pimperl, M.H. Shen, and M.A. Gibson, *Joint Workshop on New Technologies for Lunar Resource Assessment*, (1992), p. 45.
- [12] Gibson, M.A., and C.K. Knudsen, Lunar Bases and Space Activities of the 21st Century (Lunar and Planetary Institute, 1985), p. 543.
- [13] Morris, R.V., *Proc. Lunar Sci. Conf. VII*, (1976), p. 315.

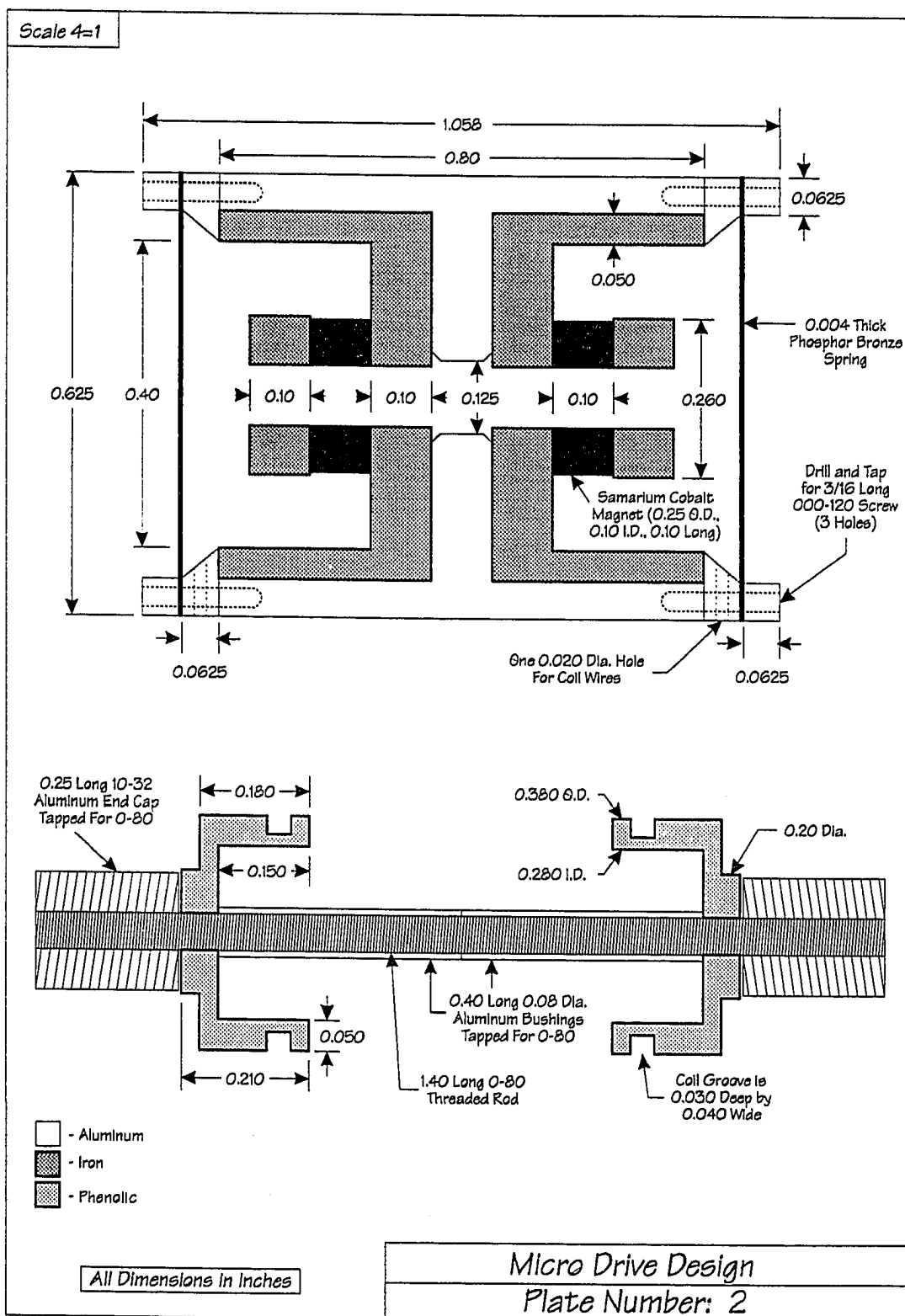
- [14] Morris, R.V., Proc. Lunar Planet. Sci. Conf. IX, (1978), p. 2287.
- [15] Morris, R.V., D.G. Agresti, T.D. Shelfer, and T.J. Wdowiak, Pathfinder Sample Acquisition, Analysis, and Preservation (SAAP) Instrument Technology Workshop, (Houston, November 1988), p. 14.
- [16] Long, G.J., Mössbauer Spectroscopy Applied to Inorganic Chemistry, Volume 1 (Plenum Publishing Corporation, 1984).
- [17] Bancroft, G.M., Mössbauer Spectroscopy An Introduction for Inorganic Chemists and Geochemists (Halsted Press, 1973).
- [18] Woldseth, R., X-ray Energy Spectroscopy (Kevex Corporation, 1973).
- [19] Müller, R.O., Spectrochemical Analysis by X-ray Fluorescence (Plenum Publishing Corporation, 1972).
- [20] Brown, E., J.M. Dairiki, and R.E. Doebler, Table of Isotopes (Seventh edition, 1978), p. 165.
- [21] Cranshaw, T.E., B.W. Dale, G.O. Longworth, and C.E. Johnson, Mössbauer Spectroscopy and its Applications (Cambridge University Press, 1985).
- [22] Stevens, J.G., and V.E. Stevens, Mössbauer Effect Data Index (Plenum Publishing Corporation, 1978), p. 26.
- [23] Preston, M.A., Physics of the Nucleus (Addison-Wesley Publishing Company, Inc., 1962).
- [24] Liboff, R.L., Introductory Quantum Mechanics (Holden-Day Inc., 1980).
- [25] American Institute of Physics Handbook (AIP Publishing, Second Edition, 1963).
- [26] Wertheim, G.K., Phys. Today (July, 1967), p. 31.
- [27] Mössbauer, R.L., Z. Physik, 151 (1958), p.124.
- [28] Kankaleit, E., Rev. Sci. Instr., 35 (1964), p. 194.
- [29] Kankaleit, E., Feedback in electromechanical drive systems, in: Mössbauer Effect Methodology (Plenum Publishing Corporation, 1965), Vol. 1, p. 47.

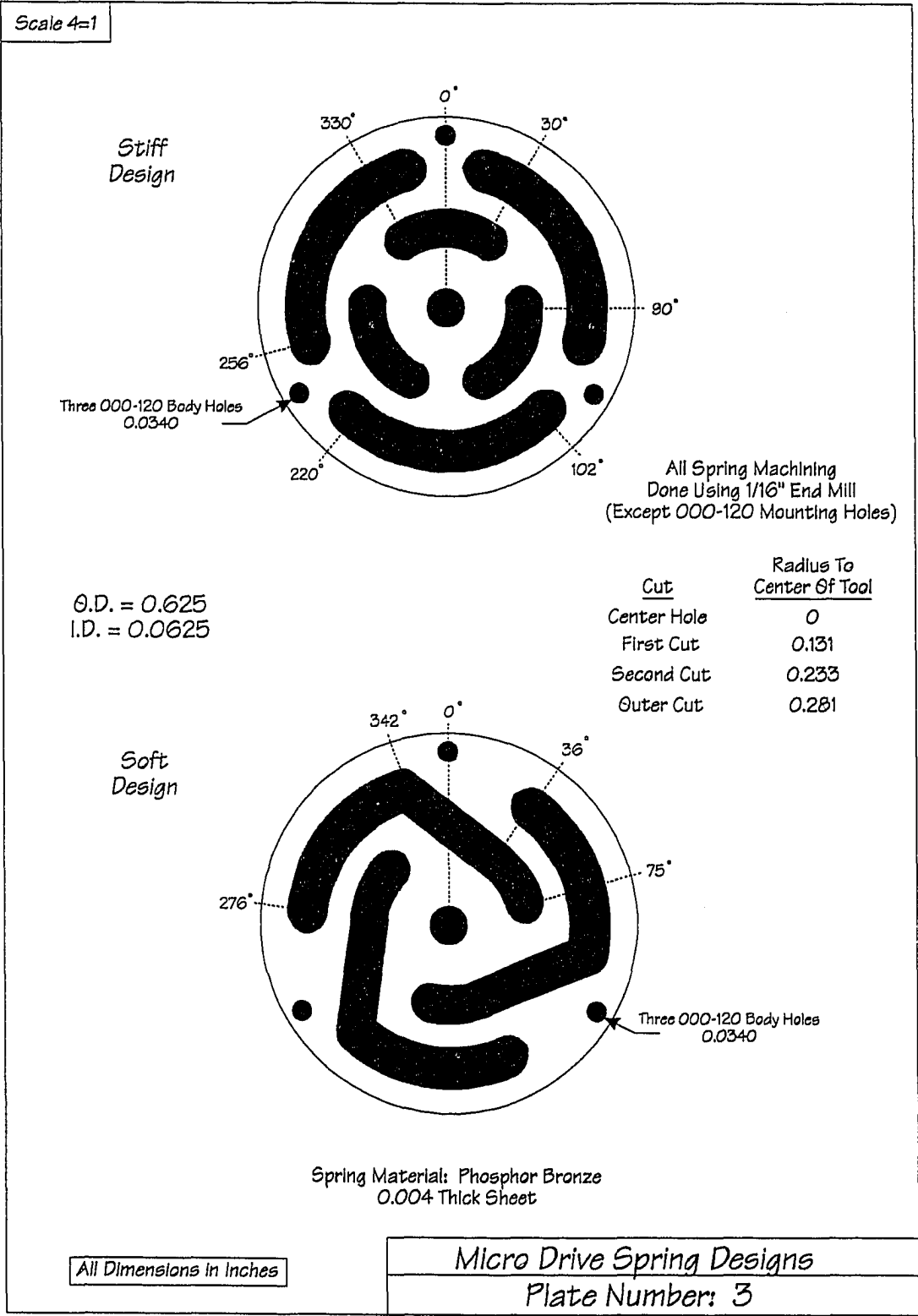
- [30] Shelfer, T.D., M.M. Pimperl, D.G. Agresti, E.L. Wills, and R.V. Morris, Lunar Planet Sci. Conf. XXII (1991), p. 1229.
- [31] Symon, K.R., Mechanics (Second edition, Addison-Wesley Publishing Company, Inc., 1964), p. 54.
- [32] Agresti, D.G., E.L. Wills, T.D. Shelfer, J.S. Iwanczyk, N. Dorri, and R.V. Morris, Lunar Planet. Sci. Conf. XXI (1990), p. 5.
- [33] Agresti, D.G., R.V. Morris, E.L. Wills, T.D. Shelfer, M.M. Pimperl, M.H. Shen, B.C. Clark, B.D. Ramsey, Hyp. Int., 72 (1992), p. 285.
- [34] Pimperl, M.M., Development of a 2π Gas-Filled Detector for use in a Backscatter Mössbauer Spectrometer, (University of Alabama at Birmingham Masters Thesis, 1993 to be published).
- [35] Klingelhöfer, G., J. Foh, P. Held, H. Jäger, E. Kankeleit, Hyp. Int., 71 (1992), p. 1449.
- [36] Arvidson, R.E., J.L. Gooding, and H.J. Moore, Rev. of Geophys., 27 (1989), p. 39.

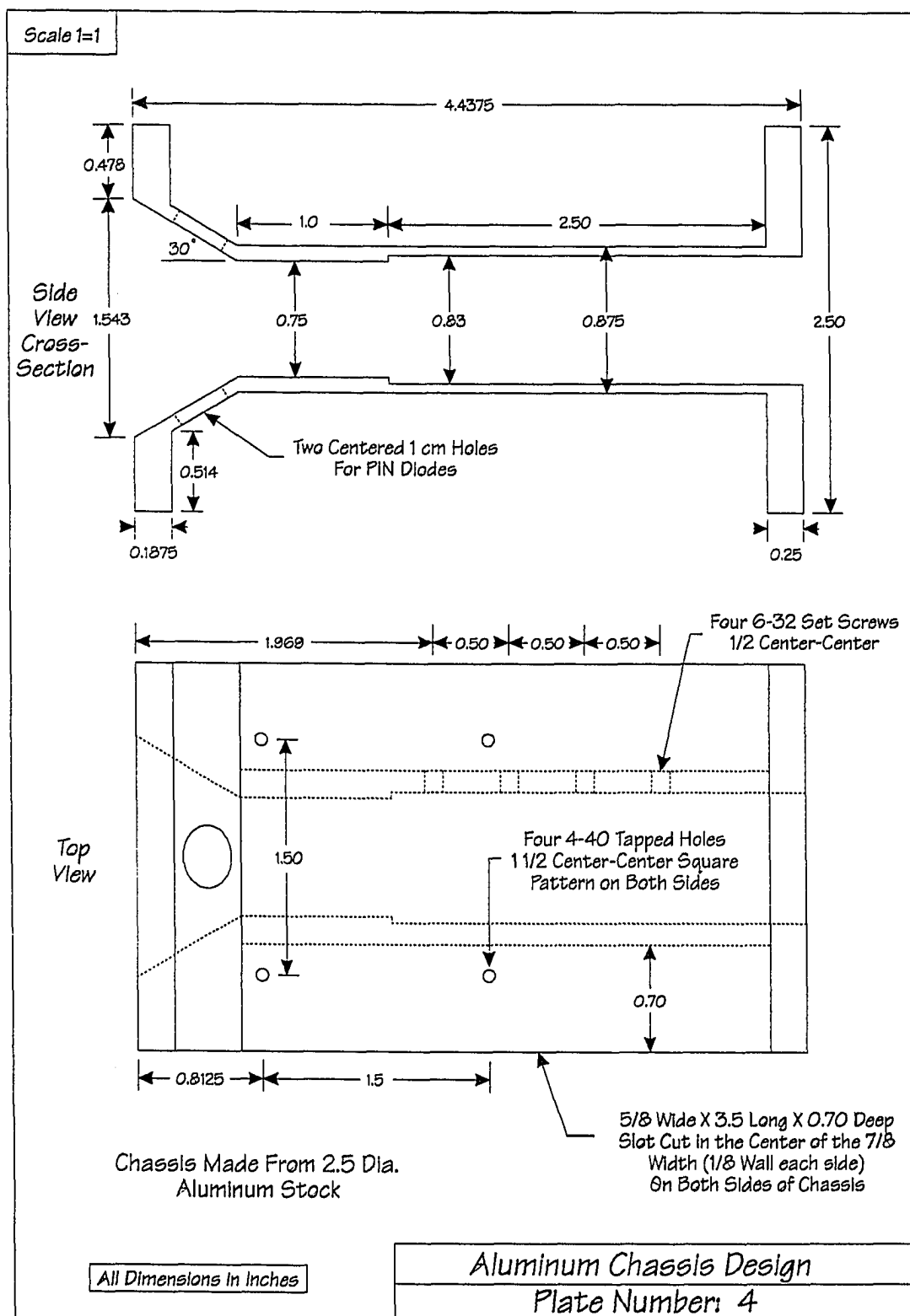
APPENDIX A

MECHANICAL DRAWINGS



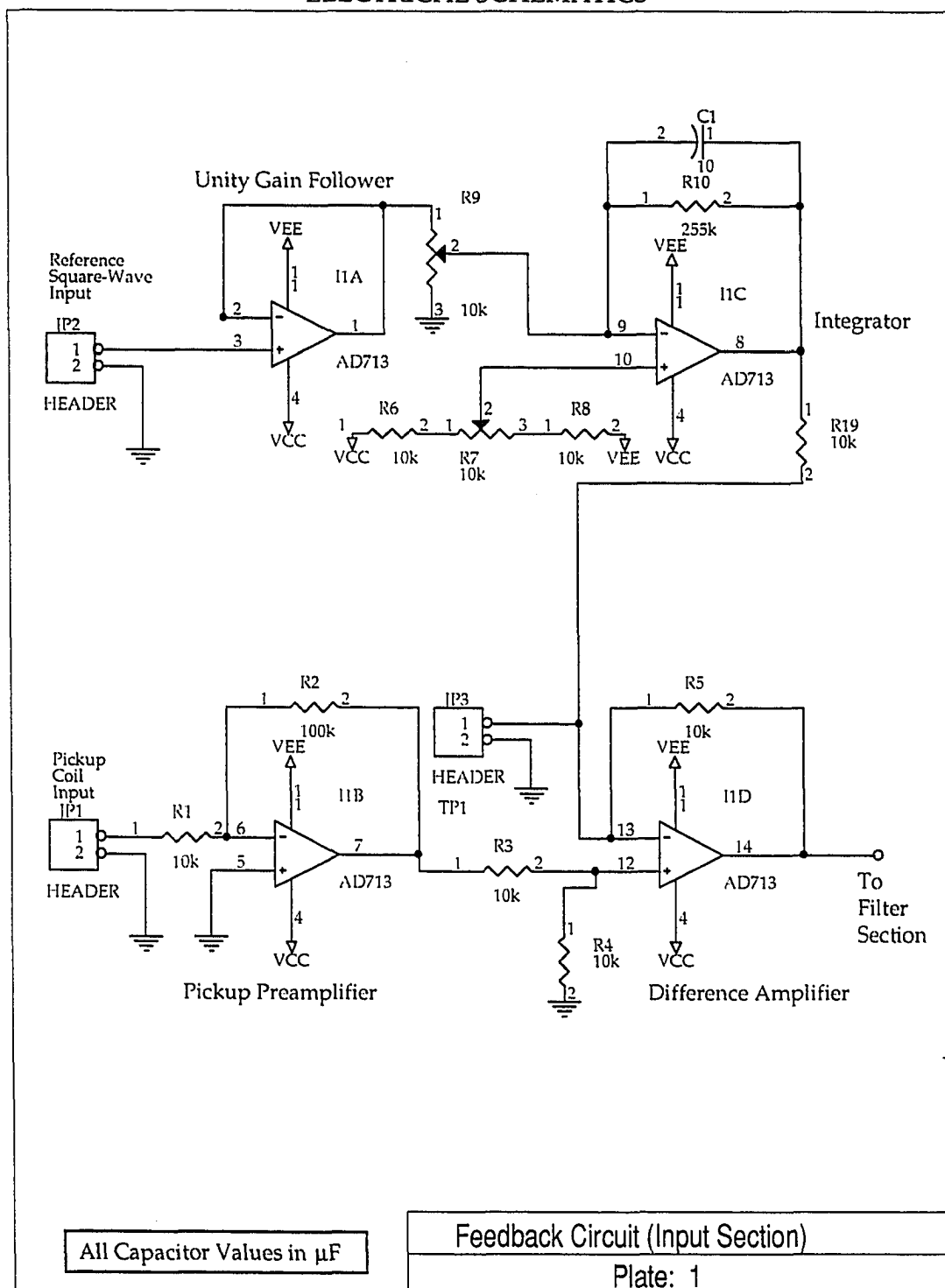




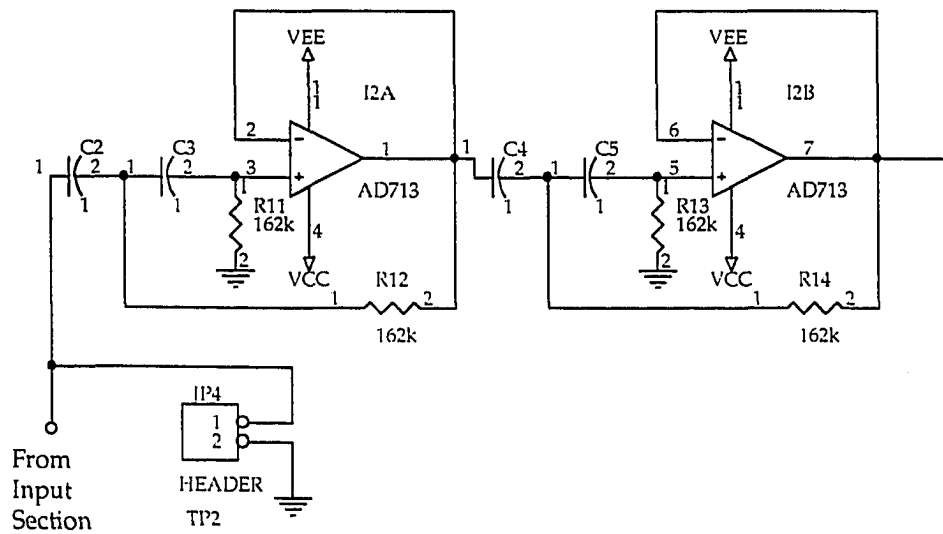


APPENDIX B

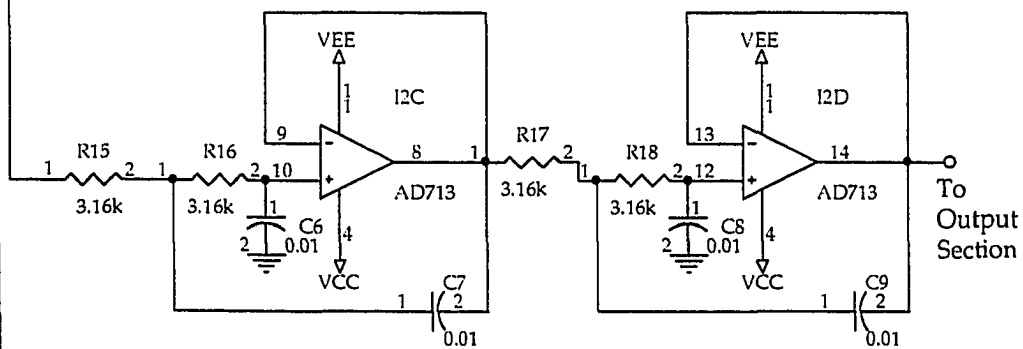
ELECTRICAL SCHEMATICS



Fourth Order High Pass Filter



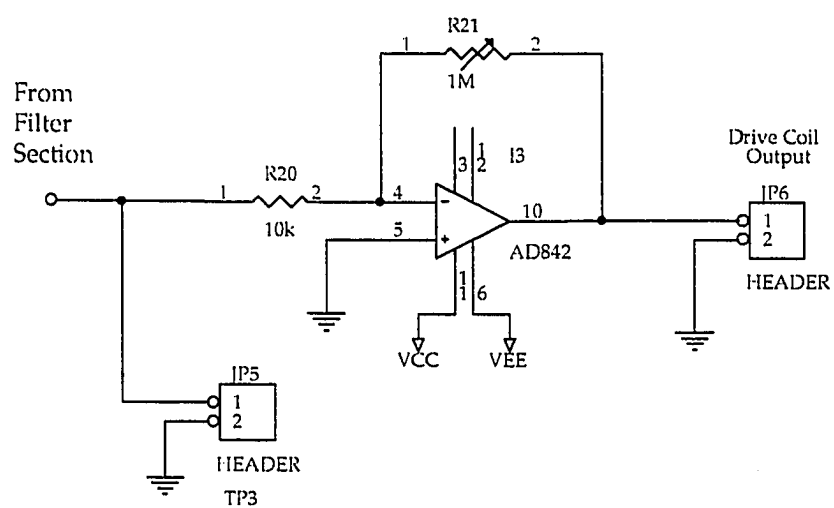
Fourth Order Low Pass Filter

All Capacitor Values in μF

Feedback Circuit (Filter Section)

Plate: 2

Output Amplifier



Feedback Circuit (Output Section)

Plate: 3

APPENDIX C
COMPUTER PROGRAM

TRIANGLE.BAS

By Tad D. Shelfer
Written in MicroSoft QuickBasic 4.5

The purpose of this program is to help determine the appropriate number of terms needed in the series form of a triangular wave, the perfect form of which being two straight lines, by graphically and numerically evaluating the effects of adding more terms to the sum. The output is represented graphically on the screen in an interactive fashion.

INITIALIZATION:

Set up any needed constants and arrays

CONST PI = 3.1415927#

DIM triangle(1 TO 1024) AS SINGLE

DIM sum.data(1 TO 1024) AS SINGLE

DIM err.data(1 TO 1024) AS SINGLE

USERINPUT:

Clear screen and set screen mode for initial user I/O

CLS

SCREEN 12

PALETTE 1, 4131338

PALETTE 7, 4144959

PALETTE 8, 2631720

PALETTE 9, 1315860

PALETTE 10, 657930

COLOR 14

LINE (200, 100)-(300, 10), 12

LINE (300, 10)-(400, 100), 12

LINE (200, 110)-(200, 120), 7

LINE (200, 120)-(220, 120), 7

LINE (220, 120)-(220, 110), 7

LINE (224, 110)-(224, 120), 7

LINE (224, 120)-(276, 120), 7

LINE (276, 120)-(276, 110), 7

LINE (280, 110)-(280, 120), 7

LINE (280, 120)-(320, 120), 7

LINE (320, 120)-(320, 110), 7

LINE (324, 110)-(324, 120), 7

LINE (324, 120)-(376, 120), 7

LINE (376, 120)-(376, 110), 7

LINE (380, 110)-(380, 120), 7

LINE (380, 120)-(400, 120), 7

LINE (400, 120)-(400, 110), 7

LOCATE 9, 27: PRINT "R R R R R"

```

LOCATE 10, 27: PRINT "a  a  a  a  a"
LOCATE 11, 27: PRINT "n  n  n  n  n"
LOCATE 12, 27: PRINT "g  g  g  g  g"
LOCATE 13, 27: PRINT "e  e  e  e  e"
LOCATE 15, 27: PRINT "1  2  3  4  1"

LOCATE 18, 18: PRINT "Enter the width in channels for Ranges 1 & 3."
LOCATE 19, 18: PRINT "This width will be used as windows for "
LOCATE 20, 18: PRINT "calculating errors in given regions."
LOCATE 21, 18: PRINT "(1024 channels total) Enter width : "; : INPUT
                range.width

LOCATE 25, 18: PRINT "Enter the number of terms to use in the sum."
LOCATE 26, 18: PRINT "Enter number : "; : INPUT sum.num

CLS

LOCATE 10, 18: PRINT "You have entered"; range.width; "for the range
                width."

LOCATE 12, 18: PRINT "You will be using"; sum.num; "term(s) in the
                sum."

LOCATE 15, 18: PRINT "Is this correct (Y/N)"; : INPUT answer$
IF answer$ <> "Y" AND answer$ <> "y" THEN GOTO USERINPUT

CLS

```

' Go ahead and draw graph borders and prepare for calculations & plotting

' Plot regions of interest if user input > 0 channels

```

IF range.width < 1 THEN GOTO skipregions
half = INT(range.width / 2)

```



```

px1 = 20 + half / 2
px2 = 20 + (512 - half) / 2
px3 = 20 + (512 + half) / 2
px4 = 20 + (1024 - half) / 2
LINE (20, 15)-(px1, 267), 10, BF
LINE (20, 292)-(px1, 444), 10, BF
LINE (px2, 15)-(px3, 267), 10, BF
LINE (px2, 292)-(px3, 444), 10, BF
LINE (px4, 15)-(534, 267), 10, BF
LINE (px4, 292)-(534, 444), 10, BF

```

skipregions:

Draw borders and grids

```

LINE (20, 15)-(534, 267), 8, B
LINE (20, 141)-(534, 141), 9
LINE (277, 15)-(277, 267), 9
LINE (149, 15)-(149, 267), 9
LINE (405, 15)-(405, 267), 9
LINE (20, 292)-(534, 444), 8, B
LINE (20, 330)-(534, 330), 9
LINE (20, 368)-(534, 368), 9
LINE (20, 406)-(534, 406), 9
LINE (277, 292)-(277, 444), 9
LINE (149, 292)-(149, 444), 9
LINE (405, 292)-(405, 444), 9

```

COLOR 8

LOCATE 2, 1: PRINT " 1";

LOCATE 9, 1: PRINT " 0";

LOCATE 17, 1: PRINT "-1";

LOCATE 18, 3: PRINT "0";

LOCATE 18, 18: PRINT CHR\$(227); "/4";

LOCATE 18, 35: PRINT CHR\$(227);

LOCATE 18, 49: PRINT "3"; CHR\$(227); "/4";

LOCATE 18, 66: PRINT "2"; CHR\$(227);

LOCATE 29, 3: PRINT "0";

LOCATE 29, 18: PRINT CHR\$(227); "/4";

LOCATE 29, 35: PRINT CHR\$(227);

LOCATE 29, 49: PRINT "3"; CHR\$(227); "/4";

LOCATE 29, 66: PRINT "2"; CHR\$(227);

Calculate perfect triangle data and store in array

FOR i = 1 TO 512

$x = (i * \text{PI}) / 512$

$y = (2 / \text{PI}) * x - 1$

triangle(i) = y

NEXT i

FOR i = 512 TO 1024

$x = (i * \text{PI}) / 512$

$y = (-2 / \text{PI}) * x + 3$

triangle(i) = y

NEXT i

Plot perfect triangle

```

cx = 21: cy = 141
FOR x = 1 TO 1024
    y = triangle(x)
    px = cx + x / 2
    py = cy - 125 * y
    LINE (px, cy)-(px, py), 1
NEXT x

```

Calculate sum based on user defined # of terms and store in array

```

terms = 1
term.num = 1
FOR i = 1 TO 1024
    sum.data(i) = 0
NEXT i
DO
    FOR i = 1 TO 1024
        x = i * PI / 512
        y = (1 / (term.num * term.num)) * COS(term.num * x)
        sum.data(i) = sum.data(i) + y
    NEXT i
    term.num = term.num + 2
    terms = terms + 1
LOOP WHILE terms <= sum.num

```

```

FOR i = 1 TO 1024
    sum.data(i) = sum.data(i) * (-8 / (PI * PI))
NEXT i

```

' Plot sum

```

cx = 21: cy = 141
FOR x = 1 TO 1024
    y = sum.data(x)
    px = cx + x / 2
    py = cy - 125 * y
    LINE (px, cy)-(px, py), 14
NEXT x

```

```

cx = 21: cy = 141
FOR x = 1 TO 1024
    y = triangle(x)
    px = cx + x / 2
    py = cy - 125 * y
    PSET (px, py), 1
NEXT x

```

' Calculate error between perfect and series triangle waveforms

```

max.error = 0
FOR i = 1 TO 1024
    delta = sum.data(i) - triangle(i)
    err.data(i) = (delta / 2) * 100

```

```

        temp = ABS(err.data(i))
        IF temp > max.error THEN
            max.error.channel = i
            max.error = temp
        END IF
    NEXT i
    COLOR 15
    LOCATE 3, 70: PRINT sum.num; "term(s)";
    LOCATE 5, 69: PRINT "Max error(%)";
    LOCATE 6, 72: PRINT USING "##.###"; err.data(max.error.channel)

```

Determine maximum error in regions of interest if range.width > 0

```

IF range.width < 1 THEN GOTO skiprangeerror
max = 0
FOR i = 1 TO half
    temp = ABS(err.data(i))
    IF temp > max THEN
        range1.max = err.data(i)
        max = temp
    END IF
NEXT i
max = 0
FOR i = half TO 512 - half
    temp = ABS(err.data(i))
    IF temp > max THEN
        range2.max = err.data(i)
    END IF
NEXT i

```

```

        max = temp
    END IF
NEXT i
max = 0
FOR i = 512 - half TO 512 + half
    temp = ABS(err.data(i))
    IF temp > max THEN
        range3.max = err.data(i)
        max = temp
    END IF
NEXT i
max = 0
FOR i = 512 + half TO 1024 - half
    temp = ABS(err.data(i))
    IF temp > max THEN
        range4.max = err.data(i)
        max = temp
    END IF
NEXT i
max = 0
FOR i = 1024 - half TO 1024
    temp = ABS(err.data(i))
    IF temp > max THEN
        range5.max = err.data(i)
        max = temp
    END IF
NEXT i

```

```

LOCATE 8, 69: PRINT "ROI width :";
LOCATE 9, 72: PRINT range.width;
LOCATE 11, 69: PRINT "By Region(%)";
LOCATE 12, 70: PRINT "1 : "; : PRINT USING "###.###"; range1.max
LOCATE 13, 70: PRINT "2 : "; : PRINT USING "###.###"; range2.max
LOCATE 14, 70: PRINT "3 : "; : PRINT USING "###.###"; range3.max
LOCATE 15, 70: PRINT "4 : "; : PRINT USING "###.###"; range4.max
LOCATE 16, 70: PRINT "5 : "; : PRINT USING "###.###"; range5.max

```

skiprangeerror:

Plot error data

```

max.scale = INT(ABS(err.data(max.error.channel))) + 1
cx = 21: cy = 368
FOR i = 1 TO 1024
    y = err.data(i) * (75 / max.scale)
    px = cx + i / 2
    py = cy - y
    IF y < 0 THEN LINE (px, cy)-(px, py), 12
    IF y >= 0 THEN LINE (px, cy)-(px, py), 2
NEXT i
COLOR 8
LOCATE 24, 69: PRINT "0";
LOCATE 19, 68: PRINT USING "###"; max.scale
LOCATE 28, 68: PRINT USING "###"; -max.scale

```

```
GOSUB waitkey
```

```
RUN
```

```
END
```

```
waitkey:
```

```
  a$ = INKEY$: IF a$ = "" THEN GOTO waitkey
```

```
  IF a$ = "q" OR a$ = "Q" THEN STOP
```

```
  RETURN
```


APPENDIX D
EXPERIMENTAL DATA

Amplitude and Phase Response Raw Data:

Standard Laboratory Drive (Caltech):

Frequency (Hz)	Pickup amplitude (mV RMS)	Phase difference (degrees)
10.0	8.15	89.4
20.0	20.06	86.0
25.0	30.45	84.5
30.0	50.6	81.8
32.5	67.7	79.6
33.5	78.6	78.2
34.5	91.4	76.2
35.0	102.3	74.8
35.5	113.6	73.5
36.0	124.2	72.1
36.5	141.2	70.0
37.0	155.2	67.8
37.5	177.4	65.2
38.0	203.6	61.4
38.5	265.7	52.6
39.0	329.6	43.1
39.5	373.8	35.2
40.0	465.6	10.8
40.4	479.5	-0.4

Frequency (Hz)	Pickup amplitude (mV RMS)	Phase Difference (degrees)
40.5	473.2	-12.1
41.0	440.5	-26.0
41.5	358.8	-43.8
42.0	329.0	-49.3
43.0	229.5	-64.3
44.0	180.4	-71.2
45.0	148.0	-75.4
48.0	91.4	-82.7
50.0	71.8	-85.1
55.0	49.4	-87.9
60.0	38.00	-89.6
65.0	31.47	-90.6
70.0	26.86	-91.4
75.0	23.43	-92.0
80.0	20.85	-92.6
90.0	17.15	-93.5
100	14.61	-94.3
110	12.66	-95.0
120	11.37	-95.4
140	9.04	-95.7
160	8.01	-94.6
180	7.01	-97.4
200	5.88	-97.3
250	4.692	-101.4

Frequency (Hz)	Pickup amplitude (mV RMS)	Phase difference (degrees)
285	2.482	-101.0
289	1.195	-89.6
290	0.724	-64.5
291	4.303	-71.9
292	1.689	-78.3
293	2.235	46.5
294	4.698	52.1
295	7.44	50.9
295.5	40.56	-5.0
296	32.37	-70.0
297	11.76	-98.3
298	9.93	-100.3
300	7.17	-102.7
350	3.897	-104.3
400	3.133	-108.0
450	2.662	-109.4
500	2.348	-110.8
600	1.866	-113.5
700	1.532	-115.0
800	1.301	-118.1
1,000	1.001	-120.1
1,800	0.617	-128.2
2,000	0.395	-138.3

Frequency (Hz)	Pickup amplitude (mV RMS)	Phase difference (degrees)
3,000	0.284	-136.9
4,000	0.288	-141.5
5,520	0.783	-154.4
5,570	1.260	-178.6
5,630	0.456	139.1
5,700	0.458	-156.4
5,900	1.612	-159.4
5,960	4.085	130.4
6,010	0.897	75.0

Miniature Drive:

Frequency (Hz)	Pickup amplitude (μ V RMS)	Phase difference (degrees)
5.0	60.3	92.1
10.0	152.3	85.5
15.0	321.1	80.7
18.0	595	72.1
19.0	836	65.9
19.5	1,043	60.4
20.0	1,385	50.2
20.5	1,627	41.3
21.0	1,846	30.4
21.4	1,998	19.7

Frequency (Hz)	Pickup amplitude (μ V RMS)	Phase difference (degrees)
21.6	2,058	13.9
21.8	2,087	6.3
22.0	2,097	0.9
22.2	2,061	-8.0
22.4	1,925	-20.2
22.6	1,687	-31.6
23.0	1,473	-39.0
23.5	1,299	-43.8
24.0	1,110	-48.8
25.0	897	-54.7
30.0	420.7	-67.9
35.0	276.5	-74.4
40.0	205.6	-80.6
45.0	163.6	-88.1
50.0	126.4	-101.3
55.0	74.7	-126.5
57.0	39.30	-144.2
58.0	19.07	-154.1
59.1	0.54	0
59.6	6.50	9.3
59.9	15.60	5.0
60.5	23.70	1.3
61.0	34.36	-4.4

Frequency (Hz)	Pickup amplitude (μ V RMS)	Phase difference (degrees)
62.0	46.20	-10.5
63.0	57.15	-15.9
64.0	68.55	-24.5
65.1	73.5	-29.9
66.0	77.4	-34.4
67.0	80.0	-39.7
68.0	81.6	-44.2
69.1	82.6	-47.7
70.0	83.0	-50.4
75.1	81.7	-61.3
80.1	78.0	-68.8
90.0	69.2	-80.6
100.1	56.9	-97.8
109.9	36.3	-134.3
119.6	3.9	0
125.0	18.6	-13.5
129.9	27.0	-27.3
140.1	30.8	-43.4
149.9	25.4	-38.8
160.2	52.1	-43.0
170.3	52.9	-62.5
180.1	47.6	-72.3
190.0	42.6	-78.9
200.0	36.1	-80.3

Microdrive (stiff springs):

Frequency (Hz)	Pickup amplitude (mV RMS)	Phase difference (degrees)
10.0	0.0277	92.1
20.0	0.0556	90.8
30.0	0.0836	90.6
40.0	0.1123	90.6
50.0	0.1416	90.8
100.1	0.3018	91.0
150.2	0.497	90.8
200	0.790	90.4
250	1.290	89.7
301	2.449	88.7
320	3.482	88.0
340	5.99	86.6
350	8.86	84.5
355	13.32	81.7
360	22.22	76.5
362	28.37	73.0
363	38.40	66.5
364	41.68	64.2
365	60.5	47.8
366	92.4	0

Frequency (Hz)	Pickup amplitude (mV RMS)	Phase difference (degrees)
367	88.5	-14.9
368	70.2	-39.2
369	60.4	-48.8
370	48.47	-61.8
375	28.86	-74.5
379	17.21	-81.0
390	9.01	-84.5
400	6.66	-85.5
420	4.172	-86.8
440	3.042	-87.4
500	1.834	-88.3
550	1.343	-88.8
600	1.077	-89.1
700	0.780	-89.2
801	0.628	-89.4
1,000	0.4691	-89.6
1,502	0.2880	-90.3
2,000	0.2112	-90.9
3,000	0.1431	-91.6
4,000	0.1098	-90.6
5,000	0.1026	-92.8
6,000	0.0907	-93.6
7,000	0.1006	-97.0
7,500	0.1080	-96.2

Frequency (Hz)	Pickup amplitude (mV RMS)	Phase difference (degrees)
7,700	0.1263	-122.1
8,000	0.0894	-96.5
8,500	0.1068	-96.2
9,000	0.1473	-106.0
9,200	0.0882	-128.4
10,000	0.1311	-98.2

Microdrive (soft springs):

Frequency (Hz)	Pickup amplitude (mV RMS)	Phase difference (degrees)
10.0	0.252	90.8
20.0	0.503	90.0
30.0	0.769	89.7
40.0	1.054	89.5
50.0	1.365	89.5
60.0	1.707	89.7
70.0	2.105	89.2
80.0	2.576	89.1
90.0	3.145	88.9
100.0	3.866	88.7
110.0	4.817	88.4
120.0	6.29	88.9

Frequency (Hz)	Pickup amplitude (mV RMS)	Phase difference (degrees)
130.0	8.09	87.5
140.0	11.53	86.7
150.0	18.88	85.0
155.0	26.96	83.2
160.0	45.78	79.0
162.0	62.6	75.1
163.0	75.8	72.2
164.0	94.7	67.7
165.0	121.5	61.2
165.5	138.1	56.9
166.0	156.4	52.0
166.5	176.5	46.2
167.0	195.2	40.5
167.5	215.2	32.9
168.0	234.8	23.9
168.2	242.0	19.6
168.4	248.3	15.0
168.5	251.1	12.3
168.6	253.5	9.6
168.7	255.4	6.8
168.8	257.1	3.3
168.9	257.7	-0.9
169.0	256.7	-6.6
169.1	251.1	-14.3

Frequency (Hz)	Pickup amplitude (mV RMS)	Phase difference (degrees)
169.2	247.5	-19.6
169.3	215.0	-35.4
169.4	181.2	-46.4
169.5	166.5	-50.8
169.7	147.3	-56.3
170.0	129.3	-61.1
170.5	107.8	-66.6
171.0	92.9	-70.2
172.0	73.7	-74.6
173.0	61.4	-77.4
175.0	46.30	-80.9
180.0	28.62	-84.7
185.0	20.87	-86.5
190.0	16.47	-87.5
200.0	11.70	-88.6
210.0	9.12	-89.2
220.0	7.54	-89.6
230.0	6.45	-89.9
240.0	5.80	-89.1
250.0	5.09	-90.2
260.0	4.612	-90.5
270.0	4.222	-90.6
280.0	3.900	-90.8

Frequency (Hz)	Pickup amplitude (mV RMS)	Phase difference (degrees)
290.0	3.631	-90.9
300.0	3.416	-90.8
320.0	3.018	-91.1
350.0	2.598	-91.6
400.0	2.126	-92.5
500.0	1.570	-92.5
600.0	1.327	-92.0
700.0	1.071	-93.7
800.0	0.918	-94.3
900.0	0.808	-94.8
1,000	0.719	-95.2
1,500	0.480	-98.1
2,000	0.360	-100.8
3,000	0.236	-106.4
4,000	0.168	-110.9
5,000	0.141	-114.8
6,000	0.123	-119.9
7,000	0.110	-120.5
8,000	0.0993	-125.1
9,000	0.0948	-128.2
10,000	0.0928	-130.2

GRADUATE SCHOOL
UNIVERSITY OF ALABAMA AT BIRMINGHAM
DISSERTATION APPROVAL FORM

Name of Candidate Tad D. Shelfer

Major Subject Physics

Title of Dissertation Combined Backscatter Mössbauer Spectrometer/X-Ray
Fluorescence Analyzer (BaMS/XRF) for Planetary Surface Materials

Dissertation Committee:

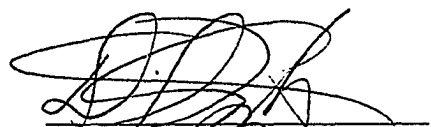
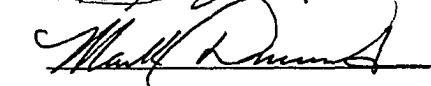
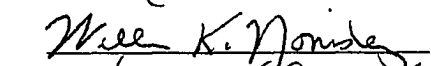
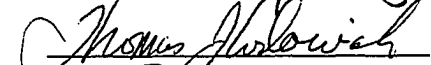

David G. Agresti, Chairman


Mark Drummond

William K. Nonidez

Thomas J. Wdowiak

Edward L. Wills

Director of Graduate Program 

Dean, UAB Graduate School 

Date 1/6/93